# Modulation and moderation of shock wave front by unsteady interaction with grid turbulence

*A thesis submitted in partial fulfillment of the requirements*

*for the degree of Doctor of Engineering*

**Gaku FUKUSHIMA**

Department of Aerospace Engineering

Nagoya University

December 2022

# Dissertation Committee

Akihiro SASOH

Professor

Nagoya University

Yoshiyuki TSUJI

Professor

Nagoya University

Koji NAGATA

Professor

Nagoya University

Kiyoshi KINEFUCHI

Associate Professor

Nagoya University

Keiichi KITAMURA

Associate Professor

Yokohama National University

# Acknowledgements

I would like to express the deepest appreciation to my supervisor, Professor Akihiro Sasoh, for his constant guidance, encouragement, and support. I am truly blessed to have met him and learn about a true researcher's attitude from him. I am grateful to Associate Professor Kiyoshi Kinefuchi for helpful advice and encouragement. I would like to thank Assistant Professor Daisuke Ichihara and Designated Assistant Professor Yusuke Nakamura for valuable discussions and encouragement. I am grateful to Professor Koji Nagata for accepting me in his laboratory and allowing me to learn about the latest turbulence research. I appreciate Associate Professor Keiichi Kitamura, Yokohama National University, for accepting me to join his laboratory and giving me an opportunity to conduct research in the field of computational fluid dynamics. I am also grateful to Professor Yoshiyuki Tsuji for reviewing my thesis and providing valuable comments regarding turbulence.

I would like to express my deep appreciation to Futamura Chemical Co. Ltd., for supporting this study and providing the cellophane diaphragm.

I thank all the members of Shock Wave and Space Propulsion Laboratory. I am especially indebted to Dr. Akira Iwakawa, Dr. Takahiro Tamba, Mr. Daisuke Kuwabara, Mr. Shingo Ogawa, Mr. Jiaxi Wei, Mr. Jun Hagiwara, Ms. Tsuki Yamaguchi, Mr. Naotaka Shigeta, and Mr. Daniel Custodio who paid many efforts during the previous studies and cooperated on my current work. I also thank Associate Professor Tomoaki Watanabe, Dr. Kento Tanaka, and Dr. Kento Inokuma in Fluid Dynamics Laboratory at Nagoya

University for conducting many stimulating discussions.

Finally, I would like to show my greatest appreciation to my wife Machika and family for their kind support, understanding, and encouragement.

Gaku Fukushima

# Contents

List of Published Papers ..... vi

List of Figures ..... vii

List of Tables ..... xiii

Nomenclatures ..... xiv

Chapter 1 Introduction ..... 1

1.1 Problems related to shock waves in aerospace engineering ..... 1

1.2 Related studies on shock–turbulence interactions ..... 3

1.2.1 Effect of shock waves on turbulence ..... 3

1.2.2 Effect of turbulence on the post-shock pressure field ..... 5

1.2.3 Effect of turbulence on the shock wave structure ..... 6

1.3 Objective of this thesis ..... 8

1.4 Structure of this thesis ..... 11

Chapter 2 Experimental law in cellophane diaphragm rupture processes and its impacts on shock tube performance ..... 13

2.1 Introduction of this chapter ..... 13

2.1.1 Introduction to shock tubes ..... 13

2.1.2 Effect of diaphragm rupture on shock wave formation ..... 14

2.1.3 Objective of this chapter ..... 15

2.2 Experimental setup ..... 16

2.2.1 Shock tubes ..... 16

2.2.2 Visualization systems ..... 18

2.2.3 Overpressure measurement ..... 19

2.3 Cellophane diaphragm rupture ..... 21
2.3.1 Strain stress acting on cellophane diaphragm..... 21
2.3.2 Crack propagation process in cellophane diaphragm ..... 22
2.3.3 Petal formation law ..... 28
2.3.4 Opening dynamics of cellophane diaphragm ..... 33
2.4 Effect of cellophane diaphragm rupture on shock wave formation ..... 46
2.5 Summary of this chapter..... 52
Chapter 3 Shock wave modulation by interaction with grid turbulence..... 53
3.1 Introduction of this chapter ..... 53
3.2 Experimental setup..... 54
3.2.1 Counter-driver shock tube ..... 54
3.2.2 Flow characteristics in counter-driver shock tube ..... 61
3.2.3 Grid turbulence characteristics ..... 63
3.3 Effects of turbulence on side projected shock wave ..... 67
3.4 Summary of this chapter..... 82
Chapter 4 Criterion for losing shock wave front profile by interaction with grid turbulence ..... 86
4.1 Introduction of this chapter ..... 86
4.2 Experimental verification of vanished shock regime..... 87
4.2.1 Experimental setup..... 87
4.2.2 Visualization of shock–turbulence interaction ..... 90
4.3 Criteria for losing shock wave front profile ..... 95
4.3.1 Shock-forward-induced flow interaction ..... 95
4.3.2 Condition for losing shock wave front during interaction with isotropic

turbulence ..... 99

4.4 Summary of this chapter..... 107

Chapter 5 Conclusions ..... 109

Appendix A Polyester diaphragm opening process..... 112

Appendix B Response limit of the hot-wire anemometer and distribution of velocity fluctuation of grid turbulence ..... 114

References ..... 117

# List of Published Papers

## Chapter 2

Fukushima, G., Tamba, T., Iwakawa, A., and Sasoh, A., “Influence of cellophane diaphragm rupture processes on the shock wave formation in a shock tube,” Shock Waves, Volume 30, pp. 545–557, 2020.

Fukushima, G., Hagiwara, J., Nakamura, Y., and Sasoh, A., “Petal formation law in a cellophane diaphragm interfacing air-pressure difference,” Physical Review E, Volume 106, L043001, 2022.

## Chapter 3

Tamba, T., Fukushima, G., Kayumi, M., Iwakawa, A., and Sasoh, A., “Experimental investigation of the interaction of a weak planar shock with grid turbulence in a counter-driver shock tube,” Physical Review Fluids, Volume 4, Issue 7, 073401, 2019.

Fukushima, G., Ogawa, S., Wei, J., Nakamura, Y., and Sasoh, A., “Impacts of grid turbulence on the side projection of planar shock waves,” Shock Waves, Volume 31, pp. 101–115, 2021.

## Chapter 4

Fukushima, G., Wei, J., Ogawa, S., Hagiwara, J., Nakamura, Y., and Sasoh, A., “Losing the shock wave front profile due to interaction with turbulence,” Fluid Dynamics Research, Volume 53, Number 2, 025504, 2021.

# List of Figures

Figure 2.1 Experimental setups. (a) Setup I for visualizing crack propagation. (b) Setup II for visualizing the complete opening process of the cellophane diaphragm in the shock tube. The strobe light source is omitted in the sideview. (c) Setup III for the overpressure measurement. ..... 20

Figure 2.2 Crack propagation behaviors. (a) $D$ = 62 mm, $\varphi$ = 35.0%RH, $p_4$ = 140.9 kPa, and $p_1$ = 100.9 kPa and (b) $D$ = 120 mm, $\varphi$ = 41.5%RH, $p_4$ = 121.5 kPa, and $p_1$ = 101.5 kPa. ..... 26

Figure 2.3 Extracted crack head positions. ..... 27

Figure 2.4 Time evolution of the averaged crack length. ..... 27

Figure 2.5 Examples of the ruptured diaphragm morphologies under different humidity values at different $\sigma_i$ obtained using Setup II. The brightness and the contrast are adjusted for visibility. ..... 31

Figure 2.6 Number of cracks $N$ as a function of $r$. ..... 32

Figure 2.7 $N/2\pi r$ versus $\sigma_i$, where the dashed line represents the linear fitting results for all the cases wherein crack branch events are observed. The data points for $\sigma_i \leq 10.3$ MPa (with gray plot frames) correspond to the experimental condition wherein $p_4 = p_1 + 20.0$ kPa and is subsequently decreased to $p_4 \leq p_1 + 3.0$ kPa. The line colors in Fig. 2.6 and 2.7 for $D$ = 62 mm are the same. ..... 32

Figure 2.8 Examples of the visualized petal opening processes: (a) $p_4$ = 120.6 kPa, $p_1$ = 100.6 kPa, (b) $p_4$ = 129.9 kPa, $p_1$ = 99.9 kPa, and (c) $p_4$ = 140.6 kPa, $p_1$ = 100.6 kPa. ..... 35

Figure 2.9 Time variations of the projected opening area ratio. ..... 37

Figure 2.10 Schematic of the estimation model of the propagation of the domain of influence on the diaphragm petal at $p_4$ = 120.6 kPa and $p_1$ = 100.6 kPa: (a) a representative of the petal shape, (b) the state when the cracks propagate from the top to the shock tube wall, (c) the state at the time of the completion of the crack propagation ($t = t_1$), (d) the state after the completion of the crack propagation with spreading of the domain of influence, and (e) the state when the domain of influence covers the entire petal. ..... 41

Figure 2.11 Time variations of the projected opening area ratio from the experiments and the models. The solid lines show the results of the best fits when various integer values of $\tau = \tau_e$ are used in the rotational motion model. The dashed lines show the results using estimated $t_2$ for $\tau$, calculated from the analysis shown in Fig. 2.10. .. 44

Figure 2.12 Plots of the characteristic times as functions of $\Delta p_{41}$. $\tau_e$ is the effective opening force period used in the best fitting, $t_1$ is the time of crack propagation completion, and $t_2$ is the time when the domain of influence covers the entire petal surface. .... 45

Figure 2.13 Overpressure histories at $p_4$ = 110.6 kPa and $p_1$ = 100.6 kPa. (a) $x/D$ = 2.26 and (b) $x/D$ = 22.4. Under these conditions, a fully planar shock wave is not formed because the shock formation distance is longer than the used driven section length. ..... 50

Figure 2.14 Overpressure histories at $p_4$ = 140.6 kPa and $p_1$ = 100.6 kPa. (a) $x/D$ = 2.26 and (b) $x/D$ = 22.4. Red points (i)–(iv) correspond to the characteristic set of time and overpressure used in the analysis of the coalescence of the compression waves. ..... 50

Figure 2.15 $c_+$ diagram at $p_4$ = 140.6 kPa and $p_1$ = 100.6 kPa: (a) $0 \leq x/D \leq 6.5$ and (b) 0

≤ $x/D$ ≤ 15. All compression waves coalesce into the leading shock wave by $x/D$ = 27.1. ..... 51

Figure 3.1 (a) Schematics of CD-ST. (b) Example of $x$–$t$ diagram of shock–turbulence interaction for $M_{s,L\text{-}tSW}$ = 1.05, $M_{s,R\text{-}gSW}$ = 1.32, and $L_i$ = 1185 mm. L-, from the left driver; R-, from the right driver; i, incident; t, transmitted; g, grid transmitted; r, reflected from the grid; SW, shock wave; EW, expansion waves; CS, contact surface; [1], driven section; [4L], left driver; [4R] right driver; [2L], state behind L-iSW; [2R], state behind R-iSW; [2R'], state behind R-gSW; [2Rr], state behind R-rSW; [GT], grid turbulence state. ..... 59

Figure 3.2 Example of raw pressure history of L-iSW at $x$ = 1.25 m after it passed through 16 sheets of punched metal. The shock Mach number was 1.008 ..... 60

Figure 3.3 Distribution of the normalized total temperature of the grid turbulence in the $y$-direction: (a) $M_{s,R\text{-}gSW}$ = 1.09, (b) $M_{s,R\text{-}gSW}$ = 1.18, and (c) $M_{s,R\text{-}gSW}$ = 1.32..... 66

Figure 3.4 Turbulent Mach number as a function of the distance from the grid. ..... 66

Figure 3.5 Projected images of the shock waves propagating through the grid turbulences for ($M_{s,L\text{-}tSW}$, $M$t) = (1.012 ± 0.001, 0.005 ± 0.001), (1.011 ± 0.001, 0.009 ± 0.001), and (1.009 ± 0.003, 0.014 ± 0.001). The central area from $y$ = 20 to 100 mm is extracted from the differential images. ..... 70

Figure 3.6 Projected images of the shock waves propagating through the grid turbulences for ($M_{s,L\text{-}tSW}$, $M$t) = (1.029 ± 0.001, 0.005 ± 0.001), (1.026 ± 0.001, 0.009 ± 0.001), and (1.021 ± 0.003, 0.014 ± 0.001). ..... 71

Figure 3.7 Projected images of the shock waves propagating through the grid turbulences for ($M_{s,L\text{-}tSW}$, $M$t) = (1.047 ± 0.001, 0.005 ± 0.001), (1.047 ± 0.003, 0.009 ± 0.001), and (1.047 ± 0.002, 0.014 ± 0.001). ..... 72

Figure 3.8 Projected images of the shock waves propagating through the grid turbulences for ($M_{s,L\text{-}tSW}$, $Mt$) = (1.105 ± 0.001, 0.005 ± 0.001) and (1.100 ± 0.001, 0.009 ± 0.001)..... 73

Figure 3.9 Projected images of the shock waves propagating through the grid turbulence for ($M_{s,L\text{-}tSW}$, $Mt$) = (1.150 ± 0.001, 0.005 ± 0.001) and (1.150 ± 0.002, 0.009 ± 0.001)..... 73

Figure 3.10 Example of detected shock edge from shadowgraph image for ($M_{s,\,L\text{-}tSW}$, $Mt$, $L_i/L$) = (1.021 ± 0.002, 0.014 ± 0.001, 124.6). ..... 75

Figure 3.11 $\beta$ versus $L_i/L$ for (a) $M_{s,L\text{-}tSW} \approx 1.01$, (b) $M_{s,L\text{-}tSW} \approx 1.02$–$1.03$, (c) $M_{s,L\text{-}tSW} \approx 1.05$, (d) $M_{s,L\text{-}tSW} \approx 1.10$, and (e) $M_{s,L\text{-}tSW} \approx 1.15$. Close symbols: results calculated using the shadowgraph image. Open symbols: results calculated using the schlieren image. ..... 78

Figure 3.12 $\delta/L$ versus $L_i/L$ for (a) $M_{s,L\text{-}tSW} \approx 1.01$, (b) $M_{s,L\text{-}tSW} \approx 1.02$–$1.03$, (c) $M_{s,L\text{-}tSW} \approx 1.05$, (d) $M_{s,L\text{-}tSW} \approx 1.10$, and (e) $M_{s,L\text{-}tSW} \approx 1.15$. Close symbols: results calculated using shadowgraph image. Open symbols: results calculated using schlieren image. ..... 84

Figure 3.13 $\delta/L$ versus dimensional interaction time $t_i/t_0$ for (a) $M_{s,L\text{-}tSW} \approx 1.01$, (b) $M_{s,L\text{-}tSW} \approx 1.02$–$1.03$, (c) $M_{s,LtSW} \approx 1.05$, (d) $M_{s,L\text{-}tSW} \approx 1.10$, and (e) $M_{s,L\text{-}tSW} \approx 1.15$. Close symbols: results calculated using the shadowgraph image. Open symbols: results calculated using the schlieren images. ..... 85

Figure 4.1 Example of an $x$–$t$ diagram of the CD-ST operation: $p_{4L}$ = 20.8 kPa, $p_1$ = 12.8 kPa, and $p_{4R}$ = 128.3 kPa. L-, from the left driver; R-, from the right driver; i, incident; t, transmitted; g, grid transmitted; r, reflected from the grid; SW, shock wave; EW, expansion waves; CS, contact surface. ..... 89

Figure 4.2 Schlieren images of the shock wave propagating through the grid turbulence. Arrows indicate the trajectory of the shock wave propagating at a constant velocity: (a) $M_{s,\,L\text{-}tSW}$ = 1.006, (b) $M_{s,\,L\text{-}tSW}$ = 1.013, (c) $M_{s,\,L\text{-}tSW}$ = 1.034, (d) $M_{s,\,L\text{-}tSW}$ = 1.046. ..... 93

Figure 4.3 Schematics of the 1D shock wave-forward induced-flow interaction: (a) before and (b) after. ..... 97

Figure 4.4 Schematic of $x$-element during the shock wave-turbulence interaction. ..... 98

Figure 4.5 Schematic of the $u$–$p$ diagram. ..... 98

Figure 4.6 Shock vanishment probability after one-time interaction $P$ ($m_x > M_{R,\,v}$) as a function of $M_s M_t$ / ($M_s^2 - 1$). Plots correspond to $M_{s,\,L\text{-}tSW}$ = 1.006 (circle), $M_{s,\,L\text{-}tSW}$ = 1.013 (triangle), $M_{s,\,L\text{-}tSW}$ = 1.034 (square), and $M_{s,\,L\text{-}tSW}$ = 1.046 (diamond), respectively. $M_t$ = 0.025 under all conditions. ..... 105

Figure 4.7 Schematic of shock formation by the integration of compression waves, as presented by Sasoh (2020). ..... 106

Figure 4.8 Ratio of shock formation distance to thickness of compression wave $L_s/\Delta x_c$ as a function of $M_s$. Plots correspond to the shock Mach numbers examined during the experiment. ..... 106

Figure 4.9 Shock vanishment probability in $n$ interactions with the velocity fluctuation. The interaction length for the integral scale of 10 mm is also shown in the horizontal axis. $M_t$ = 0.025 under all conditions and $M_{s,\,L\text{-}tSW}$ = 1.006 (circle), $M_{s,\,L\text{-}tSW}$ = 1.013 (triangle), $M_{s,\,L\text{-}tSW}$ = 1.034 (square), and $M_{s,\,L\text{-}tSW}$ = 1.046 (diamond). Regions indicated by a double arrow correspond to $L_i$, that is, where in the present experiment the shock wave front profile vanishes based on the schlieren images at $M_{s,\,L\text{-}tSW}$ = 1.006 (solid line) and $M_{s,\,L\text{-}tSW}$ = 1.013 (dashed line). ..... 108

Figure A.1 Opening process of polyester diaphragm at $\Delta p_{41}$ = 100 kPa ($p_4$ = 201.5 kPa and $p_1$ = 101.5 kPa). ..... 113

Figure B.1 Example of original velocity fluctuation signal measured by hot-wire anemometer. ..... 115

Figure B.2 Energy distribution of measured velocity signal. ..... 115

Figure B.3 Example of pdf of measured $u_x$'. Gray dotted line shows Gaussian profile. ..... 116

# List of Tables

Table 2.1 Petal states at the beginning of the inertial motion ($t = t_2$). The inclination angle of a diaphragm petal is $\theta$, angular velocity of a diaphragm petal is $\omega$, area-averaged petal velocity during the inertial motion is $v$p, and contact surface velocity is $u_c$. $u_c$ is calculated from initial pressures $p_4$ and $p_1$. ..... 45

Table 3.1 Measured shock wave and grid turbulence characteristics and the initial operation conditions ..... 62

# Nomenclatures

| | |
|---|---|
| $a$ | speed of sound |
| $A$ | area of diaphragm petal |
| $c_+$ | speed of characteristics |
| $D$ | cross-section length of shock tube |
| $e$ | thickness of diaphragm |
| $E$ | Young's modulus |
| $i$ | integer number |
| $I$ | moment of inertia of diaphragm petal |
| $k$ | decay constant of grid turbulence |
| $l$ | shortest distance between center of petal base and head of domain of influence |
| $L$ | integral scale of turbulence |
| $L_s$ | shock formation distance |
| $m$ | mesh size |
| $m_x$ | local Mach number of velocity fluctuation in $x$-direction |
| $M$ | Mach number of upstream flow of stationary shock wave |
| $M_R$ | flow Mach number in state R |
| $M_{R,v}$ | flow Mach number in state R for shock wave vanishment in interaction |
| $M_s$ | shock Mach number |
| $M_t$ | turbulent Mach number |
| $n$ | interaction times |
| $N$ | number of petals |

| | |
|---|---|
| $p$ | pressure |
| $P_n$ | shock vanishment probability in $n$ times interactions |
| $P()$ | probability function |
| $r$ | distance from center axis of shock tube |
| $R$ | radius of curvature of diaphragm |
| $Re_m$ | mesh Reynolds number |
| $Re_\lambda$ | turbulence Reynolds number |
| $s$ | arc length from center axis on surface of bulged diaphragm |
| $\bar{s}$ | average length of cracks measured on surface of bulged diaphragm |
| $t$ | time |
| $t_0$ | reference time defined as ratio of integral scale to velocity fluctuation |
| $t_1$ | time of crack propagation completion |
| $t_2$ | time from beginning of diaphragm opening until domain of influence covers entire diaphragm petal surface |
| $t_i$ | time after interaction |
| $u$ | velocity in $x$-direction |
| $u_c$ | velocity of contact surface |
| $u'$ | root-mean-square value of velocity fluctuation in $x$-direction |
| $u_x$ | $x$ component of velocity fluctuation |
| $U$ | mean flow speed |
| $v_c$ | speed of crack propagation |
| $\overline{v_p}$ | averaged velocity of rotating petal |
| $x, y, z$ | Cartesian coordinate |
| $x_0$ | initial bulge of diaphragm |

$x_a$ location of leading head of compression waves

$x_b$ location of tail of compression waves

$\alpha$ opening area ratio of diaphragm

$\beta$ discontinuity ratio of side projected shock wave

$\gamma$ specific heat ratio

$\Delta x$ coordinate system from grid position

$\Delta x_c$ thickness of bundle of compression waves

$\Delta p$ overpressure

$\Delta p_{41}$ pressure difference between driver and driven section

$\Delta p_p$ pressure difference acting on petal

$\delta$ averaged side projected thickness of shock wave

$\varepsilon$ base angle of diaphragm petal

$\theta$ inclination angle of petal

$\lambda$ Taylor micro scale

$\mu$ Poisson ratio

$\nu$ kinetic viscosity

$\rho$ density

$\rho_c$ density of cellophane diaphragm

$\sigma_i$ initial strain stress acting on diaphragm

$\sigma_c$ minimum strain stress for generating multiple cracks

$\tau$ effective opening force period on diaphragm petal

$\tau_e$ effective opening force period on diaphragm petal used in best fitting

$\varphi$ relative humidity

$\chi$ constant in petal formation law

$\psi$ Mach angle of the domain of influence by Mach wave

$\omega$ Angular velocity of diaphragm petal

Subscripts:

0 stationary state

1 driven section

4 driver section

4L left driver section

4R right driver section

GT grid turbulence region

L behind shock state

$L^*$ state behind left-running wave after interaction

R forward induced flow state

$R^*$ state behind right-running wave after interaction

*t* turbulence region

# Chapter 1

# Introduction

## 1.1 Problems related to shock waves in aerospace engineering

A shock wave is a symbolic phenomenon in compressible fluids. In aerospace engineering, where high-speed flow often occurs, shock waves appear in various situations. Because instantaneous compression by a shock wave increases entropy (Landau and Lifshitz, 1987), appropriate control of shock waves is required to improve efficiency. In particular, supersonic and hypersonic flights always struggle with aerodynamic problems related to shock waves. Realization of these new generation transportation means could contribute to the innovative values in human society and reduce transportation time. However, the complex behaviors of shock waves in non-uniform fluid fields render difficulty in aerodynamic problems and prevent sustainable operations.

A sonic boom is a serious problem caused by rapid compression by a supersonic flight vehicle. The sonic boom is an explosion-like loud noise heard on the ground owing to its two sudden pressure increases represented as an “N-wave” (Maglieri et al., 2014). The unpleasant noise affects human activities, and in worse cases, structures such as windows are broken. Furthermore, the overpressure characteristics of the sonic boom, such as the

peak value of overpressure and the pressure risetime, are locally changed by atmospheric turbulence existing between the supersonic flight path and ground. Supersonic flight tests conducted in the past by the National Aeronautics and Space Administration (NASA) revealed that the overpressure history measured at multiple points on the ground considerably varied (Kane, 1972). Subsequently, researchers investigated the effects of atmospheric turbulence on the overpressure characteristics of the sonic boom by simplified laboratory experiments (e.g., Lipkens and Blackstock, 1998) and numerical simulations (e.g., Kanamori et al., 2021). To determine the operational rules of supersonic flight above the ground, the effect of atmospheric turbulence on the changes in overpressure by the sonic boom must be clarified.

In supersonic flight, the engine intakes air in a supersonic state and transfers it to the propulsion system; subsequently, a diffuser is employed to slow this supersonic air down to a subsonic state. From a compressible fluid dynamics viewpoint, supersonic flow cannot be decelerated to subsonic flow while preserving entropy: the supersonic flow must be compressed by shock waves (Shapiro, 1953a). Thus, the diffuser is designed to generate multiple weak oblique shock waves and compress air without considerably increasing the entropy (Strack and Morris Jr., 1988). In the process, the shock waves interact with a boundary layer developed from the wall; this phenomenon is called a shock wave-boundary layer interaction (SWBLI) (Clemens and Narayanaswamy, 2014). In the boundary layer, the pressure waves can propagate upstream because the flow speed in the boundary layer is subsonic. This causes undesirable complex shock wave behaviors in the internal flow field, thereby leading to serious problems, such as a reduction in operating conditions and efficiency deterioration (Trapier et al., 2006).

Scramjet (supersonic combustion ramjet) is a developing technique that attempts to

take place a combustion process and obtain thrust in supersonic airflow (Ferri, 1973; Curran et al., 1996). This method enables efficient high-speed operation because the propulsion system does not have to slow down the supersonic flow. However, completing the combustion process in supersonic or hypersonic flow involving multiple shock waves is challenging. Therefore, the mixing process by shock waves should be clarified to enhance mixing efficiency.

To offer solutions for these shock-related aerodynamic problems in applicational situations, the shock wave behaviors in complex flow fields should be well understood. Therefore, the abovementioned aerodynamic phenomena should be investigated in reasonably simplified configurations, and essential parts of shock wave behavior should be extracted. To understand the interaction of shock waves with complex flow fields (atmospheric turbulence, boundary layers, and fuel jets), an interaction between a shock wave and turbulence (shock–turbulence interaction) has been investigated as the most fundamental configuration (Andreopolous et al., 2000). In the next section, the related academic work of shock–turbulence interactions are reviewed.

## 1.2 Related studies on shock–turbulence interactions

### 1.2.1 Effect of shock waves on turbulence

In a shock–turbulence interaction, velocity fluctuation is amplified and length scales are changed in turbulence owing to the instantaneous compression of a shock wave. These phenomena directly affect mixing, one of the most important features of turbulence in engineering. Budzinski et al. (1992) reported that the enhancement of mixing by shock waves could be applied to the combustor of hypersonic vehicles. Therefore, numerous

researchers have investigated the effects of shock waves on turbulence characteristic changes for a long time.

Keller and Merzkirch (1990) used a shock tube with grid turbulence and a shock wave reflected at the end wall. They measured the density fluctuations using speckle photography and reported an amplification in the turbulence intensity at lower wave numbers in the spectrum. Honkan and Andreopoulos (1992) conducted an experiment on the interactions of a planar shock wave with grid-generated turbulence in a shock tube. They developed a hot-wire measuring technique for shock tube flow and found that the amplification of the root-mean-square value of velocity fluctuations and its gain ratio depended on the upstream isotropic turbulence characteristics. This finding was confirmed using a similar experimental device (Briassulis et al., 1996; Agui et al., 2005). In another experimental system, Barre et al. (1996) studied an interaction between a planar shock and quasi-homogeneous isotropic turbulent supersonic flow at Mach 3. They reported that the shock wave increases the longitudinal fluctuating velocities and decreases the longitudinal integral scales. Recently, McManamen et al. (2021) measured velocity and temperature fluctuation using molecular tagging velocimetry (MTV) and two-line planar laser induced fluorescence (PLIF) in a pulsed wind tunnel at Mach 4.4. They reported that the temperature fluctuation amplification factor was between 3.0 and 4.5.

Improvements in the computing capacity and development of numerical simulation methods enable numerical simulations of the interaction between a planar shock wave and isotropic turbulence to be conducted. Direct numerical simulation (DNS) has primarily been used to understand shock–turbulence interaction problem. In studies involving DNS, the characteristic change in turbulence, including very strong

compressible turbulence, have been investigated (Lee et al., 1993; Larsson and Lele, 2009; Larrson et al., 2013; Ryu and Livescu, 2014; Chen and Donzis, 2019). These DNSs confirmed the experimental results of the amplification of turbulence velocity fluctuations and the change in scales of turbulence. Additionally, important changes in the shock wave affected by turbulence were reported in these DNS studies, as summarized later.

### 1.2.2 Effect of turbulence on the post-shock pressure field

Modulation of post-shock overpressure is important for numerous engineering applications, such as the sonic boom behavior while passes through atmospheric turbulence and behavior of the blast wave in the far field. To predict the effect of a modulated shock wave on humans and buildings, understanding overpressure modulation characteristics caused by a nonuniform flow field is crucial.

Lipkens and Blackstock (1998) conducted a model laboratory experiment of sonic boom propagation through atmospheric turbulence. The sonic boom was imitated by an N-wave induced by an electric spark source, and the turbulence was generated by a plain jet. Their experiments were conducted multiple times and indicated that the peak pressure and rise time of the N-waves were considerably scattered by interacting with the plane jet. Kim et al. (2010) generated a spherical shock wave using an Nd:YAG laser breakdown and by allowing the shock to pass through a turbulent slit jet. They obtained distinct relationships between the overpressure history and visualized shock front deformation. The peak overpressure was increased when the shock front was flattened, whereas it decreased when humped. Sasoh et al. (2014) demonstrated an interaction between a spherical shock generated by an open-ended shock tube and grid turbulence in a wind tunnel. They found that the impact of the turbulence on the standard deviation of the peak

post-shock overpressure was much larger than that of its ensembled average. Using a similar experimental device, Inokuma et al. (2017) simultaneously measured overpressure and velocity of the grid turbulence; they found that the shock modulation was induced by the large-scale turbulent motion. Additionally, they statistically investigated the peak overpressure of the shock wave in grid turbulence and discussed the effects of a shock and turbulent Mach number on the averaged peak overpressure (Inokuma et al., 2019). Tamba et al. (2016) conducted a field experiment of the interaction between a blast wave and grid turbulence using a gunpowder explosion and grid turbulence. They found that the effect of turbulence on peak overpressure was seven times that of non-turbulence.

In the abovementioned studies, spherical shock waves were used, whereas, in a shock tube, a planar shock wave, which is a much simpler type of shock wave, can be obtained. Dosanjh (1956) experimentally visualized the wave front of the planar shock wave fluctuating owing to the interaction with grid turbulence using a shock wave with shadowgraph visualization. Xanthos et al. (2002) conducted an experiment on a planar shock wave reflected from an end wall with grid-generated turbulence in a shock tube. The variation in the post shock pressure of the planar shock wave owing to its interaction with grid turbulence was investigated. Using DNS, Tanaka et al. (2018 and 2020) studied the relation between planar shock wave deformation and the change characteristics of overpressure of the deformed shock wave.

### 1.2.3 Effect of turbulence on the shock wave structure

The deformation of a shock wave is a common outcome of shock–turbulence interactions. In studies involving DNS, the shock wave structure in the interaction

between a planar shock wave installed in a supersonic flow and isotropic turbulence has been investigated. Lee et al. (1993) first reported an interaction regime, where shock waves no longer had well-defined fronts in DNS. This finding was remarkable because, in the classical theory of linear interaction analysis (LIA) of the shock–turbulence interaction (Ribner, 1954), the shock wave was assumed to always maintain its discontinuous structure. They suggested $M_t^2 > 0.1\ (M^2 - 1)$ as the interaction regime where shock waves that no longer have a front occur. Here, $M_t$ is a turbulent Mach number (a value obtained by dividing the root-mean-square value of velocity fluctuation of turbulence by the speed of sound in the turbulence), and $M$ is a flow Mach number of the upstream flow of the stationary shock wave. Subsequently, Larsson and Lele (2009) categorized the regimes in the shock–turbulence interaction into the "wrinkled shock" regime, in which the discontinuity of the shock wave is maintained although it deformed, and "broken shock" regime, in which locally continuous parameter changes appear to the shock wave front; they suggested $M_t^2 > 0.06\ (M^2 - 1)$ as a predictor of the broken shock regime. Larsson et al. (2013) studied a wide range of interactions and proposed $M_t > 0.6\ (M - 1)$ as a more precise criterion for the broken shock regime. Simultaneously, Donzis (2012) derived the same criterion from theoretical analysis. He assumed that the upstream turbulent flow of the shock wave follows the Gaussian velocity field and computed a ratio of locally subsonic flow. Chen and Donzis (2019) confirmed that this assumption is appropriate using DNS. Further, they reported a "vanished" regime as a new type of interaction regime, where the location of the shock wave front could not be easily defined entirely. This "vanished" regime occurred when the shock wave was weak and turbulence was strong.

## 1.3 Objective of this thesis

Among the aforementioned important features of the shock–turbulence interaction, this thesis focuses on the modulation and moderation of a planar shock wave front, which is the most fundamental type of shock wave, during its interaction with turbulence. We believe that fundamental understanding of the changes in a planar shock wave front and consequent pressure modulations by turbulent flow will aid in reliably predicting the noise level of a sonic boom affected by atmospheric turbulence and developing innovative methods to efficiently control the shock wave strength.

Earlier research has revealed that deformation of a planar shock wave considerably affects the shock–turbulence interaction (Lee et al., 1993; Larsson and Lele, 2009; Kim et al., 2010; Larsson et al., 2013; Tanaka et al., 2018 and 2020; Chen and Donzis, 2019). However, regarding the regime of the shock–turbulence interactions, previous studies have the following limitations:

A) The regimes of shock–turbulence interactions have only been investigated using DNS.

B) The “broken” and “vanished” regimes have been obtained only for intensive turbulence conditions.

C) The mechanism leading to the “vanished” regime during the interaction is unclear.

Let us first evaluate A). In numerical simulations, a shock wave is approximated as a thin continuous profile because a finite length is required to express the shock wave in the simulation. This assumption deviates from the structure of an actual shock wave, whose thickness is extraordinarily small (the same order to the mean free path of gas). In addition, regarding the numerical setup in the DNS, to simulate the interaction between the stationary planar shock wave and isotropic turbulence, the boundary conditions,

including the turbulence effect (Lele, 1992), are applied based on the Rankine–Hugoniot equations. If these conditions are not applied, the shock wave unstably moves in the calculation domain, a phenomenon called “shock drifting” (Larrson et al., 2013). That is, an artificial external force acts on the shock wave to maintain its location. Therefore, these earlier studies were conducted on the assumption that the shock wave remains stationary; this assumption is different from the real situation. Thus, the results obtained by the numerical simulation cannot be guaranteed to be applied to real phenomena. Additionally, the obtained characteristic changes in the shock wave and turbulence are the results from the “steady” state of the shock–turbulence interaction. Therefore, the unsteady modulation and moderation of a shock wave propagating through turbulence and the mechanism through which the shock wave settles into a steady state remains unclear.

Regarding B), the DNS studies examined the strong turbulence condition to investigate shock wave deformation: turbulent Mach number $M_t$ in these studies is typically greater than 0.1. This range of turbulence is not frequently observed in the atmosphere. For example, according to measurements using a radiosonde, the averaged wind speed in the troposphere is 9.55 m/s in the height from 0 to 11 km (Takahashi et al., 2018). If we assume the temperature as 300 K, $M_t = 0.028$ is obtained. Thus, the shock–turbulence interactions must be investigated under these weak turbulence conditions to address the real phenomenon. However, whether a broken and vanished regime occurs in an interaction between a weak shock wave and weak turbulence has not been investigated. To answer this question, a wide range of conditions of the shock wave and turbulence should be examined. However, the constraints of experimental facilities make performing these examinations difficult.

Topic C) is about the vanished regime of the shock wave. This new regime has been reported in just one recent DNS study (Chen and Donzis, 2019), and the criterion for occurrence has not been proposed yet. The understanding of this regime is important because the vanished regime shows the possibility of mitigation of the shock wave by the interaction of the flow field.

The objective of this thesis is to tackle these limitations in shock–turbulence interactions and provide novel insights. Regarding topic A), we conduct experiments between the planar shock wave and grid turbulence. To establish the experiment, the first part of this thesis focuses on a generation method for shock wave. In general, generating a shock wave depends on an opening process of diaphragm that separates a driver and driven gases (e.g., White, 1958). The objective of this part is to understand the characteristics of shock wave generation in a shock tube for the following experiment of the shock–turbulence interaction. Then, the experiments between the planar shock wave and grid turbulence are conducted by a counter-driver shock tube (CD-ST) (Tamba et al., 2015). The experimental investigation in the CD-ST is expected to provide novel insights into shock–turbulence interactions. First, the experimental investigation enables the validation of the results obtained by DNS studies. As aforementioned, the shock wave is approximated as a continuous profile in numerical simulations. By conducting experimental investigations, this thesis aims to validate the DNS studies and offer insight into the physics in shock wave deformations. Second, the experiments performed can overcome the problem of unphysical boundary conditions. In the CD-ST, the planar shock wave and grid turbulence can be generated by an independent driving force. We can evaluate the shock wave unsteadily propagating through grid turbulence, without an artificial force applied to the shock wave. Because the planar shock wave does not change

properties by itself during propagation, pure effects of unsteady propagation through turbulence on the shock wave can be investigated. Although a similar system can be obtained in DNS (Tanaka et al., 2020), their research was conducted under limited shock wave and turbulence conditions. Further investigations are still required.

Regarding topic B), this thesis parametrically evaluates the effects of parameters in shock–turbulence interactions, such as the shock and turbulent Mach number, on shock wave deformations. The weak turbulence effect ($M_t \leq 0.025$) on the modulation and moderation of the shock wave profile is examined in this thesis, which has not been investigated earlier. The experimental validation of the "broken" and "vanished" shock regime in the shock–turbulence interaction, under weak shock wave and weak turbulence conditions, is also an important objective of this thesis.

Regarding topic C), this thesis aims to experimentally validate the "vanished" regime and give a physical understanding by expanding a fundamental shock wave interaction theory (the Riemann problem).

## 1.4 Structure of this thesis

In Chapter 2, as preparation for the shock–turbulence interaction experiments, investigations of a cellophane diaphragm rupture process and its impact on the shock wave formation in a shock tube are conducted. The process of a tensioned cellophane diaphragm is observed using high-speed visualization, and the petal formation law, which can predict diaphragm stress condition where a shock wave can be successfully generated, is obtained. Finally, we conclude that the opening process of the cellophane diaphragm is suitable for weak shock formation in a short shock formation distance.

In Chapter 3, interactions between a planar shock wave and grid turbulence are

conducted using a counter-driver shock tube. The shock wave propagating through the turbulence is visualized using the shadowgraph and schlieren method, and the effects of the shock Mach number, turbulent Mach number, and the interaction length on the shock wave front profile are evaluated. An unsteady increase in the side projected thickness of the shock wave is discussed. Moreover, the broken regime is experimentally obtained when the shock wave is weak after traveling a sufficient interaction length.

In Chapter 4, the vanished regime of the shock wave is investigated in an experimental and theoretical manner. In the experiment, losing the shock wave front profile during propagation through turbulence is obtained on images using schlieren visualization. Based on the Riemann problem, a condition where the shock wave changes into expansion waves is derived for a one-dimensional system. By expanding that to a multidimensional system, a new criterion for the vanished shock regime is derived.

# Chapter 2

# Experimental law in cellophane diaphragm rupture processes and its impacts on shock tube performance

## 2.1 Introduction of this chapter

### 2.1.1 Introduction to shock tubes

A shock tube is the most fundamental experimental device for generating a planar shock wave, which is the simplest form of shock waves. A diaphragm separates the long tube inside a shock tube into two sections: driver and driven. High- and low-pressure gases are filled in the driver and driven sections, respectively. On the rupture of the diaphragm, the high-pressure gas abruptly compresses the low-pressure gas, and a planar shock wave propagates in the driven section. Shock tubes have been used in various fields of science and engineering, e.g., fundamental shock wave physics, shock wave reflections, dynamic responses of materials, and chemical reactions. In this thesis, we use a shock tube to investigate the behavior of shock waves interacting with turbulence, and the results are discussed in Chapters 3 and 4. This chapter describes the experimental examination of the fundamental operation of a low-pressure shock tube, conducted as a preliminary study for the subsequent shock–turbulence interaction experiments.

### 2.1.2 Effect of diaphragm rupture on shock wave formation

The strength of a shock wave and its associated flow conditions in an ideal shock tube operation are straightforwardly obtained from the initial conditions using inviscid shock tube relations based on the Rankine–Hugoniot equations (Shapiro, 1953b; Liepmann and Roshko, 1957; Glass and Sislian, 1994). However, in an actual shock tube operation, the viscosity, heat transfer, and diaphragm rupture processes should be carefully considered. Among these processes, diaphragm rupture typically affects the shock wave formation and flow field.

White (1958) investigated the effect of the diaphragm opening time on strong shock wave formation in a shock tube using a stainless-steel diaphragm. Petrie-Repar and Jacobs (1998) obtained similar results by numerical simulation. Simpson et al. (1967) measured the opening time of a 0.55-millimeter-thick brass diaphragm and demonstrated that a shorter opening time resulted in a shorter shock formation distance.

The diaphragm opening morphology also significantly affects the flow in a shock tube. Yang (1995) reported that a shock wave weakens with the reduction in the cross-sectional area ratio of the diaphragm of a shock tube, based on theoretical analysis. Gaetani et al. (2008) investigated, both experimentally and numerically, the performances of shock tubes with various diaphragm opening area ratios. They confirmed that shock strength decreased with decreasing opening ratio of the diaphragm. They also evaluated the disturbance characteristics in the shock tubes and proposed a simple analytical model for reducing the local frequency disturbance. Houas et al. (2012) showed that compression waves do not coalesce in a shock tube with an opening area ratio smaller than 0.5.

### 2.1.3 Objective of this chapter

The abovementioned previous research dealt with relatively strong shock waves and used metal diaphragms to sustain the large pressure difference before diaphragm rupture. On the other hand, for generating a weak shock wave with a shock Mach number smaller than 1.1, a diaphragm formed of a light and brittle material is preferred to ensure diaphragm opening under a relatively smaller pressure difference. However, such a diaphragm causes a crucial problem in shock tube experiments because it needs a long time to open. In one-dimensional analysis, the shock wave formation distance, $L_s$, of compression waves, whose time derivative of pressure under the initial conditions is $(\partial p/\partial t)_{t=0}$, can be estimated as follows (Sasoh, 2020):

$$L_s = \frac{2\gamma}{\gamma+1}\frac{p_0 a_0}{\left(\frac{\partial p}{\partial t}\right)_{t=0}} \tag{2.1}$$

where $\gamma$ is the specific heat ratio and $p_0$ and $a_0$ are the pressure and speed of sound in front of the head of the compression waves, respectively. This equation shows that the shock formation distance is proportional to the diaphragm opening time and the inverse of the pressure increase. Thus, the shock formation distance for a weak shock increases not only with a small pressure increase but also with the diaphragm opening time increase in a shock tube.

The experiments presented in this thesis had to handle this problem. We used a counter-driver shock tube (CD-ST) in shock–turbulence interaction experiments, which are discussed subsequently. The CD-ST had two counter drivers on both sides of the driven section. Therefore, the distance between the diaphragm and the test section was limited compared to that in a conventional single-driver shock tube. Moreover, the behavior of weak shock waves interacting with turbulence was a crucial aspect of the

study presented in this thesis. Therefore, to conduct the shock–turbulence interaction experiments under wide conditions in the CD-ST, the effect of the opening process of a diaphragm on the shock wave formation needed to be clarified. In this study, cellophane was employed as the diaphragm material. To generate weak shock waves, cellophane has been empirically adopted as the diaphragm material owing to its light and thin features (Henshall, 1955; Ikui and Matsuo, 1969; Ikui et al., 1969; Tamba et al., 2015). However, the opening process of the cellophane diaphragm has not been sufficiently investigated. Under humid experimental conditions, the author of the present thesis observed an incomplete opening of a cellophane diaphragm, which resulted in the deterioration of shock formation. Therefore, the objectives of the study presented in this chapter were to clarify the opening process of a cellophane diaphragm by high-speed imaging and investigate the effect of the opening process on the formation of a weak shock wave.

## 2.2 Experimental setup

### 2.2.1 Shock tubes

Figure 2.1 shows the experimental setups used in the study. Two types of stainless-steel shock tubes with square cross-sections were used. The length of the side square cross-section, $D$, were 62 and 120 mm, and the lengths of the driver section were 515 and 1020 mm, respectively. Those of the driven section were changed depending on the objectives of the experiments (visualization of diaphragm opening process or measurement of the overpressure). To separate the driver and driven gases, a one-layer cellophane diaphragm was used. A layer of a “white” cellophane film (Futamura Chemical Co. Ltd., PC5-W #300) with a thickness $e$ of 21 μm was used to enhance the

visibility of the diaphragm opening process. The mechanical properties of the white cellophane film were largely similar to those of a plane one without any additive or surface coating (Futamura Chemical Co. Ltd., PL #300). Specifically, the differences in their measured tensile strengths and elongations were approximately 6% and 4%, respectively. Therefore, the experiments were conducted using the white cellophane film; however, the results obtained in this research can also be applied to the widely used plain cellophane. We adopted an active diaphragm rupture system using a needle driven by a pneumatic piston controlled by electronic signals. This system was introduced into a counter-driver shock tube, in which the relative diaphragm rupture timing of the driver should be controlled precisely (Tamba et al., 2015). To drive the pneumatic cylinder (SMC Co., CJ2B10-60AZ), high-pressure air was supplied by two 4.00-millimeter-thick polyurethane tubes using a feedthrough installed on the driver channel to actuate the needles. These tubes were connected to a high-pressure air bottle via a five-port electromagnetic valve (SMC Co., SY-3220). Valves on the upper and end walls of the driver channel were also connected to a Bourdon pressure gauge and attached to the driver air supply from a compressor. The initial pressures in the driver and driven sections are denoted as $p_4$ and $p_1$, respectively. The driver was supplied with dry compressed air using a dryer (SMC Co., ID300-04) and a compressor (ANEST IWATA Co., TFP04C-10C) through which atmospheric air was passed. The temperature and relative humidity, $\varphi$, of the driven section were recorded using a thermo-hygrometer immediately before the diaphragm rupture. Because atmospheric conditions in the laboratory exhibited everyday alterations, the relative humidity of the driven section was passively set in a range of $20.0\%\text{RH} \leq \varphi \leq 76.6\%\text{RH}$. The accuracies of the temperature and relative humidity measurements were ±1 K and ±5%RH, respectively.

### 2.2.2 Visualization systems

Figures 2.1 (a) and (b) show the schematically show the setups for the visualization of the diaphragm rupture process. As shown in Fig. 2.1 (a), we set the origin, *O*, at the diaphragm center before its bulge. The *x*-axis is defined from *O* toward the right along the central axis of the driven section, the *y*-axis is from *O* toward the depth direction in the sideview, and the *z*-axis points upward. The distance, *r*, is considered from the central axis (see Fig. 2.1 (a) and 2.2). *s* is the arc length from the top of the bulged diaphragm (see Fig. 2.1(a)).

Setup I (see Fig. 2.1 (a)) was used to capture the crack-propagation process during a relatively early stage of the diaphragm rupture. The diaphragm was illuminated by a strobe light (Panasonic, PE-60SG) installed off the central axis of the shock tube. The diaphragm rupture process was visualized using a high-speed camera (SHIMADZU co., HPV-1) set along the axis of the driver channel. This setup had a resolution of 312 × 260 pixels and a framing rate of $5 \times 10^5$ fps with an exposure time of 1 μs.

Setup II (see Fig. 2.1 (b)) was used for capturing the opening motion of the petals of the ruptured diaphragm. The frame rate of the high-speed camera (SHIMADZU Co., HPV-1 or nac Image Technology Inc., ULTRA Cam) was set as 3.2–4.0 × $10^4$ fps (time interval was 32–25 μs) and the exposure time was 3–16 μs. To replicate an actual shock tube operation, the driven section was installed on the low-pressure side. A transparent acrylic endplate was installed at the end of the driven section. The feedthrough port on the top surface of the driven section was kept open until immediately before the diaphragm rupture. Therefore, the initial conditions of the gas in the driven section were equivalent to those of the laboratory atmosphere (pressure, temperature, and humidity), as in Setup I. For Setup II, the strobe light source was the same as used as in Setup I.

### 2.2.3 Overpressure measurement

Setup III (see Fig. 2.1 (c)) was used to measure the overpressure histories of the shock waves in a long driven channel. Pressure transducers (113B27, PCB Piezotronics Inc.; rise time 1 μs) were flush-mounted on the upper wall of the shock tube.

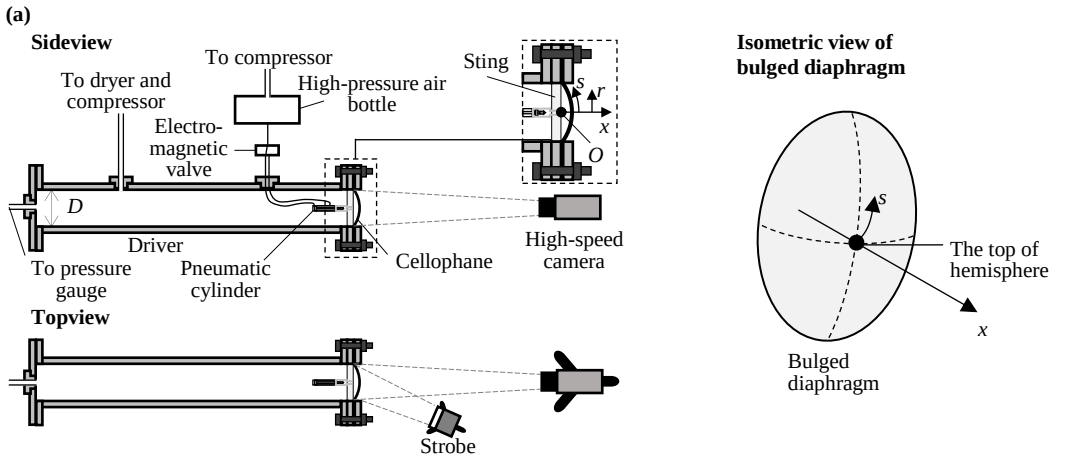


(a)

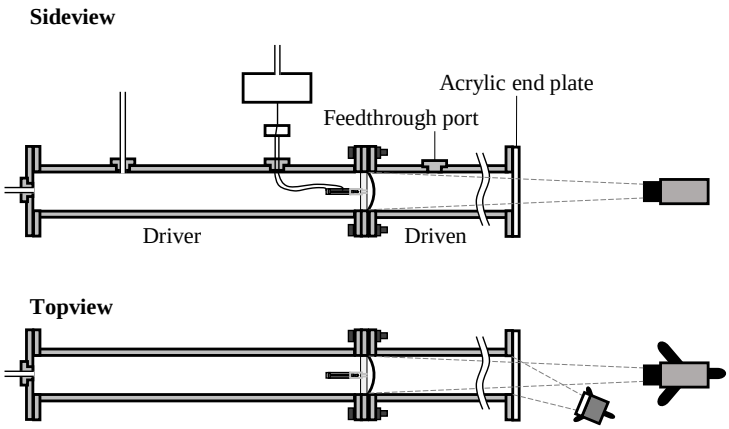


(b)

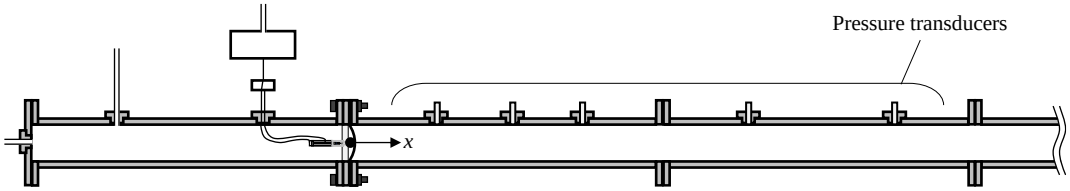


(c)

Figure 2.1 Experimental setups. (a) Setup I for visualizing crack propagation. (b) Setup II for visualizing the complete opening process of the cellophane diaphragm in the shock tube. The strobe light source is omitted in the sideview. (c) Setup III for the overpressure measurement.

## 2.3 Cellophane diaphragm rupture

### 2.3.1 Strain stress acting on cellophane diaphragm

To consider the fragmentation process of a tensioned thin membrane, evaluating the strain and the stress before fragmentation is important (Moulinet and Adda-Bedia, 2013). We calculated the tensile stress acting on the cellophane diaphragm subjected to a pressure difference by displacement. The displacement of the diaphragm was measured by changing $p_4$ and $\varphi$ using Setup I. The measurement results revealed that the diaphragm was deformed into an almost spherical shape. Thus, by measuring displacement at the center of the diaphragm, $x_0$ (on the $x$-axis), and assuming a zero displacement at ($y$, $z$) = (0, ± $D$/2) and (± $D$/2, 0), we obtained the spherical shape of the diaphragm with a radius of curvature $R$. The tensile stress $\sigma_i$ [Pa] acting on a partial spherical diaphragm with a thickness $e$ under a pressure difference $\Delta p_{41}$ (= $p_4 - p_1$) is calculated as follows (Roark, 1938):

$$\sigma_i = \frac{\Delta p_{41} R}{2e} \tag{2.2}$$

The error in $\sigma_i$, estimated by the measurement errors of $x_0$ and $\Delta p_{41}$ was approximately 2%. The maximum $\sigma_i$ used in this research was 68.7 MPa.

The bulge at the center of the diaphragm, $x_0$, varied depending on the pressure difference and humidity on the low-pressure side. Specifically, it increased with humidity for the same pressure difference and with the pressure difference for the same humidity, on the low-pressure side. The former trend was consistent with the technical data of the mechanical properties of the cellophane diaphragm provided by the cellophane manufacturer, i.e., its elongation of the cellophane diaphragm increases with the relative humidity, and tensile strength decreases with relative humidity (Futamura Chemical Co.

Ltd., private communication, 2021). If the compressibility of the material is ignored, the strain of a diaphragm can be estimated as the ratio of the stretched length to the length in the original state. In this study, the minimum strain was 0.011 and the maximum was 0.42. For natural rubber (Moulinet and Adda-Bedia, 2013), the measured strain has been found to be $7.0 \pm 0.5$, indicating that the studied cellophane diaphragm was very brittle.

### 2.3.2 Crack propagation process in cellophane diaphragm

In the early stage of the diaphragm opening process, high-speed crack propagation was observed. Examples of sequence images of the crack propagation observed using Setup I are shown in Fig. 2.2. The results obtained with the cross-section size, pressure, humidity, and temperature of $D$ = 62 mm, $p_4$ = 140.9 kPa, $p_1$ = 100.9 kPa, and $\varphi$ = 35.0%RH are shown in Fig. 2.2 (a). The images captured under $D$ = 120 mm, $p_4$ = 121.5 kPa, $p_1$ = 101.5 kPa, and $\varphi$ = 41.5%RH are shown in Fig. 2.2 (b). The calculated tensile stresses under these conditions were $\sigma_i$ = 54.8 MPa (Fig. 2.2 (a)) and 54.1 MPa (Fig. 2.2 (b)), respectively. The frame immediately before the first crack was identified and set as $t$ = 0 μs. The time, $t$, had an uncertainty of 2 μs owing to the frame interval. The crack propagated from the center of the diaphragm immediately after needle impingement. As the distance from the origin increased, crack branching was observed. This high-speed crack propagation has not been observed in aluminum and copper diaphragms (Campbell et al., 1965; Rothkopf and Low, 1974). We also visualized a polyester diaphragm (see Appendix A); however, we did not observe high-speed multiple crack propagation in the early stage of the diaphragm opening.

The crack front positions were manually extracted from Fig. 2.2 every 10 μs, and the results are shown in Fig. 2.3. The propagation speed of the crack front under these

conditions remained unchanged. Figure 2.4 shows the time evolution of the averaged crack length on the arc of the diaphragm, $\bar{s}$. The effects of the differences in the shock tube scale, pressure, and low-pressure section humidity on the crack propagation speed were examined. For $\varphi$ = 53.7, 76.6%RH, and $D$ = 120 mm, the experimental results obtained with Setup II were used. As the time resolution of Setup II was 32 or 25 μs, the time, $t$, was synchronized by comparing the images of the first crack appearance with the results obtained under the same pressure difference but different humidity values. In Fig. 2.2, saturated regions of brightness exist on the left-hand side ($-20 < y < -10$ in Fig. 2.2 (a)) and right-hand side of the diaphragm ($20 < y < 40$ in Fig. 2.2 (b)). Therefore, $\bar{s}$ was calculated using the crack fronts at $y > 0$ in Fig. 2.2 (a) and $y < 0$ in Fig. 2.2 (b). As shown in Fig. 2.4, $\bar{s}$ increases linearly with time, i.e., the crack speed is constant. Under the low-pressure condition ($\Delta p_{41}$ = 3.0 kPa), a single crack was generated (subsequently shown in Fig. 2.5 $\sigma_i$ = 20.0 MPa), and its propagation speed was lower than that under the other condition (619 m/s). Under this condition, the initial stress appeared to be insufficient to fully accelerate the crack. Under the other conditions, multiple cracks were generated, and a constant crack front propagation speed was obtained regardless of $D$, $\Delta p_{41}$, and $\varphi$. The average crack speed $v_c$ was 855 ± 37 m/s. This crack propagation speed should be compared with the longitudinal and shear wave speeds. In this study, we calculated the longitudinal and shear wave speeds of the cellophane diaphragm. Using Young's modulus, $E$, and Poisson's ratio, $\mu$, of the material by assuming a bulk state, the longitudinal and shear wave speeds can be expressed as $\sqrt{E(1-\mu)/\{\rho_c(1+\mu)(1-2\mu)\}}$ and $\sqrt{E/\{2\rho_c(1+\mu)\}}$, respectively, where $\rho_c$ (= 1460 kg/m$^3$) is the density of cellophane. According to the cellophane manufacturer, $E$ for cellophane with a humidity of

approximately 60%RH is $E \approx 4.42$ GPa. However, we obtained a value of $E \approx 3.2$ GPa from the elastic range of the stress–strain curve (0.25% stretch at 80 MPa) presented in an earlier study using plain cellophane (Zhang et al., 2015). We assumed $\mu$ as 0.3–0.4, similar to those of other polymer materials. Consequently, using $E \approx 4.42$ and 3.2 GPa, the longitudinal wave speeds were calculated as 2269–2806 m/s and 1930–2387 m/s, respectively. Correspondingly, the shear wave speeds were estimated as 1402–1455 m/s and 1194–1239 m/s. Therefore, the difference of 1.2 GPa in $E$ obtained by the two approaches caused differences of 339–419 m/s and approximately 200 m/s in the longitudinal and shear wave speeds, respectively. It can be concluded that the crack propagation speed obtained experimentally was approximately 30–38% longitudinal wave speed and 59–61% shear wave speed on employing the value supplied by the manufacturer. It was 36–44% longitudinal wave speed and 69–72% shear wave speed on using the value of Zhang et al. (2015).

In a molecular dynamics simulation conducted by Martín et al. (2000), a branching instability occurred when the crack speed reached a critical crack tip speed. This speed was estimated at 70% that of a wave propagating near the surface (the Rayleigh wave), which in turn is approximately 90% of the shear wave speed (Landau and Lifshitz, 1986). Thus, the critical point of crack speed is approximately 63% of the shear wave speed. In our experiment, the crack propagation speed with branching was estimated at 59–72% of the shear wave speed, correlating with the prior figure. However, the Young's modulus $E$ of the cellophane was assumed to be constant throughout our analysis. Because the stress–strain relationship was affected by humidity, $E$ and the wave speeds must likewise be influenced by the humidity effect. However, the measured crack propagation speed was constant. To clarify the relationship between the change in physical properties and

constant crack propagation speed, further investigation is necessary.

We now examine differences among materials. Prior studies using highly tensioned natural rubber reported a constant crack propagation speed with branching (Moulinet and Adda-Bedia, 2013) through an experiment conducted in a single length-scale of the experimental device. The present study confirmed a constant crack propagation speed even given changes in experimental device length, pressure difference, and humidity on the low-pressure side.

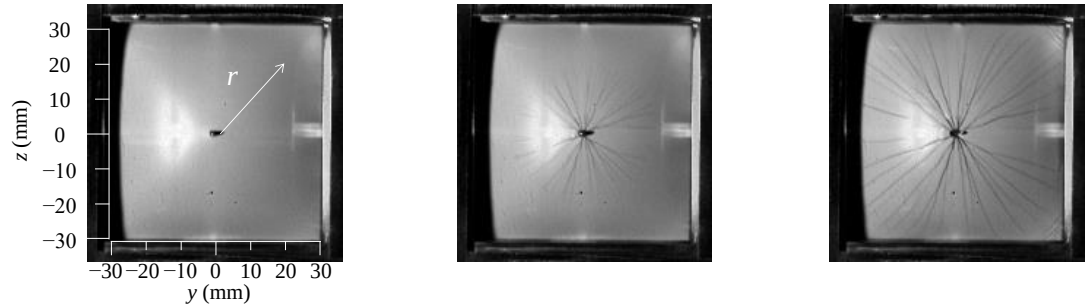


$t$ = 0 μs $t$ = 20 μs $t$ = 40 μs

(a)

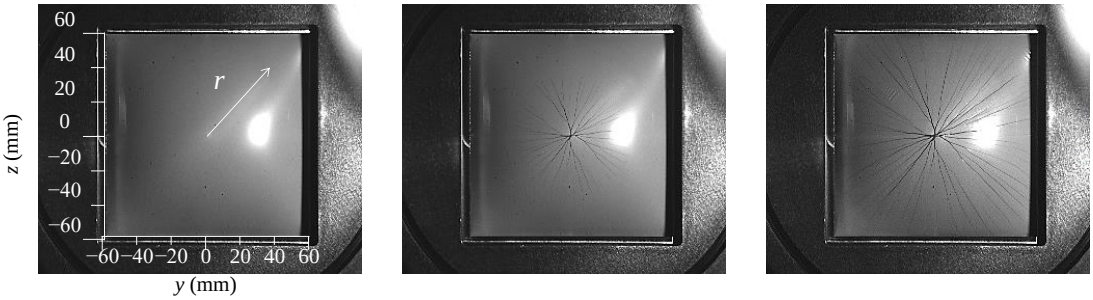


$t$ = 0 μs $t$ = 40 μs $t$ = 80 μs

(b)

Figure 2.2 Crack propagation behaviors. (a) $D$ = 62 mm, $\varphi$ = 35.0%RH, $p_4$ = 140.9 kPa, and $p_1$ = 100.9 kPa and (b) $D$ = 120 mm, $\varphi$ = 41.5%RH, $p_4$ = 121.5 kPa, and $p_1$ = 101.5 kPa.

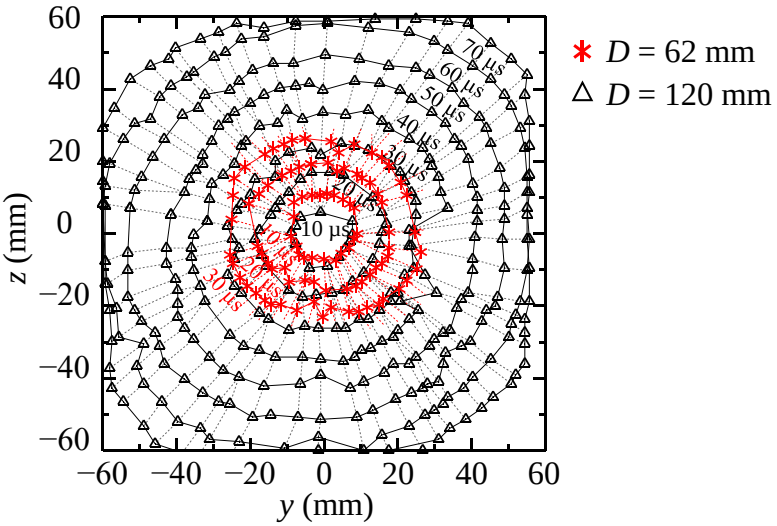


Figure 2.3 Extracted crack head positions.

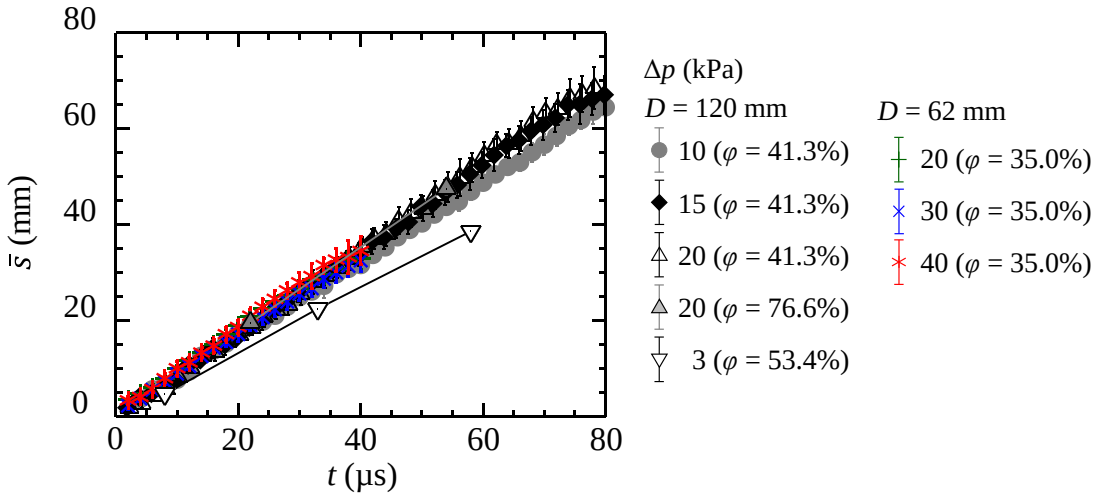


Figure 2.4 Time evolution of the averaged crack length.

### 2.3.3 Petal formation law

Figure 2.5 shows examples of the opening process of the cellophane diaphragm visualized using Setup II. The temperature in the driven section ranged from 289.6 to 295.0 K. The humidity, $\varphi$, in the driven section was different in all experiments, within 20.0%RH $\leq \varphi \leq$ 76.6%RH. The humidity affected the initial deformation of the diaphragm, which changed the initial tensile stress acting on the diaphragm, $\sigma_i$. The calculated values of $\sigma_i$ were within 0 MPa $\leq \sigma_i \leq$ 68.7 MPa. A small tensile stress ($\sigma_i \leq$ 10.3 MPa) was obtained under the following pressure setting: first applying $p_4 = p_1 + 20.0$ kPa and subsequently decreasing it to $p_4 \leq p_1 + 3.0$ kPa. The diaphragm was ruptured at $p_4 = 0$, 1, and 3 kPa. Because the diaphragm underwent a partial plastic deformation owing to the pressure difference, we obtained a small $\Delta p_{41}$ and $R$ using Eq. (2.2) following the aforementioned procedure and examined the small tensile stress condition. The time, $t$, was synchronized by comparing the images of the first crack appearance to the images captured every 2 μs in the previous experiment (Fig. 2.2). As shown in Fig. 2.5, two types of crack propagation regimes are observed. When $\sigma_i$ = 3.45 and 20.0 MPa, a single crack was generated, and a crack branch was not observed. Moreover, in the lowest tensile stress case ($\sigma_i$ = 3.45 MPa), the crack propagation stopped before reaching the duct wall. This partial diaphragm opening regime is unfavorable for shock wave formation. Alternatively, in the higher tensile stress cases ($\sigma_i \geq$ 25.9 MPa), petal-like fragments were formed by crack propagation with a branch from the center of the diaphragm, and they began rotating about the axis-of-rotation on the wall. The number of petals varied with $\sigma_i$. Under a high tension, $\sigma_i$ = 68.7 MPa, numerous petals were formed (146 petals), and the apex angle of the petals became extremely small. On the contrary, a smaller tensile stress resulted in a fewer number of petals. The number of petals was 9 when $\sigma_i$ = 25.9 MPa. Notably, the

aforementioned two types of crack propagation regimes were observed in a previous study on a highly elastomeric material (Moulinet and Adda-Bedia, 2013). However, in this study, these crack propagation regimes emerged for a highly brittle material.

Figure 2.6 shows the variation in the number of crack fronts, $N$, with respect to the coordinate, $r$, obtained from the images. For clear detectability of the petal tips, the images in the range of 100 μs < $t$ < 200 μs were used for $D$ = 120 mm. The detected branch position (petal tip position) was different from the initial branch point by approximately 3 mm maximum. This was because the central area started to rotate earlier than the marginal area. For $D$ = 62 mm, the post-mortem cellophane diaphragm after the experiment was used in the analysis. With increasing $r$, $N$ increased almost linearly. This trend indicated that the crack growth maintained a certain constant difference from neighboring cracks. When $r$ exceeded $D$/4 (30 and 15.5 mm for $D$ = 120 and 62 mm, respectively), the rate of increase in $N$ decreased compared with that for $r < D/4$.

In the following, the number of cracks formed is discussed. We examined the number of crack fronts equidistant from the origin that were induced by needle impingement using $N/2\pi r$ m$^{-1}$. For counting the number of cracks, the region of $r \leq D/4$ was used, in which $N$ linearly increased with $r$ (as shown in Fig. 2.6). In this region, boundary reflections were irrelevant according to the abovementioned estimated longitudinal and shear wave speeds. Fig. 2.7 shows a plot of $N/2\pi r$ as a function of the initial diaphragm tensile stress $\sigma_i$. The maximum value of $N/2\pi r$ was 531 m$^{-1}$ when $\sigma_i$ = 68.7 MPa. If we assume that the cracks were generated equidistantly, each crack grew keeping a constant distance of 1.88 mm from the neighboring cracks. On the contrary, the smallest value was 47.7 m$^{-1}$ when $\sigma_i$ = 25.9 MPa, and the distance between cracks was estimated as 20.9 mm. Under the conditions wherein crack branch events were observed ($\sigma_i \geq$ 25.9 MPa), the relation

between $N/2\pi r$ and $\sigma_i$ were fitted using a linear function as follows:

$$N/2\pi r = \chi(\sigma_i - \sigma_c), \tag{2.3}$$

where $\chi$ and $\sigma_c$ are fit to constants of $1.20 \times 10^{-5}$ $Pa^{-1}m^{-1}$ and 23.7 MPa, respectively. The determination coefficient is 0.859. $\sigma_c = 23.7$ MPa can be considered as the threshold stress of the crack branch in the cellophane diaphragm. This petal-formation law was derived from the experimental results with different device scales $D$ and humidity $\varphi$. Therefore, the petal-formation law in Eq. (2.3) is a single function of $\sigma_i$, i.e., the distance between cracks can be quantitatively estimated by $\sigma_i$. Thus, this law enables predicting the fragmentation behavior of the cellophane diaphragm in application scenarios. Alternatively, when $\sigma_i$ was smaller than $\sigma_c$, the cracks exhibited a different behavior from that in the high-stress case. In a magnified plot of Fig. 2.7, the behavior of $N/2\pi r$ under a low stress can be observed. When $\sigma_i \leq 20.6$ MPa, crack branch events could not be observed ($N = 2$). Under the condition of lower $\sigma_i$, the single crack did not reach the shock tube wall. When $\sigma_i = 3.71$ MPa, the right-side tip of the single crack stopped at $r < D/4$, and $N = 1$. When the tensile stress was zero, the needle simply penetrated the diaphragm without causing crack propagation ($N = 0$). The present experiments clarified that $N/2\pi r$ was significantly influenced by $\sigma_i$. When $\sigma_i$ was higher than a certain minimum value (25.9 MPa in the experiments), crack branching events occurred, and $N/2\pi r$ followed Eq. (2.2). When $\sigma_i$ was smaller than a certain maximum value (20.6 MPa in the experiments), a single crack was generated, and the diaphragm opening was partial. Moreover, when $\sigma_i$ was smaller than 3.71 MPa, the crack propagation stopped prior to the wall. These results suggested that $\sigma_i$ should be set higher than $\sigma_c = 23.7$ MPa to obtain multiple petal formation and subsequently achieve full diaphragm opening during the shock tube operation.

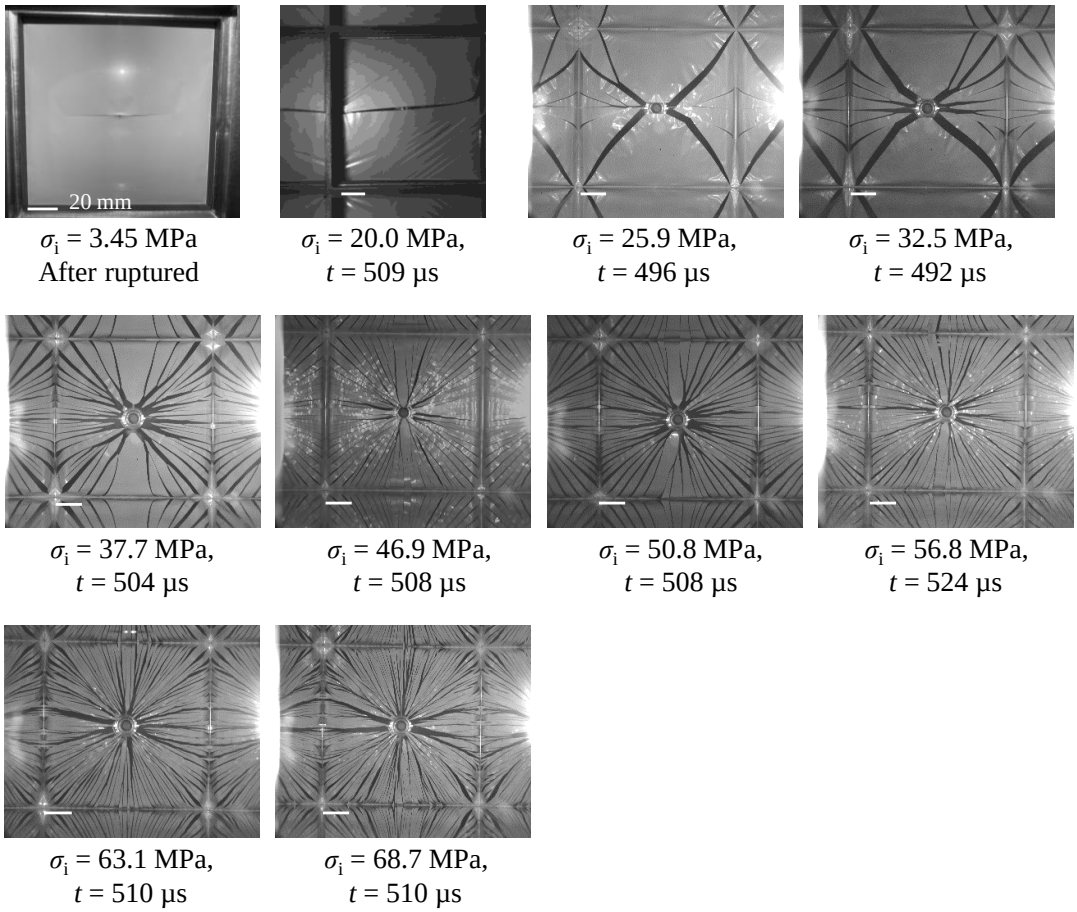


Figure 2.5 Examples of the ruptured diaphragm morphologies under different humidity values at different $\sigma_i$ obtained using Setup II. The brightness and the contrast are adjusted for visibility.

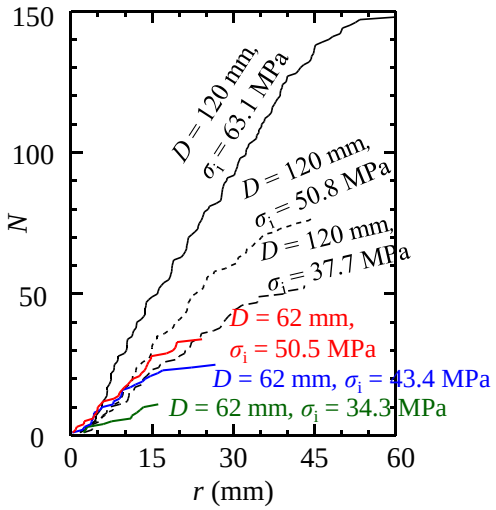


Figure 2.6 Number of cracks $N$ as a function of $r$.

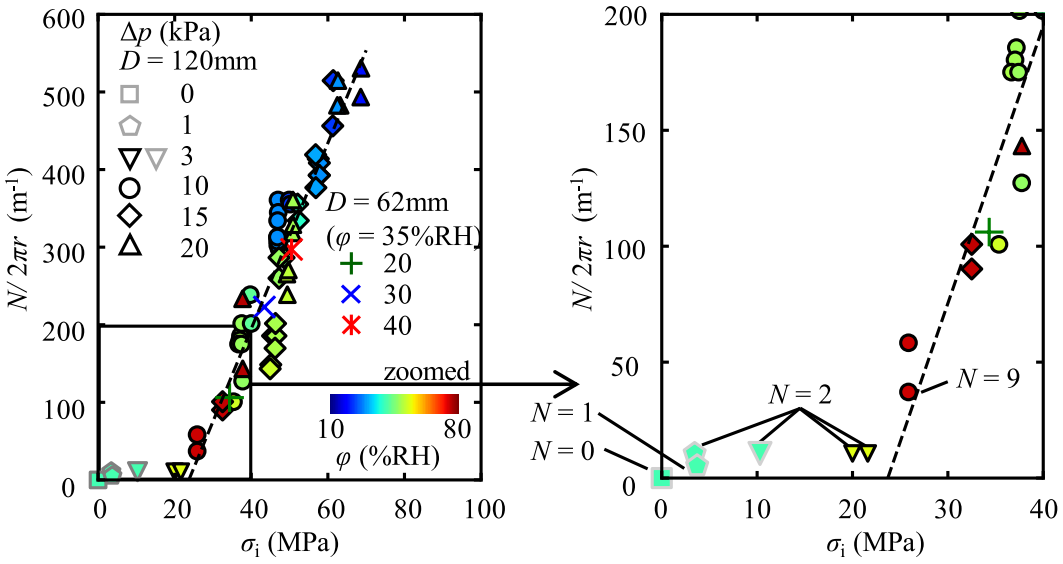


Figure 2.7 $N/2\pi r$ versus $\sigma_i$, where the dashed line represents the linear fitting results for all the cases wherein crack branch events are observed. The data points for $\sigma_i \leq 10.3$ MPa (with gray plot frames) correspond to the experimental condition wherein $p_4 = p_1 + 20.0$ kPa and is subsequently decreased to $p_4 \leq p_1 + 3.0$ kPa. The line colors in Fig. 2.6 and 2.7 for $D = 62$ mm are the same.

### 2.3.4 Opening dynamics of cellophane diaphragm

In this section, the opening process of the fragmented petals of the diagram is discussed. In this part of the study, the stress acting on the diaphragm ($\sigma_i > \sigma_c = 23.7$ MPa) in the shock tube with $D = 62$ mm was used. The humidity in the side of the low-pressure section was fixed at approximately 35%RH. Figure 2.8 shows sequence images of the diaphragm opening motion. Figures 2.8 (a)–(c) correspond to trials with different initial pressures of the driver and driven sections. The cellophane diaphragm is shown by a dashed enclosed black line in each image on the top-left corner. With the opening of the diaphragm, the needle and its sting installed in the driver section appeared in the gaps of the petals. They could be easily recognized owing to the glare from the illumination reflection. Taking Fig. 2.8 (c) as an example, the entire diaphragm opening process is described. At $t$ = 6 μs, crack propagation occurred. This was the initial state of the diaphragm opening, as discussed in the previous section. The compression waves generated from the torn area by the crack were propagated into the driven section. At $t$ = 166 μs, clustered triangular petals were formed by a straight crack propagation from the center to the wall. Some petals were small because of the crack branching in the propagation process. From $t$ = 166 to 806 μs, the area between the petals increased because the petals inclined toward the driven section. At $t$ = 806 μs, the diaphragm opening was nearly complete. The petals remained on the wall, and some of them were deformed. This sequence of events is also qualitatively confirmed from Fig. 2.8 (a) and (b).

The time variations of the projective diaphragm opening area ratio, $\alpha$, are shown in Fig. 2.9. The opening area ratio is defined as the ratio of the projective opening area to the cross-section area of the shock tube. $\alpha$ increased steeply from $t$ = 0 to 40 μs. This

period corresponded to the initial crack propagation process from the stimulated point to the shock tube wall. To distinguish between the opening due to the petal motion, the opening area ratio associated with the cracks is defined as $\Delta\alpha$. $\Delta\alpha$ was calculated using the visualization image captured immediately after the crack propagation. The values of $\Delta\alpha$ were 0.05, 0.085, and 0.11 for $p_4 - p_1 = 20$, 30, and 40 kPa, respectively. Reasonably, the $\Delta\alpha$ value was approximately proportional to the number of cracks, and it continuously increased after the crack propagation was completed ($t \sim 40$ μs). With time elapse, the time variations of $\alpha$ showed inflection points and subsequently achieved constant values smaller than 1. The values of $\alpha$ did not reach 1 because the petals remained at the wall after the opening process. The opening time of the diaphragm shortened with the increase in the initial pressure difference.

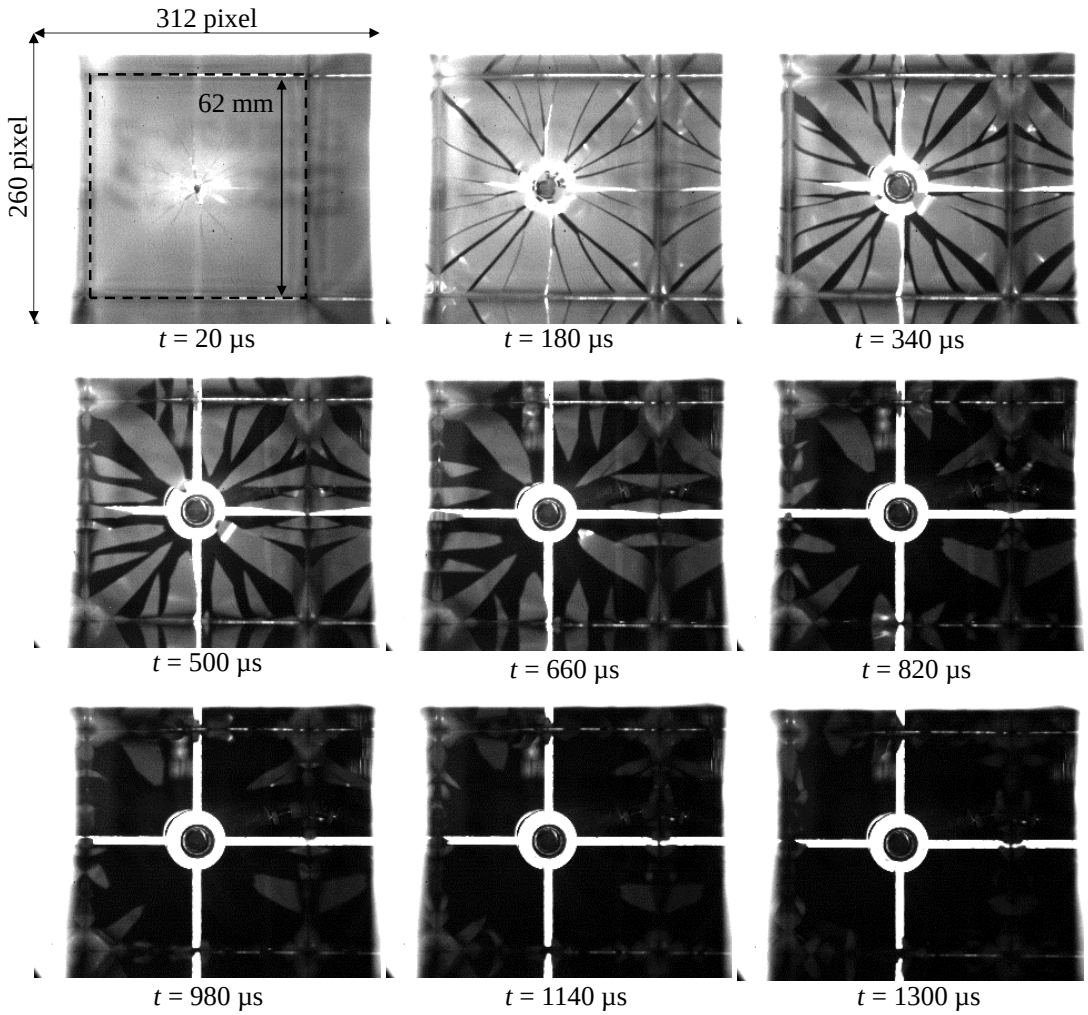


Figure 2.8 Examples of the visualized petal opening processes: (a) $p_4$ = 120.6 kPa, $p_1$ = 100.6 kPa, (b) $p_4$ = 129.9 kPa, $p_1$ = 99.9 kPa, and (c) $p_4$ = 140.6 kPa, $p_1$ = 100.6 kPa.

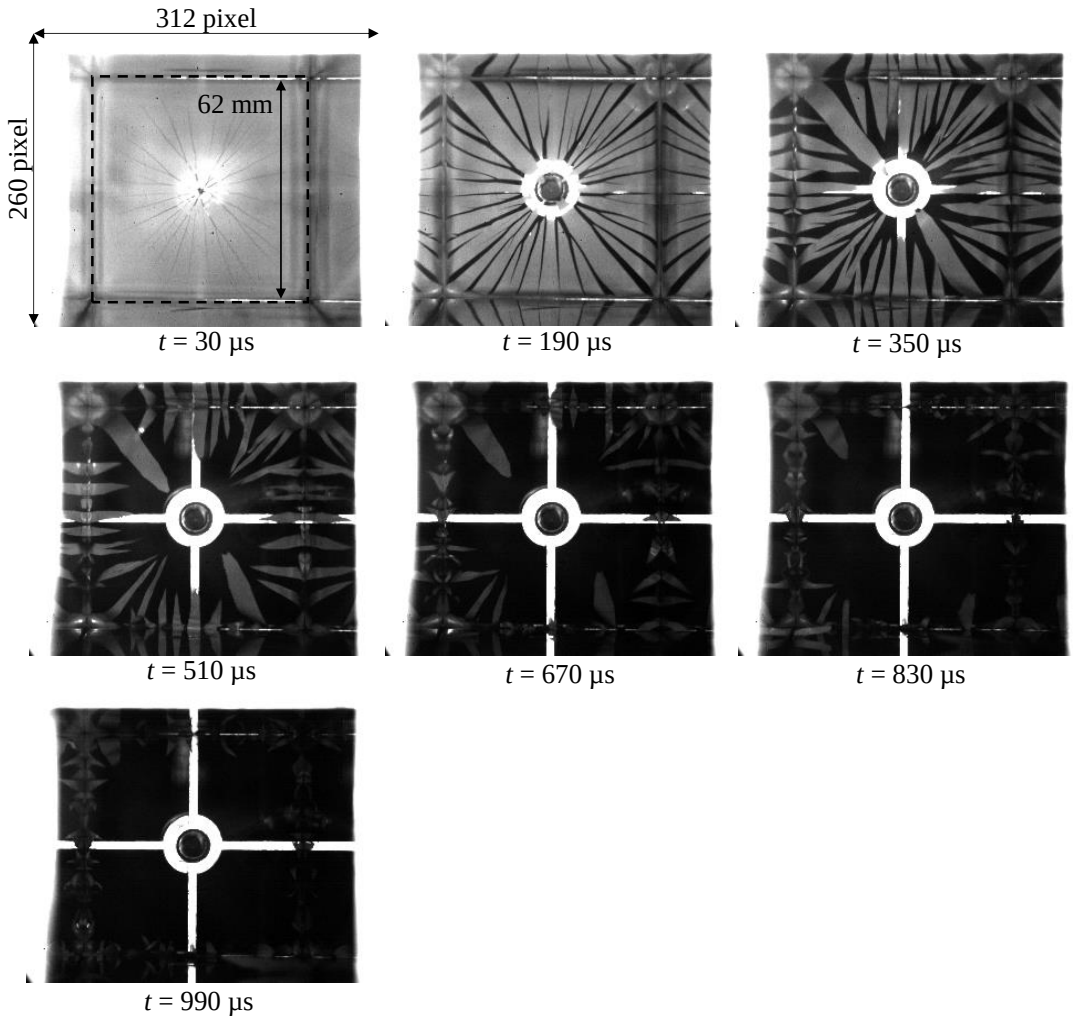


**(b)**

Figure 2.8 (Continued)

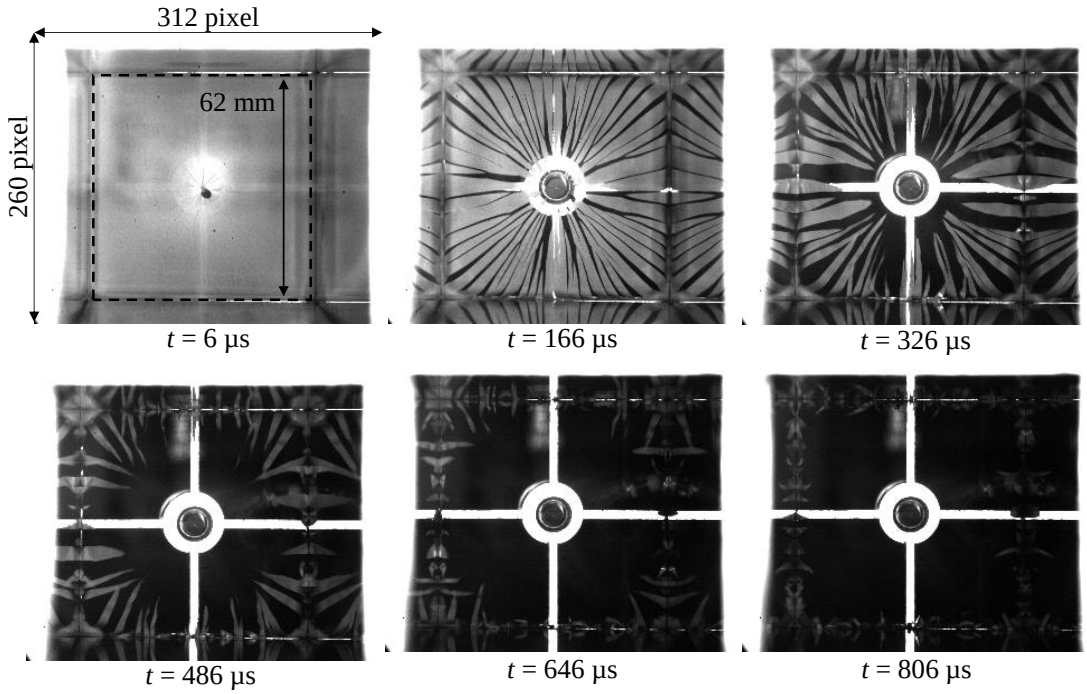


Figure 2.8 (Continued)

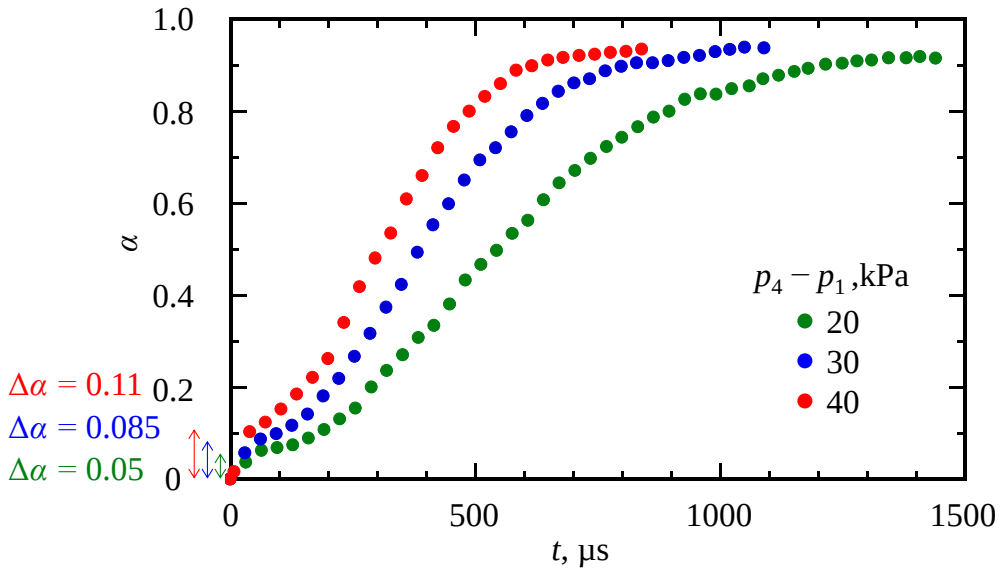


Figure 2.9 Time variations of the projected opening area ratio.

To understand the cellophane diaphragm opening processes, the opening motion of the petals was modeled by the equation of the rotational motion around the shock tube wall. This developed model is called the "rotational motion model" in this study. To establish this model, we needed to simplify the diaphragm opening motion. The following assumptions were made:

(1) The opening by the cracks was offset as $\alpha = \Delta\alpha$ at $t = 0$ because the rotational motion model could not express the diaphragm opening due to the cracks correctly.

(2) At $t = 0$, the diaphragm was equally and instantaneously divided into triangular petals with the wall as their base. Thus, the base length was $4D/N$, where $N$ is the number of cracks.

(3) The petals exhibited a rigid-body rotational motion with the wall as the axis of rotation.

(4) The diaphragm before rupture did not bulge under the initial pressure difference.

(5) The pressure difference driving the rotational motion of the petals was the initial pressure difference that was sustained when $t \leq \tau$ and became zero after $t = \tau$. Here, $\tau$ is the effective opening force period by the pressure difference.

(6) The petals presented an equiangular acceleration motion at the effective opening force period, $\tau$, and subsequently a constant-angular velocity motion by inertia.

(7) The frictional resistance of the rotating shaft was negligible.

From the above assumptions, the area of a petal ($A$), moment of inertia $I$, pressure difference $\Delta p_p$ acting on the petals, and equation of the rotational motion are respectively expressed as follows:

$$A = \frac{1}{2} \cdot \frac{4D}{N} \cdot \frac{D}{2} = \frac{D^2}{N} \tag{2.4}$$

$$I = Ae\rho_c\left(\frac{D^2}{24} + \frac{e^2}{12}\right) \tag{2.5}$$

$$\Delta p_p = \begin{cases} \Delta p_{41} & (0 \le t \le \tau) \\ 0 & (\tau < t) \end{cases} \tag{2.6}$$

$$I\,\ddot{\theta}(t) = \frac{\Delta p_p AD}{6} \tag{2.7}$$

Equation (2.7) can be analytically solved using Eqs. (2.4)–(2.6). The different solutions during and after $\tau$ are

$$\theta(t) = \begin{cases} \dfrac{\Delta p_{41} D \cdot t^2}{12e\rho_c\left(\dfrac{D^2}{24} + \dfrac{e^2}{12}\right)} & (0 \le t \le \tau) \\ \dot{\theta}(\tau)(t-\tau) + \theta(\tau) & (\tau < t) \end{cases} \tag{2.8}$$

In Eq. (2.8), the inclination of the petals, $\theta$, is expressed by $D$, which is dependent on the size of the shock tube, thickness of the diaphragm $e$, and density of the cellophane diaphragm $\rho_c$, which is determined by the diaphragm characteristics. The entire projected opening area ratio, $\alpha$, is expressed as a function of $\theta$ as follows:

$$\alpha(t) = 1 - \cos[\theta(t)] + \Delta\alpha \tag{2.9}$$

The value of $\tau$ in Eq. (2.8) is required to solve Eq. (2.9). To estimate $\tau$, the pressure states of both sides of the petals were considered by the development of the domain of influence of the characteristic waves generated by crack propagation. A schematic of the sequence of the development of the domain of influence is shown in Fig. 2.10. As shown in Fig. 2.10 (a), an isosceles triangular petal with a base length of $4D/N$, height of $D/2$, and perimeter that is the shock wave cross-section divided by $N$ is a representative of the petal shape. The average number of petals experimentally observed was used in this analysis: $N$ = 16.3, 25.5, 44.1, and 63.3 for $p_4 - p_1$ = 10, 20, 30, and 40 kPa, respectively. Figure 2.10 (b) shows the state in which the cracks propagate from the top to the shock tube wall. From the crack speed measurements shown in Fig. 2.4, we assume that the

crack speed is constant regardless of the initial pressure difference. Because the crack propagation speed, $v_c$, is higher than the speed of sound of the test gas, the head of the domain of influence forms a Mach angle $\psi$ of 25.3° with the leading edge of a crack as the top. The state presented in Fig. 2.10 (c) corresponds to the time of the completion of the crack propagation (this time is defined as $t = t_1$). The shortest distance between the center of the petal base and the head of the domain of influence is defined as $l$. $\varepsilon$ is the base angle of a diaphragm petal. After the completion of the crack propagation, the domain of influence spreads at the speed of sound, as shown in Fig. 2.10 (d). When the Mach wave reaches the petal base center, the domain of influence covers the entire petal (Fig. 2.10 (e)). This time is defined as $t = t_2$, which is taken as the $\tau$ estimated from the analysis. From the geometrical relationships, $t_1$, $l$, and $t_2$ are expressed as follows:

$$t_1 = \frac{D\sqrt{\frac{1}{4} + \frac{4}{N^2}}}{v_c} \tag{2.10}$$

$$l = \frac{2D}{N}\sin(\varepsilon - \psi) = \frac{2D}{N}\sin\left\{\arctan\left(\frac{N}{4}\right) - \arcsin\left(\frac{a_1}{v_c}\right)\right\} \tag{2.11}$$

$$t_2 = t_1 + \frac{l}{a_1} \tag{2.12}$$

$t_1$ and $t_2$ depend only on the number of cracks, $N$, because $v_c$ is constant. $t_1$ is a decreasing function of $N$, and $s$ and $t_2$ are decreasing functions of $N > 5$. The values of $t_2$ are 57, 51, 46, and 43 μs for $\Delta p_{41}$ = 10, 20, 30, and 40 kPa, respectively. Because $N$ increases with the increase in $\Delta p_{41}$ and the petals become smaller, $t_2$ is a decreasing function of $\Delta p_{41}$.

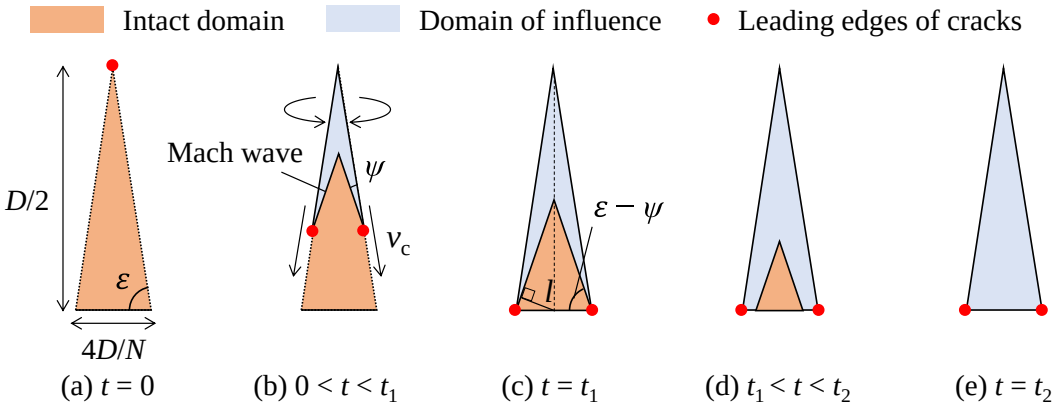


Figure 2.10 Schematic of the estimation model of the propagation of the domain of influence on the diaphragm petal at $p_4$ = 120.6 kPa and $p_1$ = 100.6 kPa: (a) a representative of the petal shape, (b) the state when the cracks propagate from the top to the shock tube wall, (c) the state at the time of the completion of the crack propagation ($t = t_1$), (d) the state after the completion of the crack propagation with spreading of the domain of influence, and (e) the state when the domain of influence covers the entire petal.

The time variations of $\alpha$ calculated using the rotational motion model (Eqs. (2.8) and (2.9)) and obtained from the experiments are shown in Fig. 2.11. The solid lines show the results of the best fit when varying $\tau$ among integers in the model. $\tau$ used for the best fit is denoted as $\tau_e$, and $\tau_e$ = 49, 42, and 39 μs for $\Delta p_{41}$ of 20, 30, and 40 kPa, respectively. For the dashed line case, the estimated $t_2$ from the analysis of the development of the domain of influence is employed as the $\tau$ in the rotational motion model. In the experimental results, the time variation of $\alpha$ shows an inflection point and a constant value of smaller than 1. In contrast, using the rotational motion model, the time variation of $\alpha$ does show an inflection point, and its slope continuously increases. This is because the effects of the drag by the gas and the deformation of the petals are ignored in the model. For the initial pressures of $p_4$ = 140.6 kPa and $p$ = 100.6 kPa, the best fit ($\tau = \tau_e$ = 39 μs) when varying $\tau$ reproduces well the experimental results in the range of $\Delta\alpha < \alpha < 0.48$ (40 μs < $t$ < 296 μs). Therefore, it reflects the initial state of the actual diaphragm opening well. Moreover, as a result of using $t_2$ = 43 μs as $\tau$, the model can reflect the experimental results in the initial stage of $\Delta\alpha < \alpha < 0.2$ (40 μs < $t$ < 136 μs). For each initial pressure difference, as shown in Fig. 2.11, similar relations are confirmed between the experimental and rotational motion model findings. The best fit of the rotational motion model results reproduces the initial diaphragm opening process well. As the pressure difference decreases, the results from the rotational motion model fit a larger value of $\alpha$.

In Fig. 2.12, $t_1$, $t_2$, and $\tau_e$ for each initial pressure condition are plotted. The values of $t_1$ are similar under all conditions. Because $N$ increases with the increase in the initial pressure difference, $t_2$ decreases. The time used in the best fit, $\tau_e$, obtained from the best fit of the experimental results also becomes a decreasing function with the increasing initial pressure difference. Under all conditions, $t_2$ is greater than $\tau_e$. This is because of the

overestimation of the effective time, $\tau$, caused by its definition as the time for the domain of influence to cover the entire petal surface. However, the difference between $\tau_e$ and $t_2$ is small considering the complexity of the actual morphology of the cellophane diaphragm. In the following, we discuss in the detail the petal opening motion in the initial stage. Using the developed rotational motion model, we evaluated the petal angular velocity, $\omega$, and the area-averaged petal velocity, $\overline{v_p}$, at $t = t_2$. Table 2.1 summarizes the petal motion at $t = t_2$ and compares $\overline{v_p}(t = t_2)$ and the contact surface velocity, $u_c$, calculated using the Rankine–Hugoniot relation applied under the shock tube operation conditions of $p_4$ and $p_1$. As seen $\theta(t = t_2)$ in Table 2.1, the initial pressure difference in the angular acceleration process of the petals only occurs in the initial period when the petals hardly incline. Specifically, the largest petal inclination, $\theta(t = t_2)$ is 4.6° when $p_4$ = 140.6 kPa and $p_1$ = 100.6 kPa. Moreover, at $t = t_2$, the area-averaged petal velocity, $\overline{v_p}$, is similar to the contact surface velocity, $u_c$, even at the early stage of the diaphragm opening ($t_2$ is estimated as 40 μs < $t_2$ < 60 μs, as shown in Fig. 2.12). After this matching, the diaphragm does not impede the shock tube flow. This is significantly effective for shock wave formation.

From the above discussion, if the number of petals and the crack propagation speed are known, the initial process of the petal opening motion can be modeled as an equiangular acceleration rotational motion when $t \leq \tau$. The initial pressure difference duration, $\tau$, can be estimated using the developed simplified model considering the propagation of the domain of influence by the characteristic waves on the petals. Moreover, the petal opening motion is determined at the initial stage mainly by the morphology of the crack propagation. As discussed in a subsequent section, these characteristics of the motion of petals are very important because the shock wave

formation distance is determined by the initial opening process of the diaphragm.

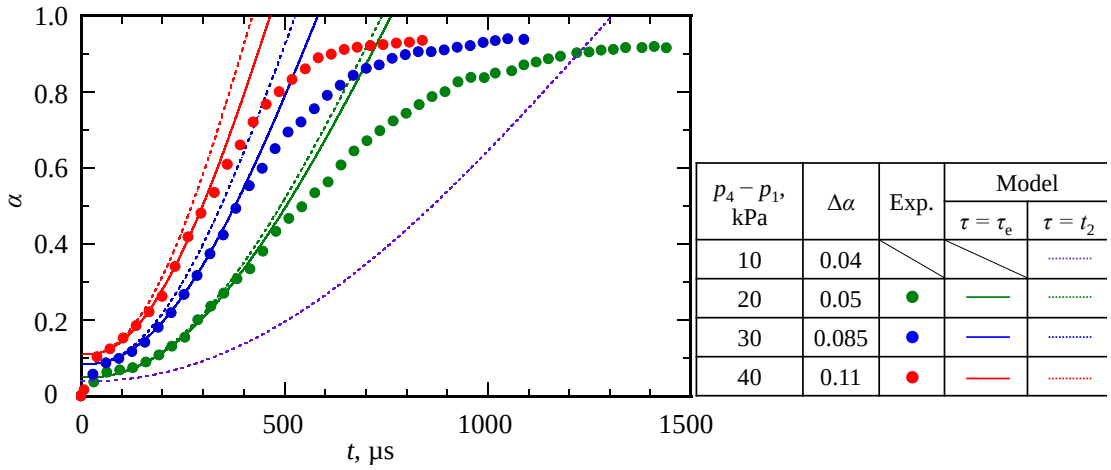


| $p_4 - p_1$, kPa | $\Delta\alpha$ | Exp. | Model | |
|---|---|---|---|---|
| | | | $\tau = \tau_e$ | $\tau = t_2$ |
| 10 | 0.04 | | | |
| 20 | 0.05 | ● | — | ····· |
| 30 | 0.085 | ● | — | ····· |
| 40 | 0.11 | ● | — | ····· |

Figure 2.11 Time variations of the projected opening area ratio from the experiments and the models. The solid lines show the results of the best fits when various integer values of $\tau = \tau_e$ are used in the rotational motion model. The dashed lines show the results using estimated $t_2$ for $\tau$, calculated from the analysis shown in Fig. 2.10.

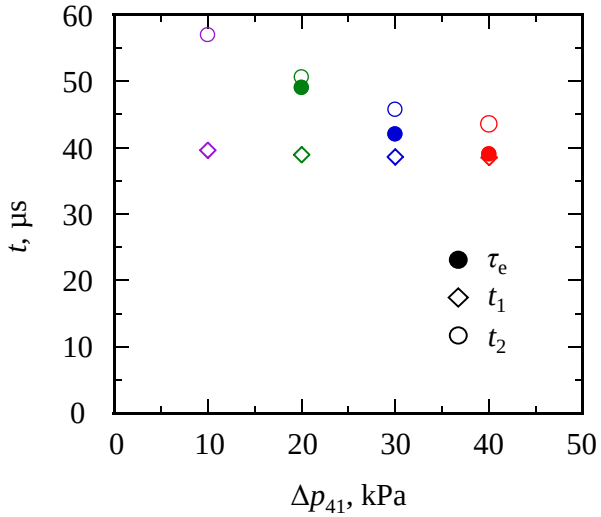


Figure 2.12 Plots of the characteristic times as functions of $\Delta p_{41}$. $\tau_e$ is the effective opening force period used in the best fitting, $t_1$ is the time of crack propagation completion, and $t_2$ is the time when the domain of influence covers the entire petal surface.

Table 2.1 Petal states at the beginning of the inertial motion ($t = t_2$). The inclination angle of a diaphragm petal is $\theta$, angular velocity of a diaphragm petal is $\omega$, area-averaged petal velocity during the inertial motion is $\overline{v}_p$, and contact surface velocity is $u_c$. $u_c$ is calculated from initial pressures $p_4$ and $p_1$.

| $(p_4, p_1)$, kPa | $\theta(t = t_2)$, ° | $\omega(t = t_2)$, rad/s | $\overline{v}_p(t = t_2)$, m/s | $u_c$, m/s |
|---|---|---|---|---|
| (110.6, 100.6) | 1.9 | 1198 | 12.3 | 11.7 |
| (120.6, 100.6) | 3.1 | 2127 | 22.0 | 22.4 |
| (129.9, 99.9) | 4.0 | 2951 | 30.5 | 32.4 |
| (140.6, 100.6) | 4.6 | 3657 | 37.8 | 41.3 |

## 2.4 Effect of cellophane diaphragm rupture on shock wave formation

In this section, the relation between the diaphragm opening processes and the shock wave formation is presented. To obtain the pressure histories, the shock tube was operated using Setup III (Fig. 2.1 (c)). The overpressure, $\Delta p$, was measured on the shock tube wall using the flush-mounted pressure transducers. The same diaphragm employed in the above experiments was used.

Figure 2.13 (a) and (b) shows the $\Delta p$ waveforms measured at $x/D$ = 2.26 and 22.4, which are the pressure measurement points closest to and farthest from the diaphragm, respectively. The initial pressure conditions were $p_4$ = 110.6 kPa and $p_1$ = 100.6 kPa. Even at $x/D$ = 22.4, the coalescence of the compression waves to form a shock wave was incomplete, and the pressure behind the shock wave continued to increase. Hence, a fully planar shock wave was not generated even at the farthest measuring point in the present experimental setup when $\Delta p_{41}$ was 10 kPa.

Figure 2.14 shows the overpressure waveform under stronger initial conditions than for those in Fig. 2.13, i.e., $p_4$ = 140.6 kPa and $p_1$ = 100.6 kPa. At $x/D$ = 2.26 (Fig. 2.14 (a)), a tendency of increasing overpressure similar to that in Fig. 2.13 (a) is observed. Relatively strong pressure fluctuations are observed in the period of approximately 80–150 μs after passing through the leading shock wave. In contrast, at $x/D$ = 22.4 (Fig. 2.14 (b)), a single steep pressure increase is seen, and a gradual multistage pressure increase is not noted. The flush-mounted pressure transducers on the shock tube wall had diameter of 5.5 mm each. Approximately 16 μs are needed to pass the transducer at the speed of sound. The time of the pressure increase due to the passing of the shock wave, as shown

in Fig. 2.14 (b), is similar at this level. Considering the time resolution of these measurements, it can be inferred that the compression waves transit to the single shock wave. The pressure disturbances due to the transverse waves are also attenuated.

To evaluate the coalescence of the compression waves, understanding the states of the characteristic waves is necessary. As an example, the results shown in Fig. 2.14 ($p_4$ = 140.6 kPa and $p_1$ = 100.6 kPa) are taken. The speeds of the characteristic waves, $c_+$, at characteristic points (i)–(iv), which are shown in Fig. 2.14 (a), were calculated using the pressure history. Point (i) is the time when the head of the compression wave reaches the measuring point. Point (ii) is the time when the slope of the pressure increase becomes steep. Point (iii) is the end of the steep pressure increase. Point (iv) is the time when the average overpressure is first reached after the pressure increase. Although, multidimensional disturbances are observed in the overpressure history at $x/D$ = 2.26 (Fig. 2.14 (a)), one-dimensional shock wave formation can be discussed based on the them using the averaged overpressure at point (iv). The shock formation distance can be estimated by analyzing the propagation of the compression waves at points (i)–(iv). The speeds of the characteristic waves, $c_+$, at points (i)–(iv) are expressed as follows (Sasoh, 2020):

$$c_+ = \left[ \frac{\gamma + 1}{2} \left( \frac{p_1 + \Delta p}{p_1} \right)^{\frac{\gamma - 1}{2\gamma}} - 1 \right] \frac{2}{\gamma - 1} a_1. \tag{2.13}$$

A diagram of the characteristic waves is shown in Fig. 2.15. The time variations of the projection opening ratio from the experiments and the best fit of the rotational motion model results (which are the same results as in Fig. 2.11) are shown in Fig. 2.15 (a). Under the considered condition, the compression waves at points (i)–(iii) coalesce at $x/D$ = 3.87. In the measured pressure history at $x/D$ = 4.27, the gradual pressure increase between

points (i) and (ii) at $x/D$ = 2.26 is not observed. The compression waves at points (iii) and (iv) coalesce at $x/D$ = 27.1. Considering that the characteristic velocity behind the shock wave is higher than the shock wave propagation velocity, all compression waves coalesce into the leading shock wave at $x/D$ = 27.1 and form a single shock wave, which is consistent with the experimental results at $x/D$ = 22.4 (Fig. 2.14 (b)). Thus, we can confirm the reasonability of this analysis.

To consider the relationship between the compression wave integration and the diaphragm opening time, the speed of the characteristic waves obtained at $x/D$ = 2.26 is extrapolated to $x$ = 0, which is the point of the diaphragm installation. The time at which the compression waves are generated at $x$ = 0 can be estimated and compared as the diaphragm opening time obtained in the previous experiments. Let the time at which the compression waves generate corresponding to point (i) in Fig. 2.14 (a) at $x$ = 0 be $t$ = 0, which corresponds to the beginning of the diaphragm opening process. The time of the compression wave generation corresponding to point (ii) at $x$ = 0 is $t$ = 38.2 μs. From Fig. 2.12, this time is approximately the time, $t_1$, when the crack propagation is completed. Therefore, we can conclude that the pressure increase between points (i) and (ii) measured at $x/D$ = 2.26 is due to the compression waves leaking from the cracks to the low-pressure chamber during the crack propagation. The time of the compression wave generation at point (iii) is $t$ = 78.2 μs. Although the pressure at $x/D$ = 2.26 reaches approximately 90% average overpressure owing to these compression waves, these waves are generated at the beginning of the opening process, which is approximately twice the completion time of the crack propagation. Furthermore, the time of the compression wave generation at point (iv) at $x$ = 0, which finally forms a single shock wave, is $t$ = 118 μs. As shown in Fig. 2.15 (a), $t$ = 118 μs is approximately one-fifth of the diaphragm opening time. At this

time, the projected opening ratio of the diaphragm does not reach $\alpha$ = 0.2, and the diaphragm is still in the middle of its opening process. Considering that the compression waves generated after this time do not affect the shock wave formation, the entire opening process of the cellophane diaphragm does not play an effective role in the shock wave formation. Therefore, the initial opening process corresponding to the period of approximately twice–thrice the completion time of the crack propagation is suggested to play a dominant and significant role. The matching process between the petal velocity and the contact surface, as discussed in Section 2.3.4, seems to contribute to this result. Compression waves are unexpected to generate after this matching process. The same tendencies are also confirmed for $p_4 - p_1$ = 20 and 30 kPa.

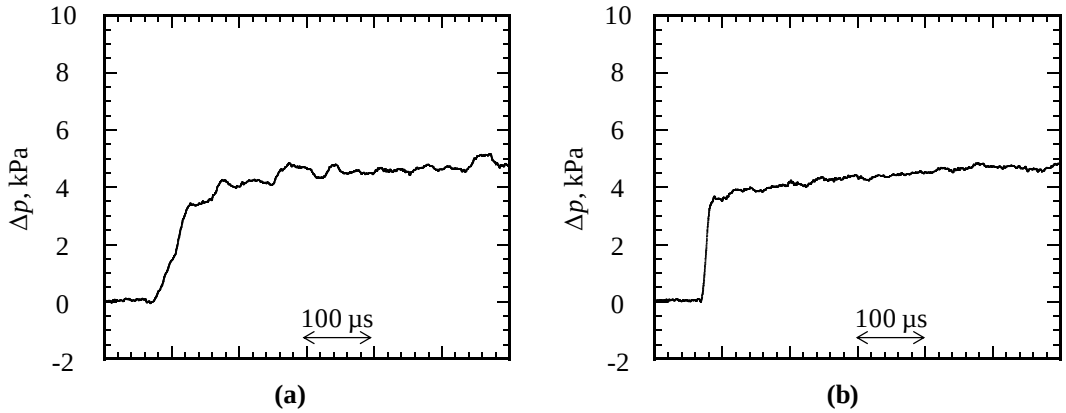


Figure 2.13 Overpressure histories at $p_4$ = 110.6 kPa and $p_1$ = 100.6 kPa. (a) $x/D$ = 2.26 and (b) $x/D$ = 22.4. Under these conditions, a fully planar shock wave is not formed because the shock formation distance is longer than the used driven section length.

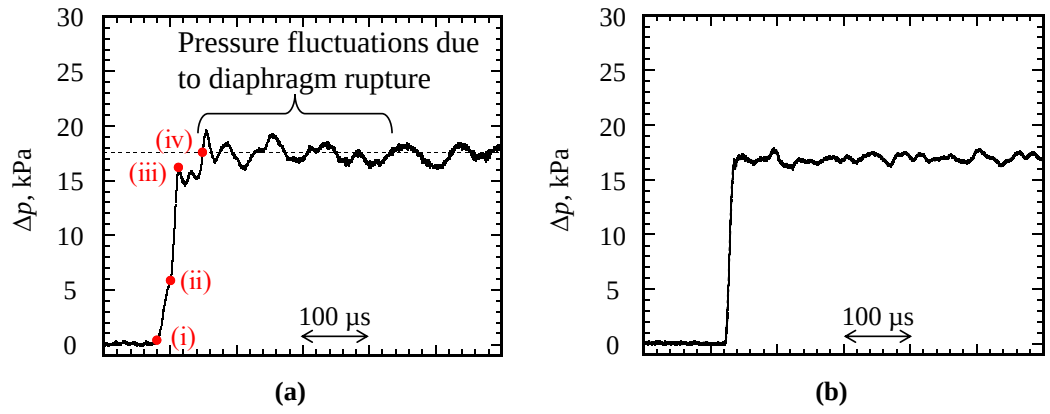


Figure 2.14 Overpressure histories at $p_4$ = 140.6 kPa and $p_1$ = 100.6 kPa. (a) $x/D$ = 2.26 and (b) $x/D$ = 22.4. Red points (i)–(iv) correspond to the characteristic set of time and overpressure used in the analysis of the coalescence of the compression waves.

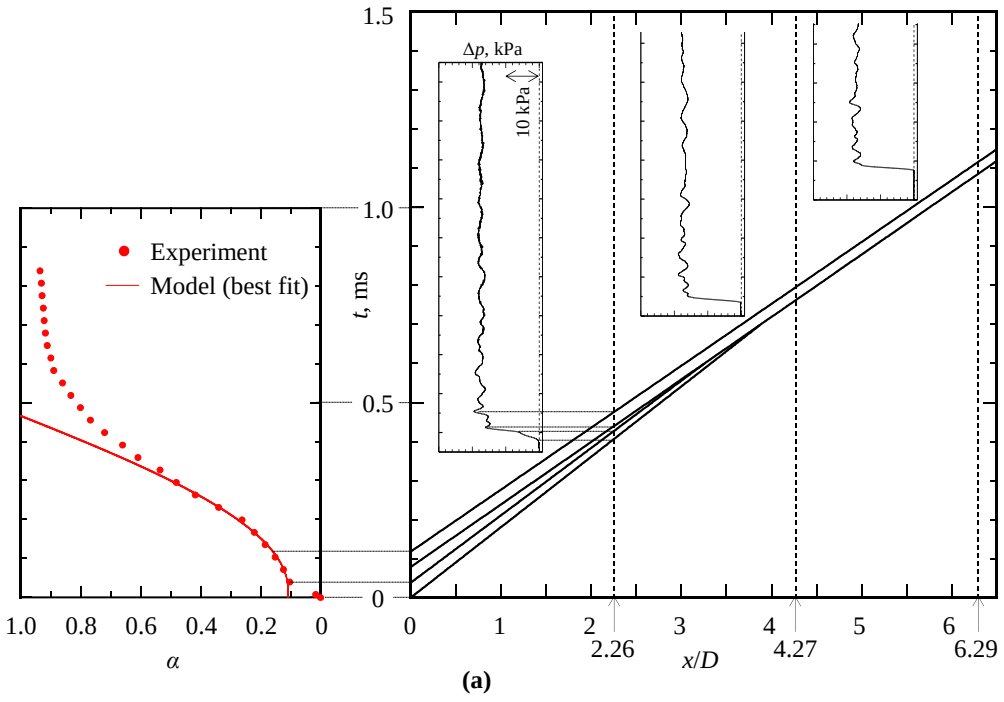


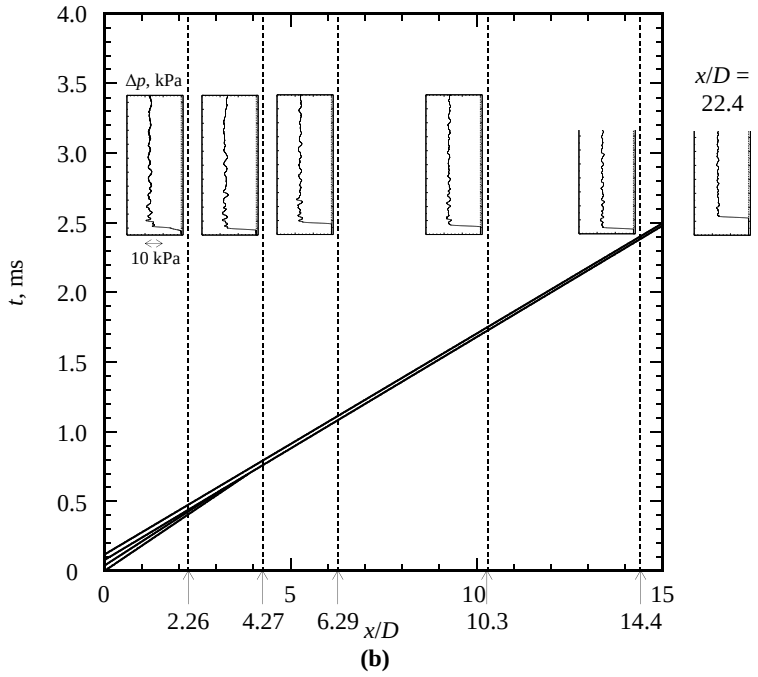


Figure 2.15 $c_+$ diagram at $p_4$ = 140.6 kPa and $p_1$ = 100.6 kPa: (a) $0 \leq x/D \leq 6.5$ and (b) $0 \leq x/D \leq 15$. All compression waves coalesce into the leading shock wave by $x/D$ = 27.1.

## 2.5 Summary of this chapter

The relationship between a cellophane diaphragm rupture and the formation of a weak shock wave was examined as a preliminary study for conducting interaction experiments between a planar shock wave and grid turbulence. The self-shaping opening process of the cellophane diaphragm was observed in the initial stage. A crack propagated at a constant speed of approximately 855 m/s, regardless of the initial pressure difference, humidity, and shock tube size. The number of cracks was expressed as a linear function of the tensile stress acting on the diaphragm before rupture. The experimental results suggested that the strain stress should exceed 23.7 MPa to completely open the cellophane diaphragm and generate a shock wave. To model the motion of the diaphragm opening, a rotational motion model was developed, which successfully expressed the initial process of petal rotation. The characteristic time for sustaining the initial pressure was estimated by analyzing the propagation of the domain of influence caused by the crack propagation. The effective petal acceleration was completed in the initial stage when the petals barely inclined. In this early stage, the petal motion almost matched the flow velocity and did not impede the shock tube flow. Moreover, considering the relationship between the time of the diaphragm opening and the time of the compression wave generation, the opening process corresponding to a period of approximately twice–thrice the completion time of the crack propagation plays a dominant role. This result suggests that the observed cellophane diaphragm opening motion significantly contributed to the weak shock wave formation in the shock tube.

# Chapter 3

# Shock wave modulation by interaction with grid turbulence

## 3.1 Introduction of this chapter

This chapter presents a study on the unsteady modulation of a shock wave propagating through a grid turbulence by conducting systematic experiments using a counter-driver shock tube (CD-ST) (Tamba et al., 2015), which generates two shock waves from two drivers. In these experiments, the CD-ST generated a shock wave and a grid turbulence independently and evaluated the effect of the grid turbulence on the shock wave, which was not under an artificial external force similar to previous direct numerical simulation (DNS) studies (Lee et al. 1993; Larsson and Lele 2009; Larsson et al. 2013; Chen and Donzis 2019). Moreover, the effect of the interaction length can also be evaluated in the CD-ST because the interaction length can be altered by adjusting the burst timings of the two driver sections.

The presented study aimed to experimentally clarify the effects of the shock Mach number ($M_s$), turbulent Mach number ($M_t$), and interaction length between the shock wave and the grid turbulence ($L_i$) (defined subsequently) on the structure of the shock wave during interaction with the turbulence. $M_s$ is obtained by dividing the relative velocity of the shock wave to the flow in front of the shock wave by the speed of sound in the gas in

front of the shock wave. $M_t$ is determined by dividing the root-mean-square value of the velocity fluctuation of the turbulence by the speed of sound in the turbulence. The interaction of the planar shock wave is in the range of $M_s$ = 1.01–1.15 with grid turbulences of $M_t$ = 0.005, 0.009, and 0.014. These ranges are frequently observed in the real world and smaller than the conditions adopted in DNS studies. Thus, whether a "broken" shock regime occurred in such interactions between a weak shock wave and a weak turbulence was also a subject of interest. In addition, because $L_i$ varied with different sets of $M_s$ and $M_t$ values, unsteady propagating effects were investigated. Although these unsteady effects are quite important in applications such as a sonic boom problem, no related research has been conducted except for a recent numerical study in the same period of this investigation (Tanaka et al., 2020). In this chapter, these effects are discussed based on optically visualized side-view images of a shock wave propagating in a turbulent field in terms of the projected thickness and profile.

## 3.2 Experimental setup

### 3.2.1 Counter-driver shock tube

In the experiments, we used a CD-ST, which had drivers on the left- and right-hand sides of the driven section, a cross-section of 120 mm × 120 mm, and a total length of approximately 14 m (Fig. 3.1 (a)). The same diaphragm rupture system as described in the previous chapter was installed in both drivers. Figure 3.1 (b) shows an example $x$–$t$ diagram of the CD-ST obtained in the planar shock wave–grid turbulence interaction experiments. In the figure, the $x$-axis is directed from the left diaphragm to the right and the $\Delta x$-axis is directed from the grid location to the left (which is the direction in which

the grid turbulence advances). The $y$-axis is defined with its origin at the bottom inner wall and is directed to the upper wall. The $z$-axis origin is located on the front inner wall and the axis is directed to the opposite wall. A square grid containing 5 mm × 5 mm square pillars with a mesh size $m$ of 25 mm is located at $x$ = 5.00 m in the setup shown in Fig. 3.1. To weaken the shock wave such that its $M_s$ is smaller than 1.03, sheets of punched metal are installed at $x$ = 1.0 m if necessary. In the experiments, the following series of events occurred in the CD-ST. First, a right-side incident shock wave (R-iSW, where R, i, and SW represent right-side, incident, and shock wave, respectively), proceeded in the left direction after the breaking of the diaphragm of the right-side driver section. When the R-iSW reached the square grid, a grid-transmitted shock wave (R-gSW) propagated toward the left and a weak grid-reflected shock wave (R-rSW) proceeded in the right direction. The uniform flow behind the R-iSW compressed because of the R-rSW. Subsequently, the flow experienced a grid turbulence when it passed through the square grid from the right to the left. Conversely, a left-side incident shock wave (L-iSW) propagated toward the right following the rupture of the left-side diaphragm after a delay time ($t_{delay}$). At a certain point in the driven section, a head-on collision occurred between the R-gSW and the L-iSW, and these shock waves converted into transmitted shock waves R-tSW and L-tSW, respectively. The L-tSW met the grid turbulence, shown as [GT] in Fig. 3.1 (b), proceeding to the left, and an interaction between the planar shock wave and the grid turbulence occurred. The interaction length, $L_i$, is defined as the distance from the head of the grid turbulence to the shock wave arriving at the center of the visualization window. By setting the delay time ($t_{delay}$) between the incident shocks generated by the two drivers, $L_i$ could be controlled well (see Fig. 3.1 (b)).

In the experiments using the CD-ST, three control parameters governed the condition

of the interaction. The initial pressures in the left driver, right driver, and driven section are denoted as $p_{4L}$, $p_{4R}$, and $p_1$, respectively. The initial pressure ratio between the left driver and driven sections, $p_{4L}/p_1$, primarily determined the shock Mach number of the L-tSW, denoted as $M_{s,L\text{-}tSW}$, during the interaction with the grid turbulence. The right-side initial pressure ratio, $p_{4R}/p_1$, decided the shock Mach number of the R-iSW, $M_{s,R\text{-}iSW}$. Because the R-iSW had a one-to-one relationship with the turbulent mean velocity, $p_{4R}/p_1$ determined the turbulent Mach number, $M_t$, of the grid turbulence. The delay time between the left and right incident shock generations, $t_{delay}$, determined the collision point of the incident shock wave at the same set of $M_{s,L\text{-}tSW}$ and $M_t$ and thereby controlled the interaction length, $L_i$. In these experiments, we evaluated the effects of the three parameters—$M_{s,L\text{-}tSW}$, $M_t$, and $L_i$—by appropriately setting the values of $p_1$, $p_{4L}$, $p_{4R}$, and $t_{delay}$. This independent variation of parameters has not been achieved using a typical single-driver shock tube (Dosanjh 1956; Keller and Merzkirch, 1990; Honkan and Andreopoulos, 1992; Briassulis and Andreopoulos 1996; Xanthos et al. 2002; and Agui et al., 2005).

The shadowgraph and schlieren methods were used to visualize the shock wave propagation through a grid turbulence. The visualization system consisted of a high-speed camera (Phantom v1211, Vision Research Inc.; 256 × 256 pixels, 100 kfps) and a synchronized pulse diode laser (CAVILUX Smart, Cavitar Ltd.; wavelength 640 nm, pulse duration 10 ns). This system visualized shock waves before and during their interaction with grid turbulences at a pair of BK7 windows (effective diameter 110 mm) installed on the sidewall at $\Delta x$ = 0.45 m. The optical path length from the test section to the high-speed camera was approximately 20 m, to facilitate the capture of weak density changes with high sensitivity.

In a diaphragm-type shock tube, the generation of a weak planar shock wave is difficult because the opening time of the diaphragm increases with small pressure differences between the driver and driven sections. When the left-side initial pressure difference, $p_{4L} - p_1$, was smaller than 20 kPa, a 21-micrometer-thick cellophane sheet was used as the diaphragm. In this shock tube, the obtained minimum shock Mach number was approximately $M_{s,\ \text{L-iSW}} = 1.04–1.05$. Thus, the planar shock wave needed to be weakened to generate a shock with a Mach number of 1.01. To generate a weak shock, we installed punched metal sheets with small holes in the shock tube at $x = 1.0$ m using a flange. The shock Mach number became small when a shock wave was transmitted through the punched metal sheets (Britan et al., 2006). When the shock wave passed through three sheets of punched metal with a thickness of 1 mm, hole diameter of 2 mm, and blocking ratio 64%, the $M_{s,\text{L-iSW}}$ value decreased from 1.05 to 1.03. To generate a weak shock wave with a Mach number of 1.01, we used 16 sheets of punched metal with a thickness of 0.8 mm, hole diameter of 1 mm, and blocking ratio of 82.5%. Figure 3.2 shows the pressure history of the shock wave at $x = 1.25$ m after it passes through the 16 sheets of punched metal. The pressure rise time for the L-iSW after it passed through the punched metal sheets was shorter than 20 μs. This time was close to the time resolution obtained when the weak shock wave passed over a flush-mounted pressure sensor with a diameter of 5.5 mm. We also confirmed the planarity of the weakened shock wave based on optically visualized images. The pressure behind the shock wave was nearly constant. Therefore, a planar shock wave with a Mach number of approximately 1.01 was generated well in the CD-ST.

In the CD-ST, a hot-wire anemometer probe was damaged by the debris from the finely ruptured cellophane diaphragm that impinged against it, and this effect became

serious in higher pressure difference operation. In this study, a 100-micrometer-thick polyester diaphragm was used when the pressure difference between the driver and driven sections exceeded 100 kPa, to suppress the debris generation by the diaphragm rupture. The polyester diaphragm did not show a degraded opening performance at large pressure differences, and the shock wave formation distance was within the allowable value in these experiments. Consequently, a hot-wire anemometer probe was used to measure the grid turbulence with a flow velocity of approximately 160 m/s without any damage to the probe.

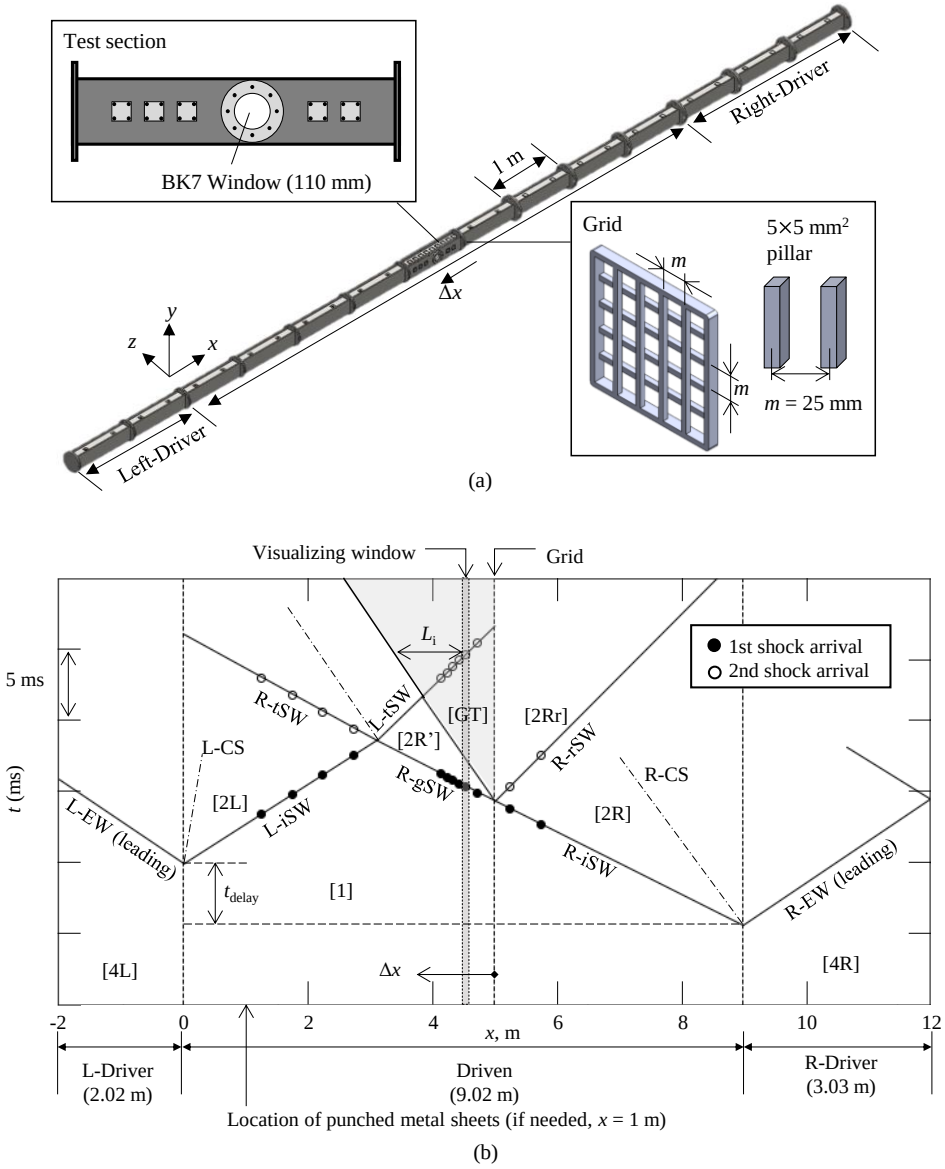


Figure 3.1 (a) Schematics of CD-ST. (b) Example of *x*–*t* diagram of shock–turbulence interaction for $M_{s,L\text{-}tSW}$ = 1.05, $M_{s,R\text{-}gSW}$ = 1.32, and $L_i$ = 1185 mm. L-, from the left driver; R-, from the right driver; i, incident; t, transmitted; g, grid transmitted; r, reflected from the grid; SW, shock wave; EW, expansion waves; CS, contact surface; [1], driven section; [4L], left driver; [4R] right driver; [2L], state behind L-iSW; [2R], state behind R-iSW; [2R'], state behind R-gSW; [2Rr], state behind R-rSW; [GT], grid turbulence state.

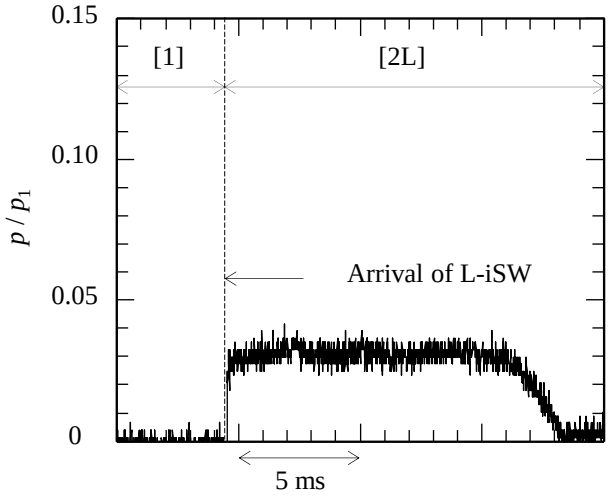


Figure 3.2 Example of raw pressure history of L-iSW at $x$ = 1.25 m after it passed through 16 sheets of punched metal. The shock Mach number was 1.008

### 3.2.2 Flow characteristics in counter-driver shock tube

Table 3.1 lists the initial pressure conditions and measured shock Mach numbers (The measured characteristics of grid turbulence are also shown in the table and are explained later in the following section). The propagation velocities of the L-iSW, R-iSW, and R-gSW were measured by the time-of-flight principle. The shock Mach number, $M_s$, was calculated by dividing the shock wave velocity by the speed of sound in the gas in the driven section. We assumed that the gas was calorically perfect, i.e., the specific heat ratio was constant ($\gamma = 1.4$). Because the L-tSW propagated in a uniform flow behind the R-gSW, the shock Mach number was calculated by the pressure jump obtained by the pressure sensor. Here, the static pressure in states [2R'] and [GT] were assumed to be constant because the boundary between them was the contact surface.

Table 3.1 Measured shock wave and grid turbulence characteristics and the initial operation conditions

| $M_{s,\,\text{L-tSW}}$ | $\widetilde{M}_t$ | $p_{4L}$ (kPa) | $p_1$ (kPa) | $p_{4R}$ (kPa) | Sheets of punched metal | $\tilde{L}$ (mm) | $\widetilde{Re}_m$ | $\widetilde{Re}_\lambda$ | $M_{s,\,\text{L-iSW}}$ | $M_{s,\,\text{R-iSW}}$ | $M_{s,\,\text{R-gSW}}$ |
|---|---|---|---|---|---|---|---|---|---|---|---|
| 1.012 ± 0.001 | 0.005 ± 0.001 | 61.9 | 48.2 | 75.2 | Thickness: 0.8 mm, hole diameter: 1 mm, blocking ratio: 0.825, and 16 sheets | 7.9 | $4.1 \times 10^4$ | 126 | 1.013 ± 0.001 | 1.094 ± 0.001 | 1.089 ± 0.001 |
| 1.011 ± 0.001 | 0.009 ± 0.001 | 51.3 | 39.6 | 93.3 | | 10.3 | $7.7 \times 10^4$ | 357 | 1.013 ± 0.000 | 1.189 ± 0.001 | 1.179 ± 0.001 |
| 1.009 ± 0.003 | 0.014 ± 0.001 | 42.0 | 32.0 | 138.2 | | 6.0 | $9.6 \times 10^4$ | 1034 | 1.014 ± 0.001 | 1.340 ± 0.006 | 1.319 ± 0.006 |
| 1.029 ± 0.001 | 0.005 ± 0.001 | 60.3 | 48.2 | 75.2 | Thickness: 1 mm, hole diameter: 2 mm, blocking ratio: 0.64, and 3 sheets | 7.9 | $4.1 \times 10^4$ | 126 | 1.031 ± 0.001 | 1.094 ± 0.000 | 1.090 ± 0.000 |
| 1.026 ± 0.001 | 0.009 ± 0.001 | 49.5 | 39.6 | 93.3 | | 10.3 | $7.7 \times 10^4$ | 357 | 1.029 ± 0.001 | 1.188 ± 0.001 | 1.179 ± 0.001 |
| 1.021 ± 0.002 | 0.014 ± 0.001 | 40.0 | 32.0 | 138.2 | | 6.0 | $9.6 \times 10^4$ | 1034 | 1.026 ± 0.001 | 1.341 ± 0.003 | 1.318 ± 0.005 |
| 1.047 ± 0.001 | 0.005 ± 0.001 | 61.9 | 48.2 | 75.2 | w/o | 7.9 | $4.1 \times 10^4$ | 126 | 1.049 ± 0.001 | 1.092 ± 0.000 | 1.088 ± 0.000 |
| 1.047 ± 0.003 | 0.009 ± 0.001 | 51.3 | 39.6 | 93.3 | | 10.3 | $7.7 \times 10^4$ | 357 | 1.050 ± 0.001 | 1.188 ± 0.001 | 1.179 ± 0.001 |
| 1.047 ± 0.002 | 0.014 ± 0.001 | 42.0 | 32.0 | 138.2 | | 6.0 | $9.6 \times 10^4$ | 1034 | 1.053 ± 0.002 | 1.341 ± 0.002 | 1.317 ± 0.002 |
| 1.105 ± 0.001 | 0.005 ± 0.001 | 80.2 | 48.2 | 75.2 | | 7.9 | $4.1 \times 10^4$ | 126 | 1.110 ± 0.000 | 1.094 ± 0.000 | 1.090 ± 0.001 |
| 1.100 ± 0.001 | 0.009 ± 0.001 | 65.9 | 39.6 | 93.3 | | 10.3 | $7.7 \times 10^4$ | 357 | 1.111 ± 0.000 | 1.190 ± 0.000 | 1.180 ± 0.001 |
| 1.150 ± 0.001 | 0.005 ± 0.001 | 97.8 | 48.2 | 75.2 | | 7.9 | $4.1 \times 10^4$ | 126 | 1.157 ± 0.000 | 1.095 ± 0.000 | 1.091 ± 0.001 |
| 1.150 ± 0.002 | 0.009 ± 0.001 | 82.7 | 39.6 | 93.3 | | 10.3 | $7.7 \times 10^4$ | 357 | 1.163 ± 0.001 | 1.189 ± 0.001 | 1.180 ± 0.001 |

### 3.2.3 Grid turbulence characteristics

The state in the grid turbulence [GT] was compressed because of the grid-reflected shock R-rSW. Thus, the temperature in the state [GT] was higher than that in the upstream uniform flow [2R']. To quantify the grid turbulence characteristics, we measured the total temperature and velocity using cold and- hot-wire anemometers. The total temperature was measured by varying the $\Delta x$- and $y$-direction values and fixing the $z$-direction value at 60 mm. As defined earlier, the $y$-axis was defined with its origin at the bottom inner wall and direction to the upper wall. The $z$-axis origin was located at the front inner wall and directed to the opposite wall. The measurement range in the $y$-direction was $5 \leq y \leq$ 60 mm, and the flow symmetry was assumed for $y > 60$ mm. Figure 3.3 shows the normalized mean total temperature in the state [GT] versus the initial temperature in the driven section, $T_1$, in the same $x$ plane. The error bars represent the standard deviations. The measurement point in the $y$-direction was changed while maintaining the same distance from the grid, $\Delta x$. The measurement points in the $\Delta x$-direction were $\Delta x = 0.45$ and 0.75 m for $M_{s,R\text{-}gSW} = 1.09$ and $x = 0.45$ and 0.95 m for $M_{s,R\text{-}gSW} = 1.18$ and 1.32, respectively. A nearly uniform temperature field was formed at $20 \leq y \leq 60$ mm under all conditions. The total temperature uniformity was maintained in the $y$-direction for the measured range in the $\Delta x$-direction. The total temperature in region $0 < y < 20$ mm was lower than that in the central area. On the $y$–$z$ plane with $\Delta x = 0.45$ m, the total temperatures measured at $y = 60$ and 10 mm were different: approximately 3, 4.5, and 8 K under the condition of $M_{s,R\text{-}gSW} = 1.09$, 1.18, and 1.32, respectively. This low-temperature field was generated because of the wall effects. The grid size, $m$ ($m = 25$ mm), was considered to have a dominant effect on the creation of the low-temperature region because this region was similar ($0 < y < 20$ mm) under all grid turbulences. The

measurement results found that the core region of the grid turbulence was approximately 80 mm × 80 mm in the center of the CD-ST under the symmetrical condition assumption. Thus, in these experiments, only the phenomena around the center of the CD-ST were evaluated.

An I-type constant-temperature hot-wire anemometer was calibrated based on the obtained total temperature information of the grid turbulence, and the velocity was measured. The response limit of the hot-wire anemometer was approximately 20 kHz, as discussed in Appendix B. Figure 3.4 shows the turbulent Mach number, $M_t$, of the grid turbulence as a function of the distance from the grid, $\Delta x$. The measurement point was the shock tube center: $y = z = 60$ mm. The isotropic nature of the grid turbulence generated in a shock tube has already been confirmed in previous experimental research. In the experiments by Agui et al. (2005), the measurements of three velocity components supported that the grid-generated turbulence in the shock tube was isotropic. Our conditions for the grid turbulence characteristics, such as the mesh Reynolds number, were close to those in their experiments. The turbulent Mach number was calculated using the root-square-mean value of the measured $x$-component of the velocity fluctuation, $u'$, assuming that the grid turbulence was isotropic. Thus, the relationship, $M_t = \sqrt{3}u'/a_{GT}$, was used, where $a_{GT}$ is the speed of sound in the grid turbulence. Here, to evaluate the measured grid turbulence characteristics, decay constant $k$ of the grid turbulence was considered. Typically, grid turbulence shows a power law decay of the turbulence intensity $(u'/U)^2$ as a function of distance from the grid, where $U$ denotes the mean velocity of the grid turbulence. Decay constant $k$ shows the decay tendency of the grid turbulence, expressed as $(u'/U)^2 = (\Delta x/m)^{-k}$. Here, $m$ denotes the grid size. The value of $k$ was 0.9, 1.2, and 0.3 for $M_{s,R\text{-}gSW} = 1.09$, 1.18, and 1.32, respectively. The decay tendency

and the value of $k$ were consistent with the grid turbulence measurement results obtained in a wind tunnel and a shock tube in previous studies (Roach, 1987; Briassulis, et al. 2001; Kitamura et al., 2014). Some parameters of the grid turbulence changed with increasing distance from the grid. To distinguish these value changes depending on the distance from the grid, we express the representative value using a tilde $(\tilde{})$. For example, the representative of the turbulent Mach number is presented as $\widetilde{M}_t$. In this study, the representative values were adopted for the value at $\Delta x$ = 0.45 m, the location in the center of the window where the shock wave was visualized using the optical method. The representative values of the turbulent Mach number were $\widetilde{M}_t$ = 0.005, 0.009, and 0.014 for $M_{s,R\text{-}gSW}$ = 1.09, 1.18, and 1.32, respectively. Table 3.1 also lists representative values of integral scale $\tilde{L}$, mesh Reynolds number $Re_m = Um/v$, and turbulent Reynolds number based on the Taylor microscale, $Re_\lambda = u'\lambda/v$. In this expression, $v$ is the kinematic viscosity, $u'$ is the root mean square of the velocity fluctuations, and $\lambda$ is the Taylor microscale. The integral scale of turbulence was obtained by calculating an autocorrelation coefficient using the measured velocity fluctuation signal. Because the integral scale of the turbulence physically corresponded to the length of the dominant scale eddies in a turbulent flow, the interaction length was normalized by $\tilde{L}$ in subsequent evaluations.

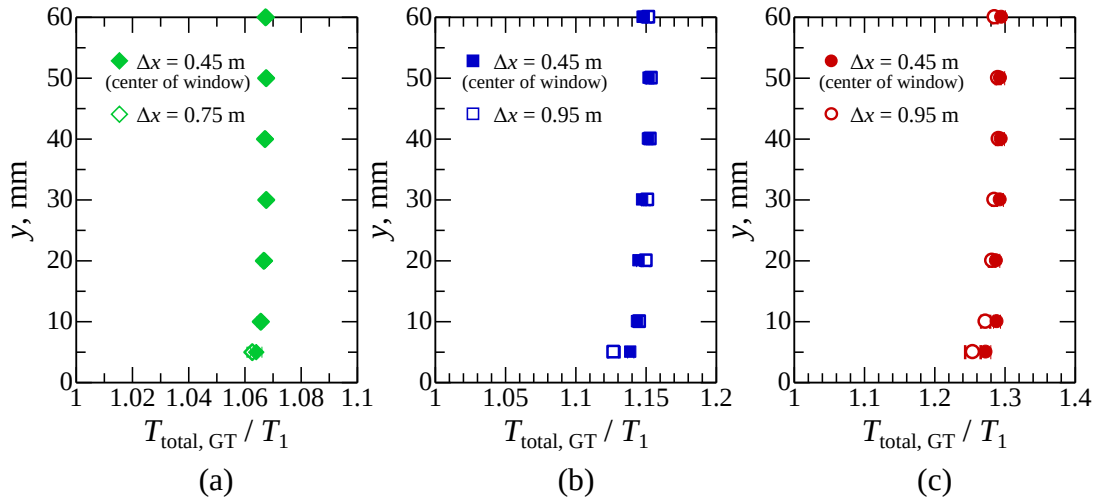


Figure 3.3 Distribution of the normalized total temperature of the grid turbulence in the $y$-direction: (a) $M_{s,R\text{-}gSW} = 1.09$, (b) $M_{s,R\text{-}gSW} = 1.18$, and (c) $M_{s,R\text{-}gSW} = 1.32$.

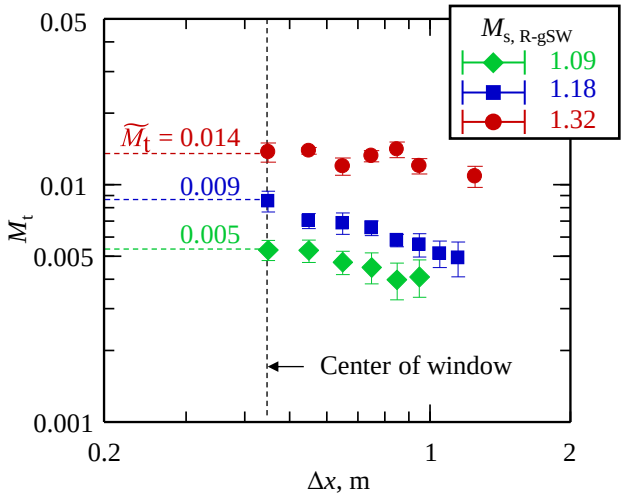


Figure 3.4 Turbulent Mach number as a function of the distance from the grid.

## 3.3 Effects of turbulence on side projected shock wave

In this section, we present the qualitative study conducting using projected shock wave images. The shadowgraph and schlieren methods were used to visualize the shock wave propagation through a grid turbulence, as described in previous sections. The proceeding direction of the planar shock wave was from the left to the right, and that of the grid turbulence direction was from the right to the left. These are shown in Fig. 3.1 (b). To eliminate stationary noise such as scratches on the window, a reference image was subtracted from the obtained images (Kim et al., 2010). The images included in this study were the differential images obtained after subtraction. The reference image was obtained at a quiescent gas state before operation of the CD-ST.

Figure 3.5 shows the projected images of the planar shock wave with $M_{s,\,\mathrm{L\text{-}tSW}} \approx 1.01$ interacting with a grid turbulence. The horizontal axis represents the dimensionless interaction length normalized by the representative value of the integral length scale of the grid turbulence, $L_i/\tilde{L}$. The vertical axis represents the representative value of the turbulent Mach number, $\widetilde{M}_t$. The images enclosed in solid- and dashed-line frames were visualized by the shadowgraph and schlieren methods, respectively. An area with approximately 80 mm in height in the center of the shock tube was extracted as the evaluation region. A negative value of $L_i/\tilde{L}$ indicated that the shock wave had not started interacting with the grid turbulence. Under all conditions, the shock waves were almost planar with $L_i/\tilde{L} < 0$. In the interaction with the weakest turbulence ($\widetilde{M}_t = 0.005$), the projected thickness of the shock wave increased with increasing $L_i/\tilde{L}$. At $L_i/\tilde{L} = 41.6$, some lines showing density changes were observed because a multidimensionally deformed shock wave was observed from the side view. For the interaction with the grid turbulence with $\widetilde{M}_t = 0.009$, shock waves were not easily detected using the shadowgraph method

when $L_i/\tilde{L}$ was above 33.7. Using the schlieren method, the deformation of a shock wave was observed even for $L_i/\tilde{L}$ = 92.8. The lines representing the density gradient by the shock wave were dispersed in the *x*- and *y*-directions. This state is termed as a "dispersed profile" in this thesis. This profile showed a large deformation of the shock wave in this state. For the interaction with the strongest turbulence ($\widetilde{M}_t$ = 0.014), the shock wave was deformed by the turbulence at $L_i/\tilde{L}$= 26.4. When $L_i/\tilde{L}$ was above 42.5, the density changes in the projected image of the shock wave became considerably weak. Using the shadowgraph and schlieren methods, the visualized shock waves exhibited dispersed profiles. For $L_i/\tilde{L}$ > 100, the density changed smoothly because the shock wave caused a loss in the sharp lines, which was not observed in the initial stage of the interaction. The projected shock wave region weakened and expanded in the traveling direction, and we could not easily detect the edge of the shock wave.

Figure 3.6 shows the images of shock waves with $M_{s,\,\text{L-tSW}}$ = 1.02–1.03 interacting with a grid turbulence. In the interaction with the turbulence at $\widetilde{M}_t$ = 0.005, the shock wave was planar even when it proceeded through the turbulence. Under this condition, the projected thickness of the shock wave slightly increased because of the turbulence. For the grid turbulence at $\widetilde{M}_t$ = 0.009, the shock wave was detected during the entire interaction, and the projected thickness was greater than that of $\widetilde{M}_t$ = 0.005 under approximately the same $L_i/\tilde{L}$. For the interaction with the strongest turbulence ($\widetilde{M}_t$ = 0.014), the shock wave remained planar until $L_i/\tilde{L}$ < 46.2. When $L_i/\tilde{L}$ exceeded 53.3, the shock wave dispersed in the *x*-direction. Numerous lines remained relatively sharp in the visualized region. Using the shadowgraph and schlieren methods, the shock wave lost the single-line profile appearance and locally disappeared in the projected images. However, unlike the weak shock wave of $M_{s,\,\text{L-tSW}} \approx 1.01$, the sharp lines did not vanish entirely.

Figures 3.7–9 show the projected side-view images of the shock–turbulence interactions of planar shock waves with Mach numbers of 1.05, 1.10, and 1.15. Unlike the interaction involving the weaker shock wave with $M_{s,L\text{-}tSW} < 1.03$, the remaining shock waves did not show dispersed profiles. The line representing the change in the density of the shock wave remained sharp in the entire $y$-direction.

In conclusion, for an interaction involving a weak shock wave with $M_{s,L\text{-}tSW} < 1.03$, the projected thickness of the shock wave increased with increasing $L_i/\tilde{L}$. Under the same intensity of the shock wave, the projected thickness of the shock wave propagating in the grid turbulence increased with the increase in the turbulent Mach number. When the intensity of the grid turbulence was the same, an increase in $M_{s,\,L\text{-}tSW}$ prevented an increase in the projected thickness of the shock wave against increases in $L_i/\tilde{L}$.

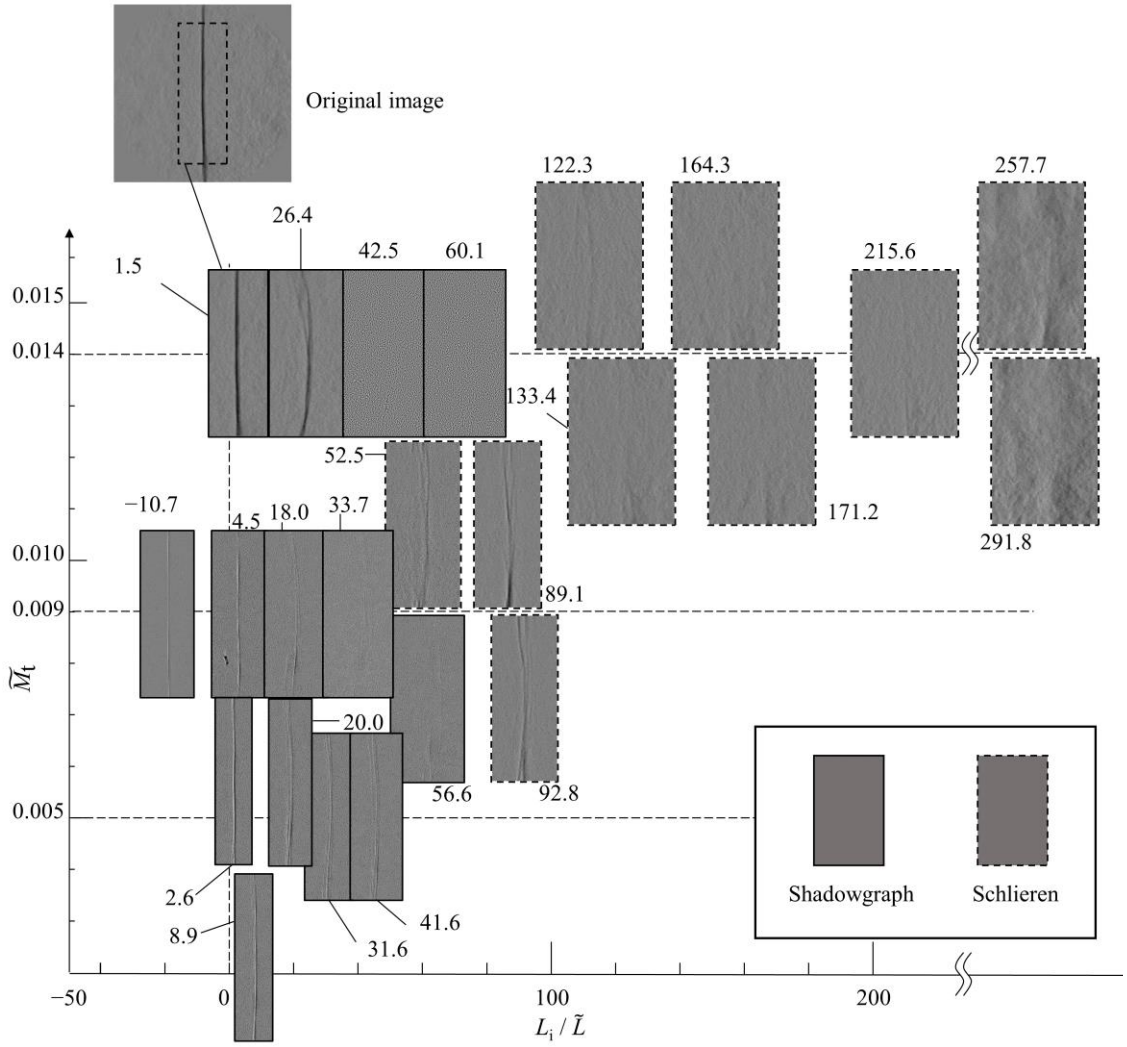


Figure 3.5 Projected images of the shock waves propagating through the grid turbulences for ($M_{s,L\text{-}tSW}$, $\widetilde{M}_t$) = (1.012 ± 0.001, 0.005 ± 0.001), (1.011 ± 0.001, 0.009 ± 0.001), and (1.009 ± 0.003, 0.014 ± 0.001). The central area from $y$ = 20 to 100 mm is extracted from the differential images.

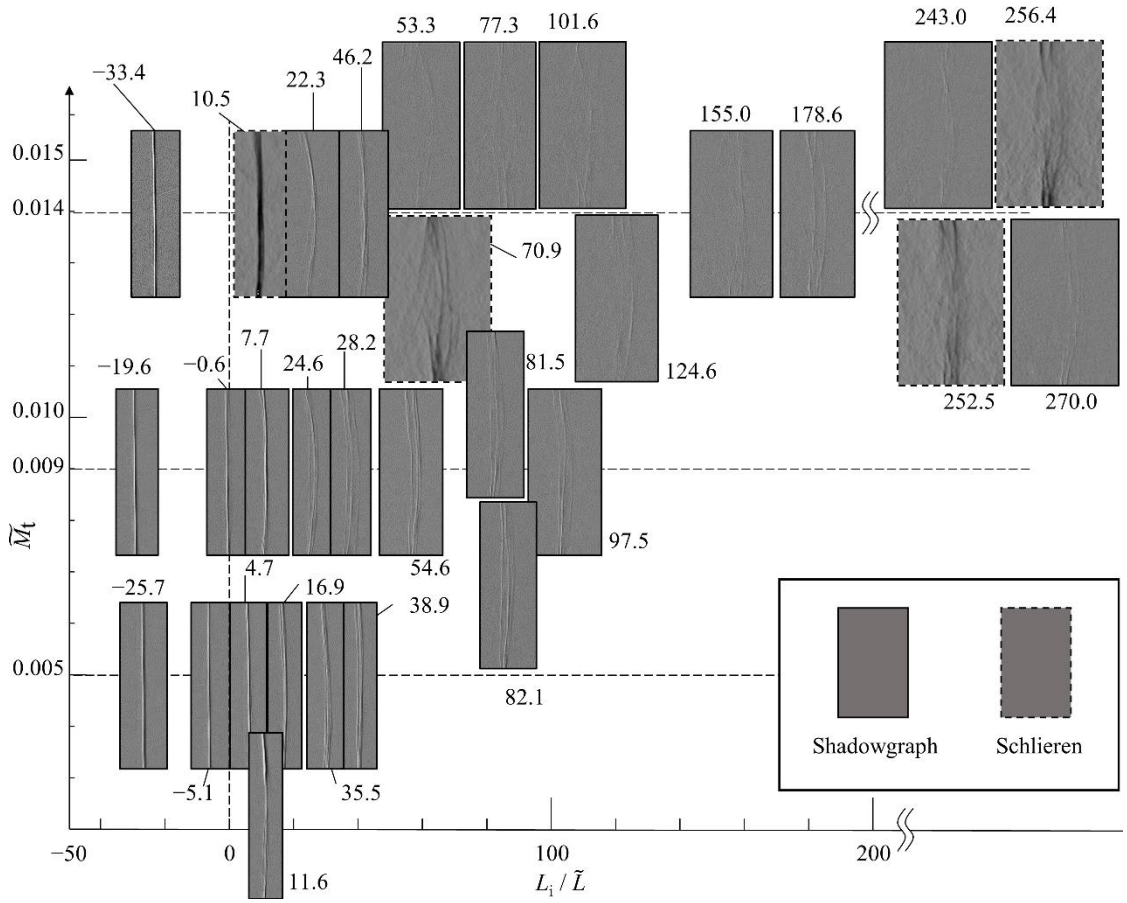


Figure 3.6 Projected images of the shock waves propagating through the grid turbulences for ($M_{s,L\text{-}tSW}$, $\widetilde{M}_t$) = (1.029 ± 0.001, 0.005 ± 0.001), (1.026 ± 0.001, 0.009 ± 0.001), and (1.021 ± 0.003, 0.014 ± 0.001).

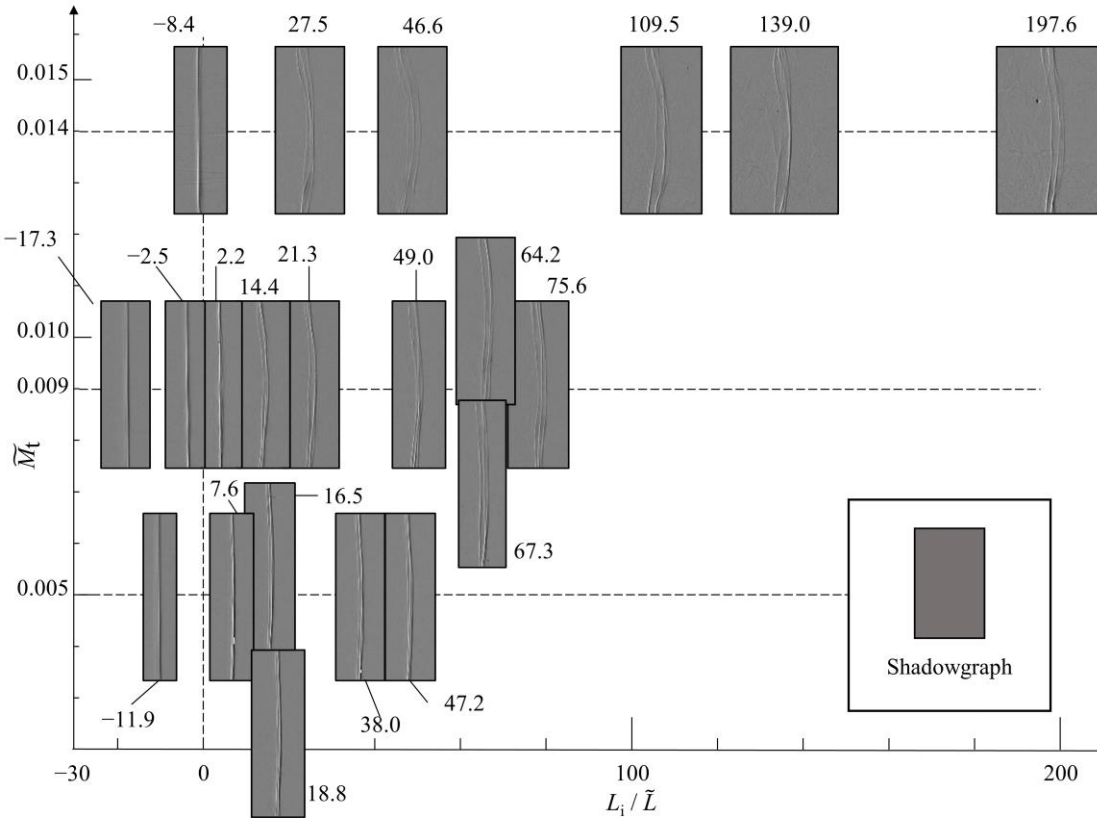


Figure 3.7 Projected images of the shock waves propagating through the grid turbulences for ($M_{s,L\text{-}tSW}$, $\widetilde{M}_t$) = (1.047 ± 0.001, 0.005 ± 0.001), (1.047 ± 0.003, 0.009 ± 0.001), and (1.047 ± 0.002, 0.014 ± 0.001).

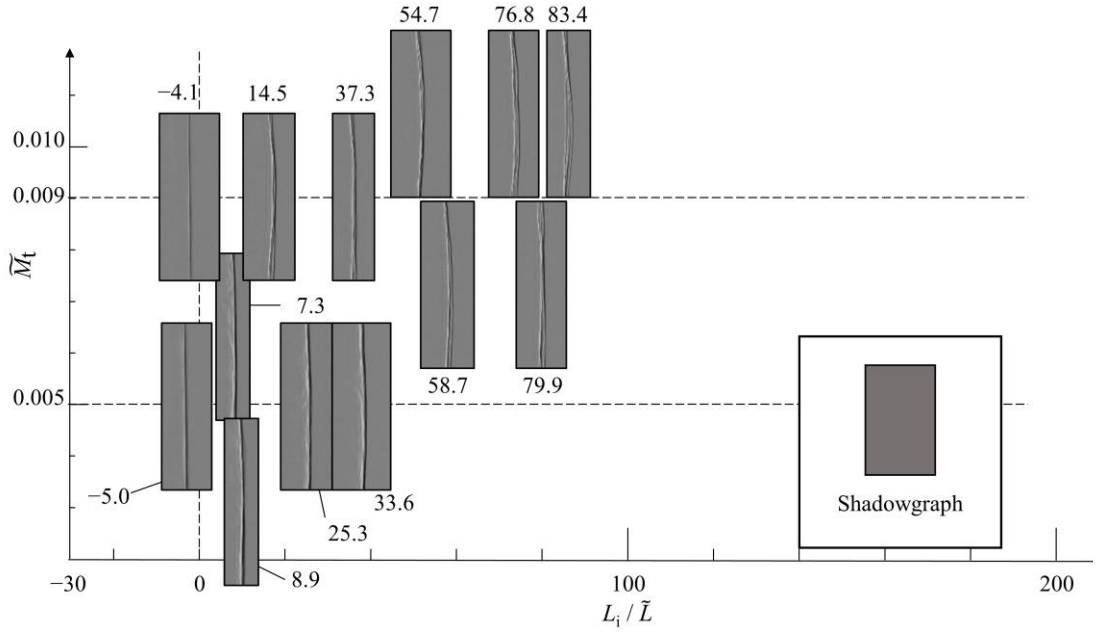


Figure 3.8 Projected images of the shock waves propagating through the grid turbulences for ($M_{s,L\text{-}tSW}$, $\widetilde{M}_t$) = (1.105 ± 0.001, 0.005 ± 0.001) and (1.100 ± 0.001, 0.009 ± 0.001).

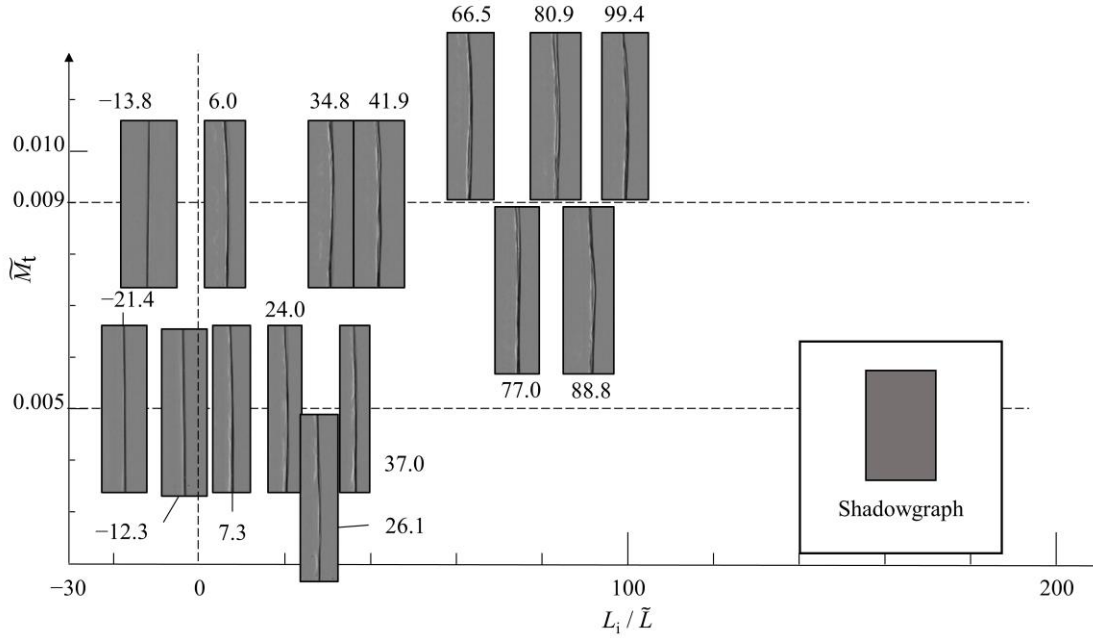


Figure 3.9 Projected images of the shock waves propagating through the grid turbulence for ($M_{s,L\text{-}tSW}$, $\widetilde{M}_t$) = (1.150 ± 0.001, 0.005 ± 0.001) and (1.150 ± 0.002, 0.009 ± 0.001).

Subsequently, we analyzed the projected images to investigate the planar shock modulations caused by the grid turbulences. We evaluated the edge profiles and thicknesses in the projected images captured from the side view. In the typical schlieren and shadowgraph methods, the information in the same direction as the light path (the $z$-direction, in this study) is integrated and shown on an image. Therefore, if a shock wave was not detected in the projected images, the shock wave was considered to locally lose a sharp density change in the $x$ direction for the entire light path direction. In this shock wave edge analysis, the evaluation range was $N_y$ pixels in the $y$-direction around the center of the shock tube and all the pixels in the $x$-direction. The value of $N_y$ was 80 in this analysis (approximately 32 mm in the $y$-direction). The edges in the projected images were extracted using the Canny method (Canny, 1986), which is one of the most famous edge detection methods. Figure 3.10 shows examples of the left and right edges of a shock wave detected in the analyzed area. In the location where the edge was not found, the shock wave could lose its discontinuous property change profile in the $x$-direction for the entire $z$-direction. At a certain point $y_i$ in the $y$-direction, where $i$ represents the sequential number, the existence of the shock wave was evaluated in the $x$-direction. This operation was continued from $i = 0$ to $N_y$. Subsequently, the number of $y$-direction pixels in which the shock wave was not found in the $x$-direction, $N_{y,\text{ w/o shock}}$, was counted. The undetectable ratio of the shock wave, $\beta$, was defined as the ratio of the $y$-direction pixels where the shock wave front did not exist throughout the $x$-direction, and it is calculated as follows:

$$\beta = N_{y,\text{w/o shock}} / N_y. \tag{3.1}$$

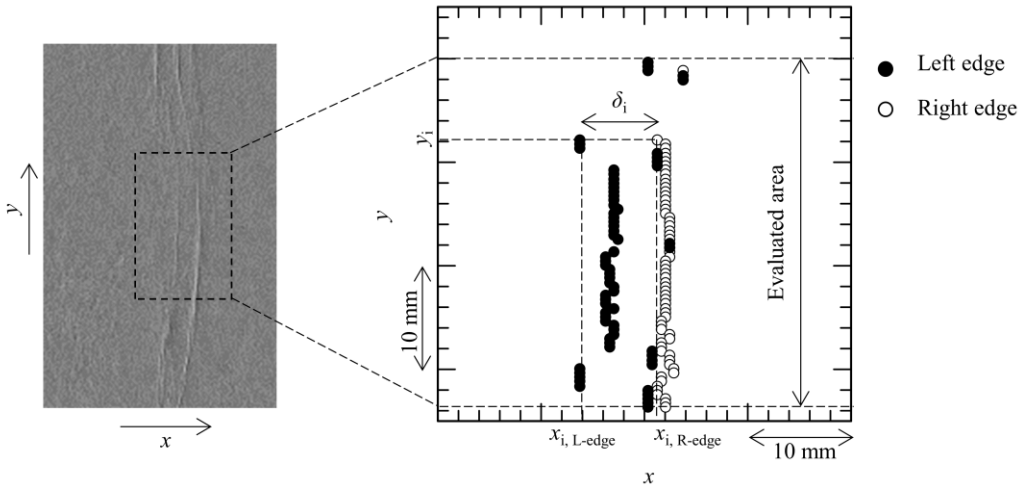


Figure 3.10 Example of detected shock edge from shadowgraph image for ($M_{s,\ L\text{-}tSW}$, $\widetilde{M}_t$, $L_i/\tilde{L}$) = (1.021 ± 0.002, 0.014 ± 0.001, 124.6).

Figure 3.11 shows the dependence of the undetectable ratio, $\beta$, on $L_i/\tilde{L}$. The same process was applied to the shadowgraph and schlieren images. The undetectable ratios of the projected shock waves obtained from the shadowgraph (closed symbol) and schlieren (open symbol) images presented similar tendency except under some conditions. Figure 3.11 (a) shows the undetectable ratio variations of the interacting shock wave with $M_{s,L\text{-}tSW} \approx 1.01$. For the interaction with the weakest turbulence ($\widetilde{M}_t = 0.005$), the undetectable ratio was zero during the entire observed interaction. In the interaction with $\widetilde{M}_t = 0.009$, the projected shock wave locally lost its edge when $L_i/\tilde{L}$ exceeded 20. The value of $\beta$ was in the range of 0.1–0.4 at $L_i/\tilde{L} \approx 40$. In the schlieren image obtained at $L_i/\tilde{L} \approx 90$, the undetectable ratio returned to zero. However, only under this condition, the shadowgraph and schlieren images could be considered to yield different $\beta$ owing to the difference in the detection sensitivity. For the interaction with the strongest turbulence ($\widetilde{M}_t = 0.014$),

the undetectable ratio sharply increased above $L_i/\tilde{L}$ = 30 and nearly reached unity when $L_i/\tilde{L}$ exceeded 100. The visualized image in Fig. 3.5, whose undetectable ratio is approximately 1, shows that the shock wave lost its sharp profile, demonstrating continuous property changes in the *x*-direction.

The shock waves with $M_{s,L\text{-}tSW}$ = 1.02–1.03 (Fig. 3.11 (b)) showed perfectly detectable profiles in the interaction with the grid turbulences with $\widetilde{M}_t$ = 0.005 and 0.009. In the interaction with the strongest turbulence ($\widetilde{M}_t$ = 0.014), the undetectable ratio started to increase at approximately $L_i/\tilde{L}$ = 50 and obtained a value in the range of 0.1–0.5 at $L_i/\tilde{L}$ > 250. The relatively strong shock waves with $M_{s,L\text{-}tSW}$ = 1.05, 1.10, and 1.15 showed detectable profiles in the projected images under all conditions of the grid turbulences: the undetectable ratio was zero (Fig. 3.11 (c)–(e)). Because the shock wave maintained the discontinuous profile in these conditions, these results corresponded to the "wrinkled" state, as reported in the DNS studies.

In the shock wave edge analysis of the projected images, the shock–turbulence interactions with ($M_{s,L\text{-}tSW}$, $\widetilde{M}_t$) ≈ (1.01, 0.009), (1.01, 0.014), and (1.02, 0.014) led to an undetectable profile of the shock wave on the projected image when $L_i/\tilde{L}$ reached approximately 20–50. These three conditions corresponded to weak shock waves and relatively intense turbulences, respectively. In addition, these conditions satisfied the criterion of the appearance of a broken shock: $M_t \geq 0.6(M - 1)$, in which the shock wave front could become subsonic, as proposed by Donzis and Larsson et al. (Donzis, 2012; Larsson et al., 2013). Note that *M* denotes the upstream flow Mach number of the stationary shock wave in the studies conducted in a shock fixed system. From the viewpoint of the strength of the shock wave, the *M* used in the shock fixed system and $M_s$ used in the shock propagating system (this research) were the same. Because the projected

images of a shock wave were obtained by the optical system with a constant sensitivity remaining constant throughout the experiments, our experimental results showed consistency with previous DNS study results, although the shadowgraph and schlieren visualizations depended on the sensitivity in general. In addition to this agreement, an important difference between the experimental and numerical results was observed. Our experimental results emphasized the effect of $L_i/\tilde{L}$ on the appearance of the "broken" regime: $L_i/\tilde{L} \approx 20$ was required for the "broken" regime to appear. The aspect of interaction length has not been investigated in detail in numerical studies. To clarify the relationship between the present experimental results and a DNS study, a systematic analysis and comparison will be performed in future research.

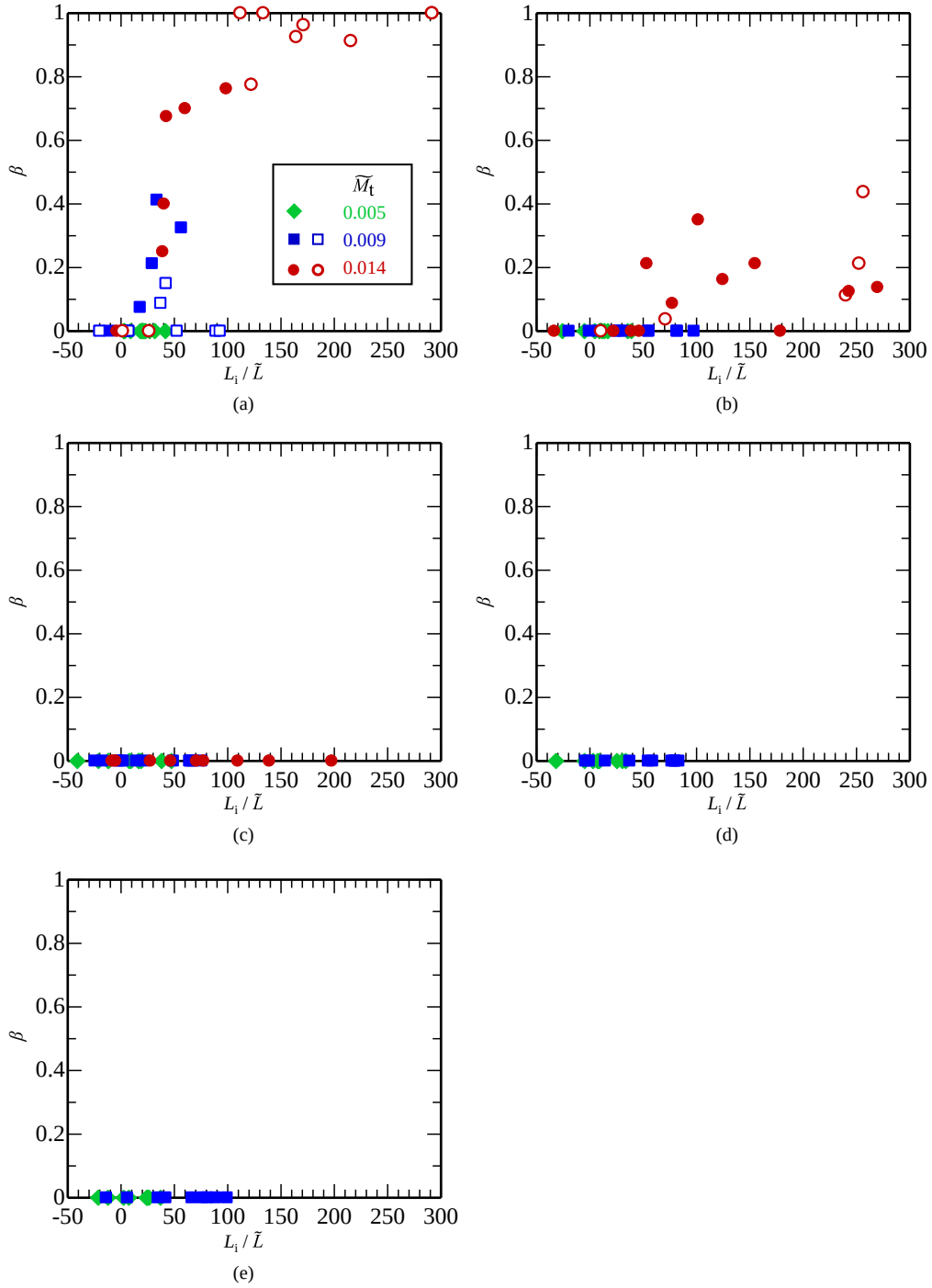


Figure 3.11 $\beta$ versus $L_i/\tilde{L}$ for (a) $M_{s,L\text{-}tSW} \approx 1.01$, (b) $M_{s,L\text{-}tSW} \approx 1.02$–$1.03$, (c) $M_{s,L\text{-}tSW} \approx 1.05$, (d) $M_{s,L\text{-}tSW} \approx 1.10$, and (e) $M_{s,L\text{-}tSW} \approx 1.15$. Close symbols: results calculated using the shadowgraph image. Open symbols: results calculated using the schlieren image.

Subsequently, the projected thickness of the shock wave region was evaluated. The projected thickness of a shock wave is an important parameter corresponding to the deformation extent of the shock wave in the $x$-direction. The projected shock wave region for $y = y_i$ was defined as the distance between the left and right edges and expressed as $\delta_i = x_{i,\text{R-edge}} - x_{i,\text{L-edge}}$. The average value of $\delta_i$ in the range of $i = 0$ to $N_y$ was defined as the projected shock wave thickness, $\delta$. Here, the averaging operation was only conducted for $y_i$, where the shock thickness was definable. In the shadowgraph method, a second derivative of the density change is expressed as a change in the brightness. Because a single planar shock wave had light and dark areas in its images, the minimum shock wave thickness had two pixels on the obtained image. A pixel in the projected image corresponded to approximately 0.4 mm. Therefore, the resolvable minimum thickness of the shock wave region obtained from the image is approximately 0.8 mm. Under all conditions, $\delta$ before interaction with the grid turbulence was approximately 1–2 mm. This thickness was the limit resolution of the shock waves in the images in this study, and this resolution did not correspond to the actual thickness of the shock wave. After the shock wave entered the grid turbulence, the projected thickness of the shockwave increased with increasing interaction length. Therefore, the projected thickness during the interaction with the turbulence reflects the deformation region of the shock wave in the $x$-direction by the turbulence interaction. Moreover, we evaluated the projected thickness as the deformation extent of the shock wave.

In Fig. 3.12 (a), the dimensionless projected thickness normalized by the integral scale of the grid turbulence, $\delta/\tilde{L}$, is shown as a function of $L_i/\tilde{L}$. The value of $\delta/\tilde{L}$ of the weakest shock wave with $M_{s,\text{L-tSW}} \approx 1.01$ (Fig. 3.12 (a)) increased after the shock wave interacted with the grid turbulence of $\widetilde{M}_t = 0.005$. $\delta/\tilde{L}$ was 0.2−0.4 at $L_i/\tilde{L} > 20$. In the interaction

with the turbulence at $\widetilde{M}_t$ = 0.009 and 0.014, the shock wave was deformed considerably by the grid turbulence. Because the projected image showed a dispersed undetectable profile and did not maintain sharp lines, the projected thickness of the shockwave region was difficult to precisely define. In the interaction of the shock waves with the law, $M_{s,L\text{-}tSW}$ = 1.02−1.03 (Fig. 3.12 (b)) and $\delta/\tilde{L}$ of the shock region increased rapidly when $L_i/\tilde{L}$ was 0–50. In the interactions with the turbulences with $\widetilde{M}_t$ = 0.005 and 0.009, the normalized projected thicknesses became approximately 0.4 and 0.5, respectively, at $L_i/\tilde{L}$ = 40. In the interaction with the turbulence at $\widetilde{M}_t$ = 0.014, the shock wave region significantly expanded. When $L_i/\tilde{L}$ was above 53.3, the shock wave dispersed, and at $L_i/\tilde{L}$ = 30, the value of $\delta/\tilde{L}$ reached 0.5. Because this value was close to the standard deviation of the average thickness, the expansion and partial disappearance of a shock wave were confirmed. $\delta/\tilde{L}$ with $M_{s,\,L\text{-}tSW} \approx 1.05$ (Fig. 3.12 (c)), whose undetectable ratio was 0 under all interactions, increased moderately compared to the thickness of the weaker shock waves. As the turbulent Mach number increased, the increase in $\delta/\tilde{L}$ became slightly steeper. For the shock waves with $M_{s,\,L\text{-}tSW} \approx 1.10$ and 1.15 (Fig. 3.12 (d) and (e)), the value of $\delta/\tilde{L}$ before and during the interactions with the grid turbulence at $\widetilde{M}_t$ = 0.005 remain the same. In the interaction with the grid turbulence at $\widetilde{M}_t$ = 0.009, $\delta/\tilde{L}$ with $M_{s,\,L\text{-}tSW} \approx 1.10$ and 1.15 were 0.3 and 0.2, respectively, at $L_i/\tilde{L} > 50$. In this case, which involved a strong shock wave, the shock wave front was slightly deformed with the increase in $L_i/\tilde{L}$.

Figure 3.13 shows the plots of $\delta/\tilde{L}$ against the dimensionless interaction time, $t_i/t_0$. The dimensionless time was used in a DNS by Tanaka et al. (Tanaka et al., 2020), in which the numerical setup of the shock–turbulence interaction was close to our experimental system. Specifically, the shock waves propagated through a local isotropic turbulent

region. In the definitions, $t_i$, is the time after the interaction and $t_0$ is the ratio of the integral scale to the velocity fluctuation. $t_0$ is expressed as $\tilde{L}/(M_t a_{GT}/\sqrt{3})$ using the variables in this thesis. Tanaka et al. (2020) showed that the initial growth rate of the root-mean-square value of the local shock wave location in the non-dimensional time follows a similar tendency. We can see this tendency of the shock wave thickness, $\delta/\tilde{L}$, in Fig. 3.13 (b) and (c), where $M_{s,L\text{-}tSW} \approx 1.02$–$1.03$ and $1.05$, respectively. However, under the other conditions, evaluating this tendency was difficult because the shock profile became dissipative for the weak shock case ($M_{s,L\text{-}tSW} \approx 1.01$), and a resolution limit was observed in the stronger shock case ($M_{s,L\text{-}tSW} \approx 1.1$ and $1.15$).

Under all conditions, the projected thickness of the shock wave region increased with the increase in $L_i/\tilde{L}$. The maximum value of $\delta/\tilde{L}$ was approximately 1.5, i.e., the largest deformation of the shock wave in the $x$-direction had the same order as the integral scale of the grid turbulence. The gradient of the projected thickness against the changes in $L_i/\tilde{L}$ differed depending on $M_{s,L\text{-}tSW}$ and $\widetilde{M_t}$. When the shock wave exhibited an undetectable profile, its thickness was difficult to define, and the deviation obtained from the side-view image became large. When the shock wave was continuous on the image even after its interaction with the grid turbulence, the projected thickness of the shock wave had a steeper increase with the increase in the turbulent Mach number. The shock Mach number contributed to the robustness of the shock wave against the turbulence. In addition, in Fig. 3.12 (b) and (c), the value of $\delta/\tilde{L}$ became saturated when the interaction length increased. Because the planar shock wave attempted to sustain its planar profile by itself when it was deformed (Landau and Lifshitz, 1987), the self-stability appeared to act in the interaction with turbulence. Thus, the saturation of the projected thickness indicated that the self-stability of the shock wave and the disturbance by the velocity fluctuation of

turbulence were balanced. The saturation of the projected thickness occurred because the self-stability of the shock wave and the disturbance by the velocity fluctuation of the turbulence were balanced. In a DNS study by Tanaka et al. (2020), the statistical location of the moving shock wave entering the turbulence region was studied. Their results showed that the root-mean-square value of the local shock wave location gradually increased after the shock wave enters turbulence. When the shock wave propagates to approximately ten times the integral scale of the turbulence, the root-mean-square value of the local shock wave location became saturated. In our results, as shown in Fig. 3.12 (b) and (c), approximately 20–50 times of the integral scale were required for the projected thickness to saturate and for this value to have the same order as the DNS result. Moreover, a similar tendency in the initial growth of $\delta/\tilde{L}$ after interaction was obtained (Fig. 3.13 (b) and (c)). Therefore, the similarity between the experiment and the DNS was confirmed.

## 3.4 Summary of this chapter

In this chapter, the study on an interaction of a planar shock wave with a grid turbulence was conducted using a CD-ST. Three parameters—shock Mach number $M_s$, turbulent Mach number $M_t$, and interaction length $L_i$—were independently controlled, and their effects were evaluated.

In the grid turbulence formed in a post-shock flow, a temperature variation was observed with a height of approximately 20 mm from the wall in a shock tube with cross-section of 120 mm × 120 mm. A nearly uniform grid turbulence zone of approximately 80 mm × 80 mm was formed in the center of the shock tube. The measured turbulent Mach number was 0.005, 0.009, and 0.014.

We analyzed the edge profile and thickness of a projected image of a planar shock wave interacting with the grid turbulence. When the turbulence was relatively strong, the planar shock wave exhibited a dispersed profile on its interaction with the turbulence. A large shock deformation occurred when the grid turbulence was the strongest ($\widetilde{M}_t$ = 0.014, the tilde represents the value at the visualized position), and the shock wave was the weakest ($M_{s,L\text{-}tSW}$ = 1.01). In the projected shadowgraph and schlieren images in which the interaction length normalized by the integral scale of grid turbulence $L_i/\tilde{L}$ is above 50, the sharp lines of the shock wave vanish entirely. In the interaction with ($M_{s,L\text{-}tSW}$, $\widetilde{M}_t$) = (1.02, 0.014) and (1.01, 0.009), when $L_i/\tilde{L}$ was above 50, the shock wave exhibited an undetectable profile in the image. The undetectable ratio in the image ranged from 0.2–0.5. When the shock wave exhibited an undetectable profile in the image, the relationships between $M_{s,L\text{-}tSW}$ and $\widetilde{M}_t$ satisfied the broken shock criterion, $M_t \geq 0.6(M-1)$, proposed in previous DNS studies (Larsson et al., 2013; Chen and Donzis, 2019). However, in these experiments, $L_i/\tilde{L}$ was significantly affected the shock wave profile. Planar shock waves with a Mach number of 1.05 and higher did not show an undetectable profile when they interacted with the grid turbulence at $\widetilde{M}_t$ examined in this study. When the shock wave was detectable, the projected shock wave thickness increased with the increasing $\widetilde{M}_t$, and saturation of the projected shock wave thickness was seen. We consider that the saturation occurred because the shock wave self-stability and the disturbance by the velocity fluctuation of the turbulence were balanced. Regarding the interaction length, until the projected thickness saturated, a similarity to the recent numerical simulation (Tanaka et al., 2020)) was confirmed.

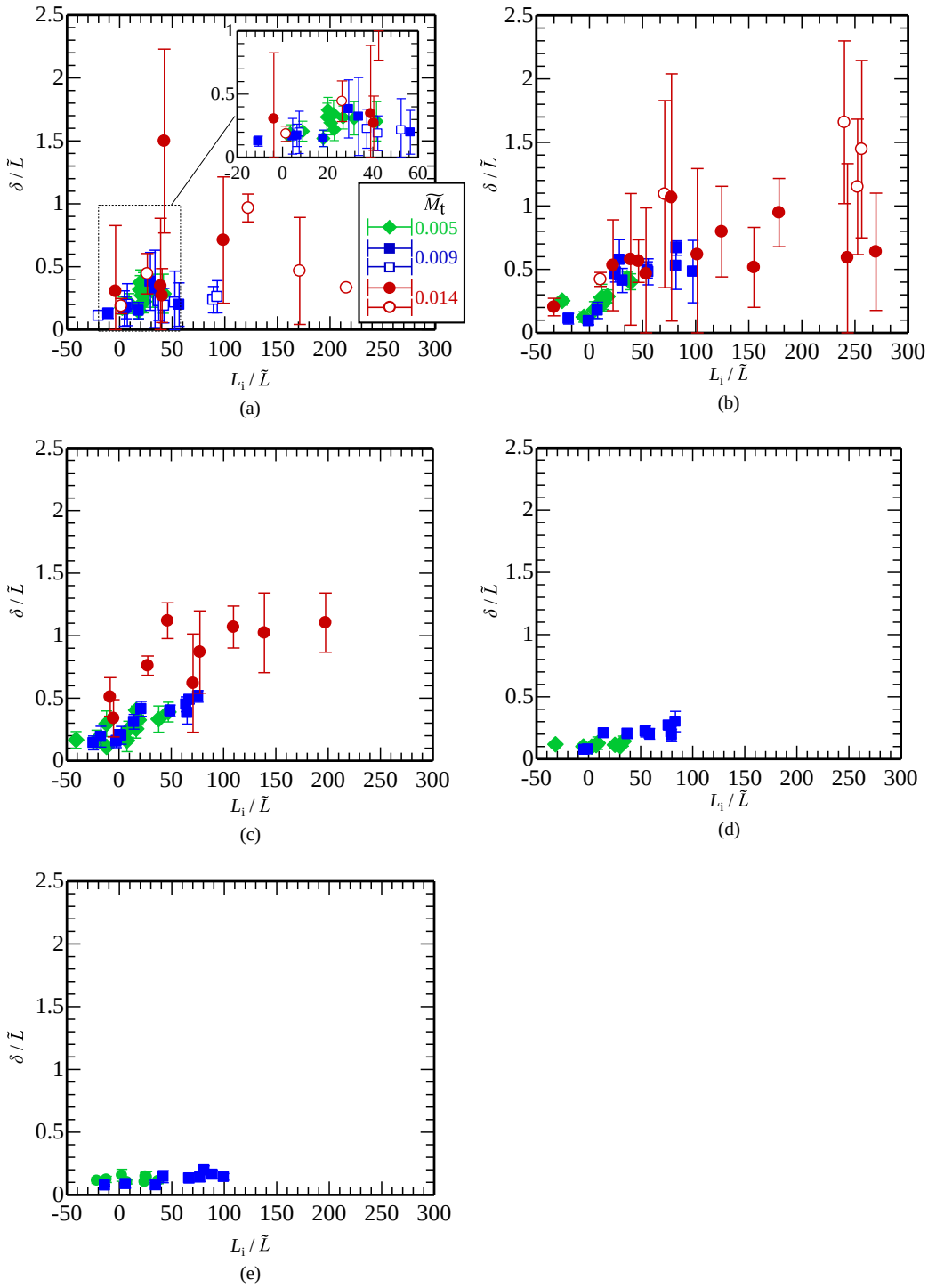


Figure 3.12 $\delta/\tilde{L}$ versus $L_i/\tilde{L}$ for (a) $M_{s,L\text{-}tSW} \approx 1.01$, (b) $M_{s,L\text{-}tSW} \approx 1.02$–$1.03$, (c) $M_{s,L\text{-}tSW} \approx 1.05$, (d) $M_{s,L\text{-}tSW} \approx 1.10$, and (e) $M_{s,L\text{-}tSW} \approx 1.15$. Close symbols: results calculated using shadowgraph image. Open symbols: results calculated using schlieren image.

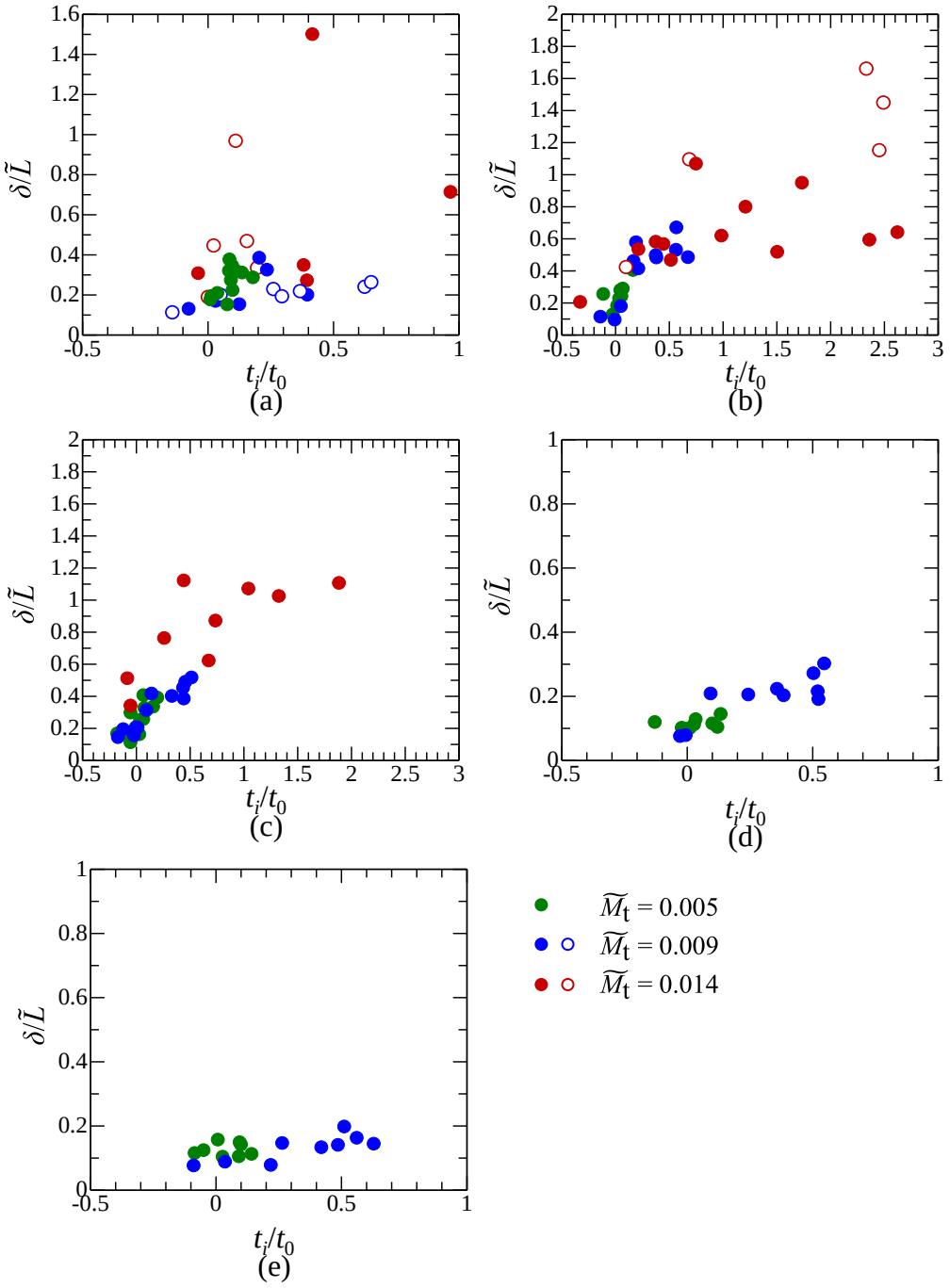


Figure 3.13 $\delta/\tilde{L}$ versus dimensional interaction time $t_i/t_0$ for (a) $M_{s,L\text{-}tSW} \approx 1.01$, (b) $M_{s,L\text{-}tSW} \approx 1.02$–$1.03$, (c) $M_{s,LtSW} \approx 1.05$, (d) $M_{s,L\text{-}tSW} \approx 1.10$, and (e) $M_{s,L\text{-}tSW} \approx 1.15$. Close symbols: results calculated using the shadowgraph image. Open symbols: results calculated using the schlieren images.

# Chapter 4

# Criterion for losing shock wave front profile by interaction with grid turbulence

## 4.1 Introduction of this chapter

A direct numerical simulation (DNS) has been used to investigate the interaction of a planar shock with isotropic turbulence, and three types of shock wave structures have been reported. The “wrinkled” regime, where deformations occur on the shock wave, is the modest state of the interaction. In the “broken” regime, local holes appear on the shock wave, and a gradual change in quantity is observed through the shock wave (Larrson and Lele, 2009; Larrson et al., 2013). The “vanished” state shows that the location of the shock wave front is difficult to be completely defined (Chen and Donzis, 2019). As a predictor of the broken shock regime, $M_t > 0.6$ ($M - 1$) is reported using DNS data (Larrson et al., 2013) and through a theoretical analysis (Donzis, 2012). Specifically, $M_t$ is the turbulent Mach number, and $M$ is the mean upstream supersonic flow Mach number of the shock wave. Further, Chen and Donzis (2019) confirmed that their theory corresponded with DNS.

In Chapter 3, we confirmed the shock wave deformation (“wrinkled” regime) and the increase of undetectable ratio of the shock wave (“broken” regime) caused by interaction

with grid turbulence in a shock wave propagating system. However, the “vanished” state has not yet been observed experimentally as demonstrated in the DNS (Chen and Donzis, 2019). This chapter aims to experimentally demonstrate the vanished shock regime and propose a criterion for this regime in a shock propagating system.

## 4.2 Experimental verification of vanished shock regime

### 4.2.1 Experimental setup

This experiment was conducted using the CD-ST in a similar setup to that in Chapter 3. The coordinate system is also similar to that in Chapter 3. Figure 4.1 shows an example of an $x$ (space)−$t$ (time) diagram of the CD-ST operation. Each driver generated left- and right-incident shock waves (denoted by L-iSW and R-iSW, respectively). Under specific conditions, we weakened the L-iSW using punched stainless-steel sheets installed at $x$ = 1.0 m. Specifically, R-iSW passed through a square grid and became a grid-past shock wave (i.e., R-gSW). The square grid containing 5 mm × 5 mm square pillars with a mesh size of 25 mm was installed at $x$ = 5.0 m (Fig. 4.1). A uniform flow behind R-iSW was transmitted to the grid turbulence beyond the square grid. After the collision of L-iSW and R-gSW, the transmitted shock waves, L-tSW, and R-tSW propagated in the directions shown in Fig. 4.1. At a specific point, L-tSW entered and interacted with the grid turbulence. We defined the interaction length ($L_\mathrm{i}$) as the distance from the shock waves to the head of the grid turbulence. The value of $L_\mathrm{i}$ was controlled by the time difference $t_\mathrm{delay}$ of each driver’s operation. We visualized the shock wave propagating through the grid turbulence using the schlieren method. The visualization system comprised a high-speed camera (Phantom v1211, Vision Research Inc.; 256×256 pixels, 100 kfps) and

synchronized pulse diode laser (CAVILUX Smart, Cavitar Ltd; wavelength 640 nm, pulse duration 10 ns). This system visualized the shock wave through a pair of BK7 windows (effective diameter of 110 mm) that were installed on the sidewall at 450 mm downstream of the square grid. To capture the weak density changes with high sensitivity, the optical path from the test section to the high-speed camera was approximately 20 m.

The main role of the right driver was to generate grid turbulence behind R-gSW. In this experiment, we used a single condition of the grid turbulence. Hence, the right-driver and driven sections' initial pressure conditions were equal to those under the CD-ST operation. The initially filled gas in the right driver was a mixture of He and atmospheric air supplied from a compressor through a dryer. The fill pressure ratio was He:air = 9:1, and air was used as the driven gas. The initial pressure conditions of the right driver and driven section were $p_{4R}$ = 128.3 kPa and $p_1$ = 12.3 kPa, respectively. The shock wave velocity was measured using the time-of-flight principle. By dividing the shock wave velocity by the speed of sound in the gas in the driven section, the shock Mach numbers of R-iSW and R-gSW were calculated as $M_{s,\,\text{R-iSW}} = 1.82$ and $M_{s,\,\text{R-gSW}} = 1.76$, respectively. Here, we assumed that the gas in the driven section was calorically perfect such that the specific heat capacity was a constant value ($\gamma$ =1.4). The velocity of the grid turbulence mainstream flow was approximately 340 $\text{ms}^{-1}$, as calculated using Rankine-Hugoniot relations. The left driver conditions primarily determined the shock Mach number of the interacting shock wave, that is, $M_{s,\,\text{L-tSW}}$. In this research, we set the left driver pressure to $p_{4L}$ = 18.3 or 20.3 kPa depending on the condition. Further, two types of punched stainless-steel sheets were used to change the shock Mach number. Type A comprised 16 punched stainless-steel sheets with the thickness of 0.8 mm, hole diameter of 1 mm, and a blocking ratio of 82.5%. Type B comprised three punched stainless-steel sheets with the

thickness of 1 mm, hole diameter of 2 mm, and a blocking ratio of 64%. When $p_{4L}$ was 18.3 kPa, we obtained $M_{s,\,L\text{-}tSW}$ = 1.006, 1.034, and 1.046 using types A and B punched stainless-steel sheets and those without the sheets, respectively. When $p_{4L}$ was 20.3 kPa, we obtained $M_{s,\,L\text{-}tSW}$ = 1.013 using type A punched stainless-steel sheets. Here, the shock Mach number of the left-transmitted shock wave, $M_{s,\,L\text{-}tSW}$, was calculated using the solution from the head-on collision of L-iSW and R-gSW.

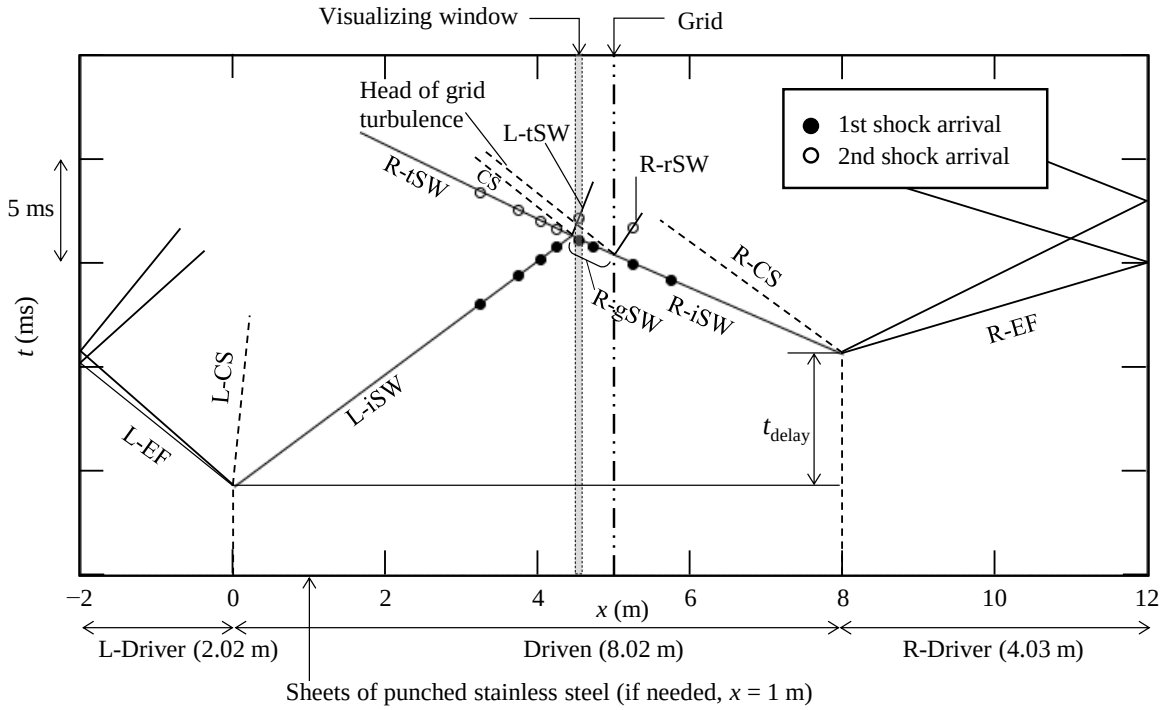


Figure 4.1 Example of an *x*–*t* diagram of the CD-ST operation: $p_{4L}$ = 20.8 kPa, $p_1$ = 12.8 kPa, and $p_{4R}$ = 128.3 kPa. L-, from the left driver; R-, from the right driver; i, incident; t, transmitted; g, grid transmitted; r, reflected from the grid; SW, shock wave; EW, expansion waves; CS, contact surface.

### 4.2.2 Visualization of shock–turbulence interaction

Under the conditions applied in this study, the grid turbulence characteristics could not be measured because a hot-wire probe was broken by finely ruptured cellophane debris. Hence, the turbulent Mach number was estimated using a linear extrapolation from the obtained relationship between the mainstream-flow Mach number of the grid turbulence and turbulent Mach number that was reported in the previous chapter. The near-linear relationship between the mainstream-flow Mach number of the grid turbulence and turbulent Mach number can be observed in the measurement of the grid turbulence that was generated in a shock tube from the mainstream-flow Mach number (0.3–0.7) for a constant mesh size (Briassulis et al., 1998). We applied this linear relationship to our facility. With a mean grid turbulence velocity of 340 $ms^{-1}$ and flow Mach number of 0.72 (calculated using the Rankine-Hugoniot equations in a perfect gas), the representative value of the turbulent Mach number was $\widetilde{M}_t$= 0.025 (tilde represents the value at the center of the visualizing window located at 450 mm downstream of the grid). Because the data used to estimate $\widetilde{M}_t$ were a standard deviation of approximately 10%, the estimated $\widetilde{M}_t$ had a similar degree of error. As the generated grid turbulence was not supersonic flow, strong disturbances such as shock waves generated by the strong velocity fluctuations of turbulence, i.e., shocklets (Lee et al., 1990), could not be confirmed in schlieren images. Pressure oscillation in the grid turbulence, which was induced mainly in the initial diaphragm rupture processes, was 1.7% of the absolute pressure in the grid turbulence based on the pressure measurement using a flush-mounted pressure sensor in the inner wall of the shock tube. This pressure oscillation caused a 1.3% change in the speed of sound.

The schlieren visualization results of the shock wave moving from the left to right

against the grid turbulence blowing from the right to left are shown in Fig. 4.2. To enhance the signal-to-noise ratio in the images, all the images presented in this paper are differential images formed by subtracting the quiescent-state image before the shock tube operation from the rough image (Kim et al., 2010). As also shown in the figure, the shock tube center of approximately 86 mm range is extracted. The positive and negative values of $L_i$ correspond to the interaction lengths during and before the interaction, respectively. The image sequences presented in each row were extracted from the same CD-ST operations. The image sequence in the lower row corresponds to the trial in the long-interaction-length case. Regarding the interaction of the weakest-shock wave case of $M_{s,\,\text{L-tSW}} = 1.006$ (Fig. 4.2 (a)), the shock wave was perfectly planar before interacting with grid turbulence ($L_i < 0$). After the interaction, the shock wave contrast on the visualized image gradually diminished with an increase in the interaction length. At $L_i > 200$ mm, the shock wave profile was not detected on the schlieren images. Finally, the contrast level of the shock wave became equivalent to the density changes caused by the grid turbulence. A similar result was observed in the case of $M_{s,\,\text{L-tSW}} = 1.013$ (Fig. 4.2 (b)). When $L_i$ exceeded 300 mm, we did not observe the shock wave profile. Because the schlieren visualization integrates information from a spanwise direction, a sharp line would be visible if the shock wave remains locally. Hence, for $L_i > 300$ mm, the shock wave appeared to lose its discontinuous profile because of its interactions with the grid turbulence. Regarding this shock wave behavior, Chen and Donzis recently reported on the “vanished” regime of the interaction, wherein the upstream and downstream of the shock wave could not be identified clearly in the DNS results (Chen and Donzis, 2019). A similar result was observed during our experiment. However, we found novel insight during the experiment when moving the shock wave. The shock wave gradually vanished

with an increase in the interaction length. Contrarily to the case of weak shock wave, the relatively strong shock waves with $M_{s,\,\text{L-tSW}}$ = 1.034 and 1.046 (Figs. 4.2 (c) and (d), respectively) were largely deformed. With expansions in the side projected areas with a grid turbulence, the shock wave profiles remained under the long interaction length cases, that is, $L_i$ > 200 mm.

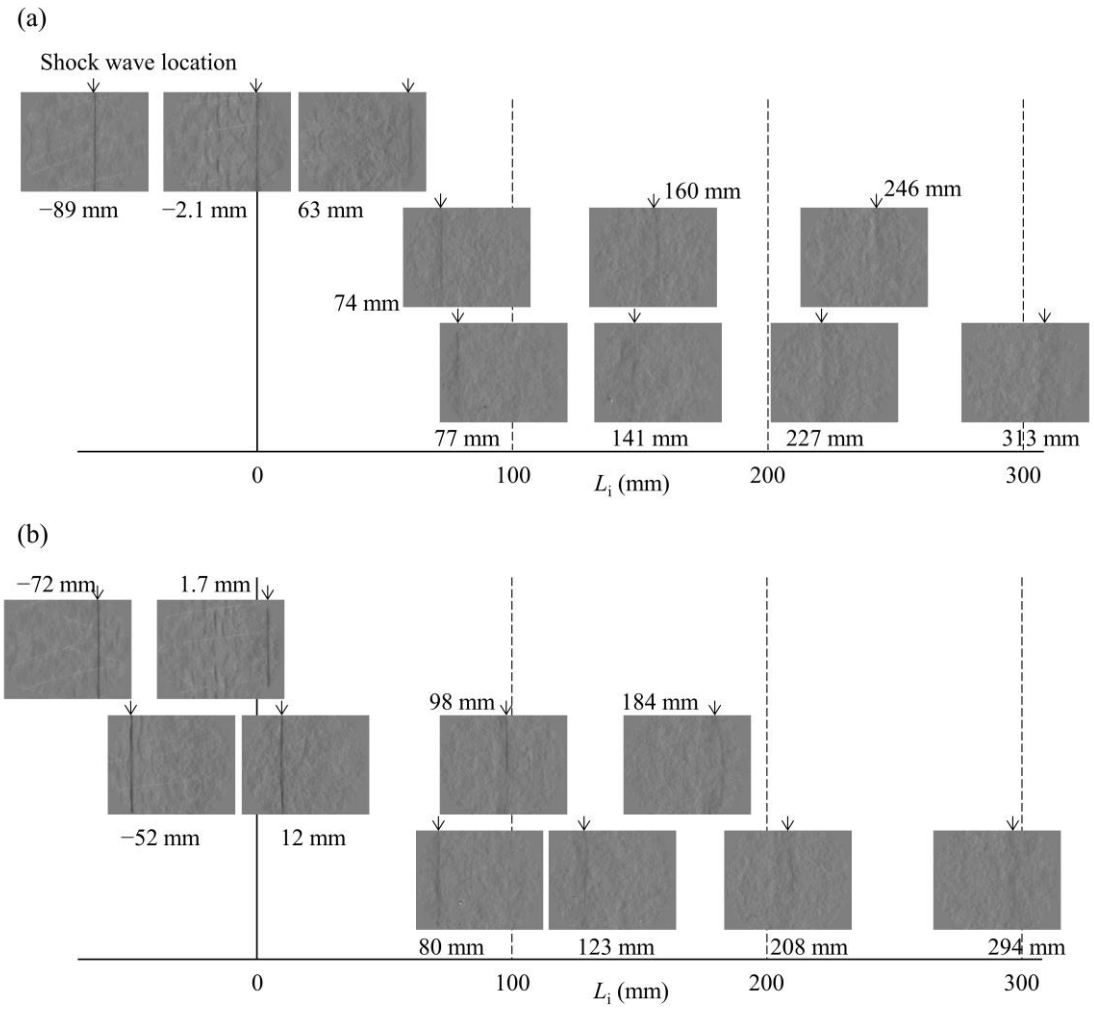


Figure 4.2 Schlieren images of the shock wave propagating through the grid turbulence. Arrows indicate the trajectory of the shock wave propagating at a constant velocity: (a) $M_{s,\,\text{L-tSW}} = 1.006$, (b) $M_{s,\,\text{L-tSW}} = 1.013$, (c) $M_{s,\,\text{L-tSW}} = 1.034$, (d) $M_{s,\,\text{L-tSW}} = 1.046$.

(c)

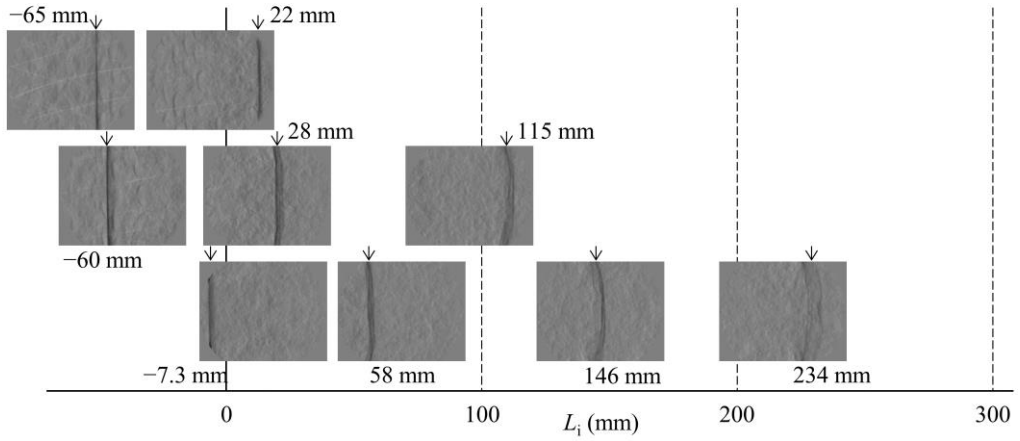


(d)

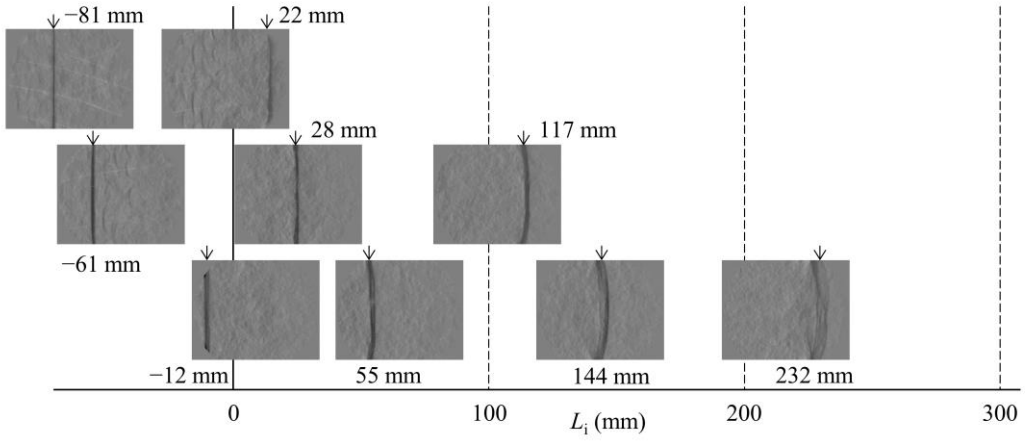


Figure 4.2 (Continued)

## 4.3 Criteria for losing shock wave front profile

### 4.3.1 Shock-forward-induced flow interaction

To physically interpret the shock wave profile vanishment during the turbulence interaction, we used the shock wave modulation based on a one-dimensional (1D) unsteady interaction problem called the Riemann problem (Shapiro, 1953; Liepmann and Roshko, 1957; Glass and Sislian, 1994; Sasoh, 2020). As shown in Fig. 4.3, the most fundamental situation was considered, that is, a shock wave propagating in a quiescent state with a shock Mach number of $M_s$ interacting with a forward induced flow. States 0, L, and R correspond to the quiescent state, area behind the incident shock wave, and forward induced flow, respectively. Here, states 0 and R are assumed to have a similar pressure. Additionally, we assumed that the proprieties of states 0 and R changed occasionally. The gas in all the states were calorically perfect, that is, the specific heat ratio was constant ($\gamma$ =1.4). When the induced shock wave entered state R, new right- and left-running waves were generated. The states after passing the left- and right-running waves are $L^*$ and $R^*$, respectively. The contact surface separates states $L^*$ and $R^*$. A schematic of the $u$ (velocity)−$p$ (pressure) interaction is shown in Fig. 4.4. When the induced velocity direction had a similar direction as the shock wave propagation, the increase in pressure by the right-running wave (curve R→$R^*$) grew smaller than that by the incident (curve 0→L). In this case, left-running expansion waves were generated.

Under such condition, the pressure increase induced by the right-running wave is zero. In this case, the incident shock wave transits to a sound wave by interacting with the forward induced flow. When quantity changes do not occur with the right running wave, the following equations for pressure $p$ and velocity $u$ are obtained:

$$p_{R*} = p_R,$$
$$u_{R*} = u_R. \tag{4.1}$$

Because the left-running wave comprises expansion waves (Fig. 4.3), the following isentropic equation between states L and L* is obtained:

$$\frac{u_{L*} - u_L}{a_L} = \frac{2}{\gamma - 1}\left[1 - \left(\frac{p_{L*}}{p_L}\right)^{\frac{\gamma-1}{2\gamma}}\right]. \tag{4.2}$$

Here, $a_L$ is the speed of sound in the state L. The pressure and velocity across the contact surface between states L* and R* were equal. Thus, we obtained:

$$p_{L*} = p_{R*},$$
$$u_{L*} = u_{R*}. \tag{4.3}$$

By deleting the variables of states L* and R* using Eqs. (4.1)–(4.3) and expressing the variable state L using the incident shock Mach number $M_s$, we obtained the ratio of the velocity of the forward induced flow $u_R$ to the velocity behind the incident shock wave $u_L$ as a function of $M_s$ as follows:

$$\frac{u_R}{u_L} = 1 + \frac{\left(2\gamma M_s^2 - \gamma + 1\right)^{\frac{1}{2}}\left[(\gamma - 1)M_s^2 + 2\right]^{\frac{1}{2}}}{(\gamma - 1)\left(M_s^2 - 1\right)}\left[1 - \left(\frac{2\gamma M_s^2 - \gamma + 1}{\gamma + 1}\right)^{-\frac{\gamma-1}{2\gamma}}\right]. \tag{4.4}$$

The right side of Eq. (4.4) becomes 2 at the limit of the weak shock wave of $M_s \to 1$, and the relationship $|u_R/u_L - 2| < 0.005$ holds for values of $M_s$ from 1 to 2. Hence, $u_R/u_L = 2$ was the weak shock wave. The values of $u_R$ and $u_L$ can be expressed as dimensionless Mach numbers as follows:

$$\frac{u_R}{a_0} = M_R,$$
$$\frac{u_L}{a_0} = \frac{2}{\gamma + 1}\left(\frac{M_s^2 - 1}{M_s}\right), \tag{4.5}$$

where $M_R$ is the flow Mach number of the forward induced flow and $a_0$ is the speed of

sound in the state 0. Using Eq. (4.5), we can express the relationship $u_R/u_L = 2$ with dimensionless Mach numbers, $M_R$ and $M_s$. The following inequality shows the relationship between the shock wave transition and a sound wave or expansion wave when the shock wave interacts with the forward induced flow in a 1D system:

$$M_R \geq \frac{4}{\gamma + 1}\frac{{M_s}^2 - 1}{M_s}. \tag{4.6}$$

Here, let $M_{R,v}$ be the values on the left side, particularly when the equal sign of the above inequality holds.

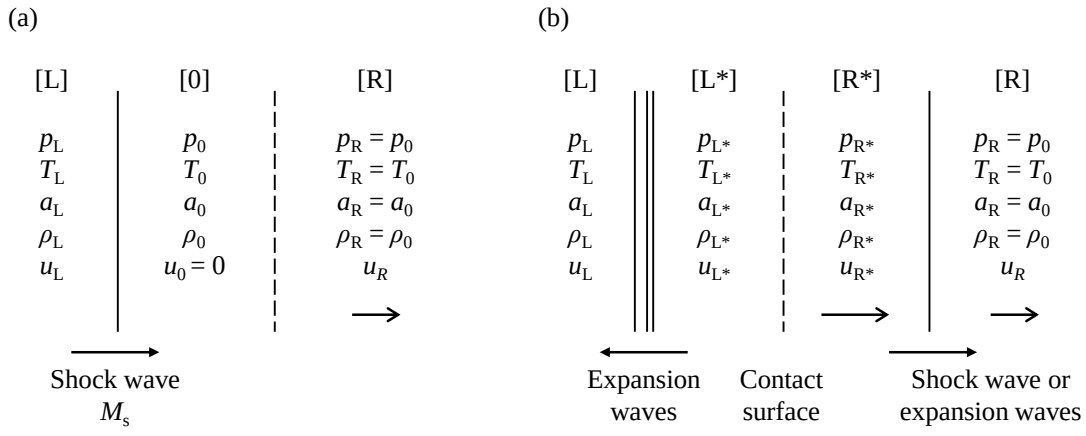


Figure 4.3 Schematics of the 1D shock wave-forward induced-flow interaction: (a) before and (b) after.

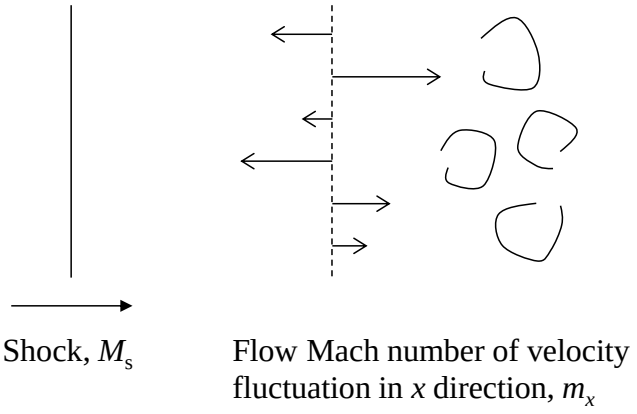


Figure 4.4 Schematic of $x$-element during the shock wave-turbulence interaction.

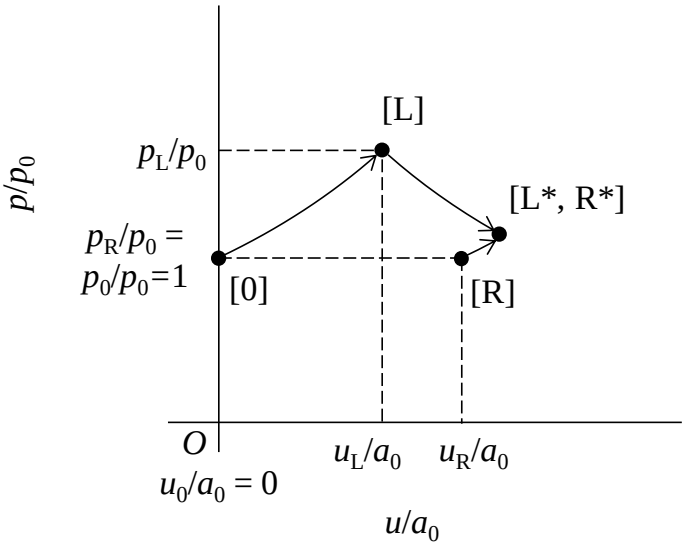


Figure 4.5 Schematic of the $u$–$p$ diagram.

### 4.3.2 Condition for losing shock wave front during interaction with isotropic turbulence

The shock wave state that interacted with the turbulence was considered using a similar analysis proposed by Donzis (2012). In his analysis, the possibility of having a local Mach number less than unity in certain locations corresponded with that of the appearance of continuous changes in fluid properties on the shock wave, as confirmed by the DNS results (Larsson et al., 2013; Chen and Donzis, 2019). In this study, the interaction between a moving shock wave and planar distributed velocity fluctuations was considered (Fig. 4.5). Thus, we calculated the probability of having a local flow Mach number which satisfied Eq. (4.6) in some locations as the probability of the local vanishment of the shock wave. Here, it was assumed that only the velocity was disturbed. Additionally, only the elements facing the shock wave ($x$-direction) were considered. The turbulence velocity fluctuation was assumed to obey a Gaussian distribution, which was a good approximation (Donzis, 2012). We confirmed the grid generated turbulence mean velocity as 160 m/s (Appendix B). Where the Mach number of the "local" turbulence velocity fluctuation $m_x = u_x/a_t$ exceeded the flow Mach number $M_{R,v}$ (thus satisfying Eq. (4.6)), the incident shock wave vanished locally. Here, $u_x$ is the $x$ component of the velocity fluctuation and $a_t$ the speed of sound of the turbulence. The probability of the existence of a local flow satisfying Eq. (4.6) in the turbulence was defined as $P\,(m_x > M_{R,v})$, where $P()$ is a function of probability of the satisfying inequality in (). Regarding the Gaussian-distribution velocity fluctuation, the value of $P\,(m_x > M_{R,v})$ can be statistically expressed in a simple form using the error function erf() as $P\,(m_x > M_{R,v}) = 1 - 1/2\{1+\mathrm{erf}[M_{R,v}/(\sqrt{2/3}M_t)]\}$. Here, regarding the turbulent Mach number, $M_t =$

$\sqrt{3}u'/a_t$ was applied because the turbulence was assumed to be isotropic, where $u$' is the root-mean-square value of $u_x$. Here, we define the probability of the local shock wave vanishment for one-time interaction of the shock wave with a fluctuating-velocity plane as $P_1$. By substituting $M_{R,v}$, $P_1$ is a function of the shock Mach number $M_s$ and turbulent Mach number $M_t$ as expressed below:

$$P_1 = P\left(m_x > M_{R,v}\right) = 1 - \frac{1}{2}\left[1 + \mathrm{erf}\left(\frac{\frac{M_s^2 - 1}{M_s}}{\sqrt{\frac{2}{3}}\ \frac{\gamma + 1}{4} M_t}\right)\right]. \tag{4.7}$$

Figure 4.6 shows a plot of Eq. (4.7) as a function of $M_sM_t / (M_s^2 - 1)$. The four plotted points correspond to the experimental conditions examined in this study. The value of $P$ ($m_x > M_{R,v}$) was almost 0 when $M_sM_t / (M_s^2 - 1) < 1$. At $M_sM_t / (M_s^2 - 1) = 1$, that of $P$ ($m_x > M_{R,v}$) was 0.002, and $P$ ($m_x > M_{R,v}$) increased with $M_sM_t / (M_s^2 - 1) = 1$ as the threshold value. Hence, we obtained the following inequality for the apparition of a shock wave local vanishment during one-time interaction with the fluctuating-velocity plane as expressed below:

$$M_t \geq \frac{M_s^2 - 1}{M_s}. \tag{4.8}$$

Inequality Eq. (4.8) is the criterion for the occurrence of local shock wave vanishment during an interaction of a shock wave with a fluctuating-velocity plane. However, such a case is rare in real situations, wherein shock waves repetitively interact with velocity fluctuations during propagation through turbulent regions of certain volumes. Thus, we considered the repetitive interaction effect on the vanishment of weak shock wave. In a repetitive interaction with velocity fluctuations, the shock wave constantly experienced modulation during propagation. Because quantity change caused by weak shock waves were regarded as isentropic (Shapiro, 1953a; Liepmann and Roshko, 1957; Glass and

Sislian, 1994; Sasoh, 2020), the flow Mach number that caused the vanishment of the shock wave was determined only by the shock Mach number of the incident shock wave. The shock wave vanishment condition in Eq. (4.6) did not change during the interaction. Hence, we can conclude that the shock wave locally vanished when it met the flow, thereby satisfying Eq. (4.6) during propagation in turbulence.

Additionally, we must consider the shock wave behavior after vanishment, which is discussed below. After the shock wave locally vanishes, compression waves are formed by multidimensional effects surrounding the vanished area. Hence, the recovery state of the shock wave from the compression waves is important in modeling the behavior of the shock wave propagating through turbulence. We quantitatively analyzed the shock wave reformation under experimental conditions similar to those in a 1D analysis as presented by Sasoh (Sasoh, 2020). Here, we considered the bundle of compression waves wherein its leading head initially ($t = 0$) was located at $x_a$ and the tail at $x_b$ (Fig. 4.7). We assumed that the pressure variation between $x_a$ and $x_b$ was continuous. The thickness of the bundle was $\Delta x_c = x_a - x_b$. Because the local velocity of the characteristic increased with increasing pressure, the tail compression wave gradually reached the head compression wave at $t = t_s$, thus forming a shock wave. We defined the shock formation location as $x = x_s$, and the shock formation distance $L_s$ as $L_s = x_s - x_a$. The time of shock formation $t_s$ is written using the velocities of the characteristics at $x_a$ and $x_b$ as well as $c_{+,a}$ and $c_{+,b}$ as follows:

$$t_s = \frac{L_s}{c_{+,\,a}} = \frac{L_s + \Delta x_c}{c_{+,\,b}}. \tag{4.9}$$

This equation can be rewritten as

$$\frac{L_s}{\Delta x_c} = \frac{c_{+,\,a}}{c_{+,\,b} - c_{+,\,a}}, \tag{4.10}$$

where $c_{+,a}$ and $c_{+,b}$ are written using the flow velocity $u$ and speed of sound of the flow $a$

as

$$c_{+,\,a} = u_a + a_a, \quad c_{+,\,b} = u_b + a_b. \tag{4.11}$$

Using Eqs. (4.9)–(4.11), we estimated the shock reformation distance after the weak shock wave became compression waves with a thickness of $\Delta x_c$. With the determined values of $u_a$ and $a_a$, the values of $u_b$ and $a_b$ were calculated using the isentropic relationship for a specific pressure jump. Because properties that change owing to weak shock waves can be regarded as isentropic, the pressure jump across compression waves was regarded similar as that across the weak shock wave. Thus, $L_s/\Delta x_c$ was calculated for a given shock Mach number $M_s$, as shown in Fig. 4.8. We used the value of $u_a = -340$ m/s and $a_a = 478$ m/s, which were under similar conditions as those in the experiment. The value of $L_s/\Delta x_c$ decreased with an increase in $M_s$. This is because $c_{+,\,b}$ became large for strong compression waves. This behavior shows that the weak shock wave required a longer shock formation distance than the strong shock did. The value of $L_s/\Delta x_c$ was 23 for $M_{s,\,\text{L-tSW}} = 1.006$. This calculation shows that if the shock wave of $M_{s,\,\text{L-tSW}} = 1.006$ transforms into compression waves of thicknesses which are equivalent to the integral scale of the turbulence, a propagation length of approximately ten times more than the integral scale is needed to recover the shock profile. Contrarily, the shock waves of $M_{s,\,\text{L-tSW}} = 1.034$ and 1.046 required propagation distances of 4.3 and 3.2 times $\Delta x_c$, respectively. In these relatively strong shock wave cases, the local compression waves soon reformed as the shock wave. Hence, the assumption that the vanished parts of the shock wave were not recovered during the interaction was appropriate for the very weak shock waves, such as those satisfying $L_s/\Delta x_c \geq O(10^1)$. For simplicity, we assumed that the shock waves of $M_s = 1.006$ and 1.013 did not recover once they experienced discontinuous profile loss.

Based on the above assumptions, the vanishment of the weak shock waves $M_{s,\,L\text{-}tSW}$ = 1.006 and 1.013 is modeled considering the interaction length effect. In a repetitive interaction with the velocity fluctuation, we define the probability of the local shock wave vanishment over $n$ interactions as $P_n$. In $n$+1 interactions, $P_{n+1}$ is expressed as the sum of the following independent cases: (1) The local shock wave remains after $n$ interactions and later vanishes after $n$+1 interactions, and (2) the local shock wave had already vanished during interactions 1 to $n$. The probability of the former was $P(m_x > M_{R,\,v})$ $(1 - P_n)$ after considering the conditional probability, and that of the latter was $P_n$. Hence, we obtained $P_{n+1}$ in the recurrence formula as $P_{n+1} = P\,(m_x > M_{R,\,v})\,(1 - P_n) + P_n$. Here, the first term of $P_n$ satisfied the relationship of $P_1 = P\,(m_x > M_{R,\,v})$, as expressed in Eq. (4.7). The general term of $P_n$ can be derived in the geometric progression form as

$$P_n = 1 - [1 - P\,(m_x > M_{R,\,v})]^n. \tag{4.12}$$

Conversely, for the relatively strong shock waves with $M_{s,\,L\text{-}SW}$ = 1.034 and 1.046, $P_n$ was approximately 0 because the shock wave vanishment criterion in Eq. (4.8) was not satisfied (Fig. 4.6). Further, the shock wave was reformed using the profile of the compression waves (Fig. 4.8).

The gradual shock wave vanishment phenomenon with an increased interaction length observed during the experiment was considered physically using the developed model. We assumed that the integral length scale of the turbulence represented the length of one velocity fluctuation because the integral scale of the turbulence physically corresponded to the length of the dominant scale eddies in a turbulent flow. During the previous measurement of the grid turbulence in the CD-ST, the integral scale of the grid turbulence was approximately 10 mm for the mean flow of 50–160 m/s (see Chapter 3). In this

analysis, we adopted this value as the integral scale of the grid turbulence. Hence, the interaction length consumed by one-time interaction with velocity fluctuations was 10 mm in this model. In the experiment results, because the largest value of the interaction length was approximately 300 mm, we visualized an interaction length that was 30 times that of the shock wave with the velocity fluctuation in this study. The value of $P_n$ was plotted as a function of the number of interactions $n$ (Fig. 4.9). The interaction length $L_i$ for the integral scale of 10 mm was also shown on the horizontal axis. Four types of plots corresponded to the experimental conditions. With an increase in $L_i$, $P_n$ sharply increased in the weakest shock Mach number of $M_{s,\,\text{L-tSW}} = 1.006$. The vanishment probability exceeded 80% for $L_i = 200$ mm. The calculations from this model were consistent with the experimental results: The contrast corresponded to density changes by the shock wave in the visualized image decreased with increasing interaction length. The model corresponded with the experimental results of the total shock wave vanishment at approximately $L_i = 200$ mm. Furthermore, in the cases of relatively strong shock waves of $M_{s,\,\text{L-SW}} = 1.034$ and 1.046, the shock wave vanishment probabilities remained near zero. The proposed shock wave vanishment model also corresponded with the experimental results of the continuous shock wave profile on the side-view image. However, on the border condition $M_{s,\,\text{L-SW}} = 1.013$, the model did not quantitatively describe the experimental results. The model showed a 4% vanishment on a shock wave profile at $L_i = 300$ mm, while the experiment showed a complete shock wave vanishment at approximately $L_i = 300$ mm.

Following the comparison of the experimental results, a precise correspondence was not achieved when the shock Mach number and turbulent Mach number satisfied the shock wave vanishment criteria ($M_{s,\,\text{L-SW}} = 1.013$, $\widetilde{M}_t = 0.025$). Conversely, the proposed

shock wave vanishment model, based on the solution of the 1D unsteady compression problem, can explain the weak shock wave vanishment in the interaction length range of 10 times more than the integral scale of grid turbulence.

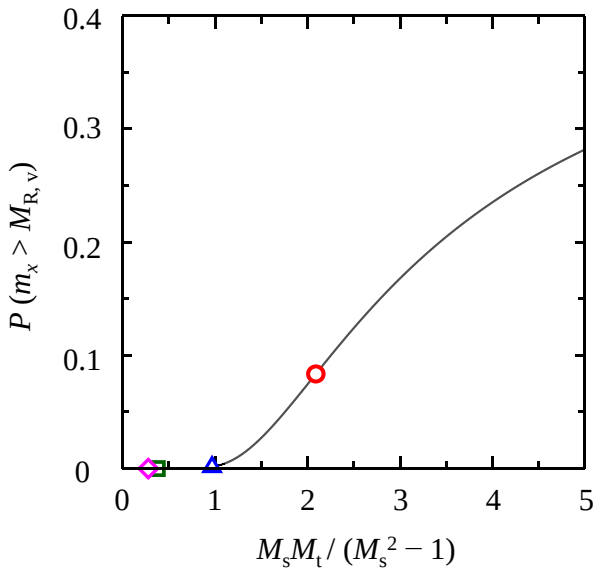


Figure 4.6 Shock vanishment probability after one-time interaction $P\ (m_x > M_{R,v})$ as a function of $M_s M_t / (M_s^2 - 1)$. Plots correspond to $M_{s,\text{L-tSW}} = 1.006$ (circle), $M_{s,\text{L-tSW}} = 1.013$ (triangle), $M_{s,\text{L-tSW}} = 1.034$ (square), and $M_{s,\text{L-tSW}} = 1.046$ (diamond), respectively. $M_t = 0.025$ under all conditions.

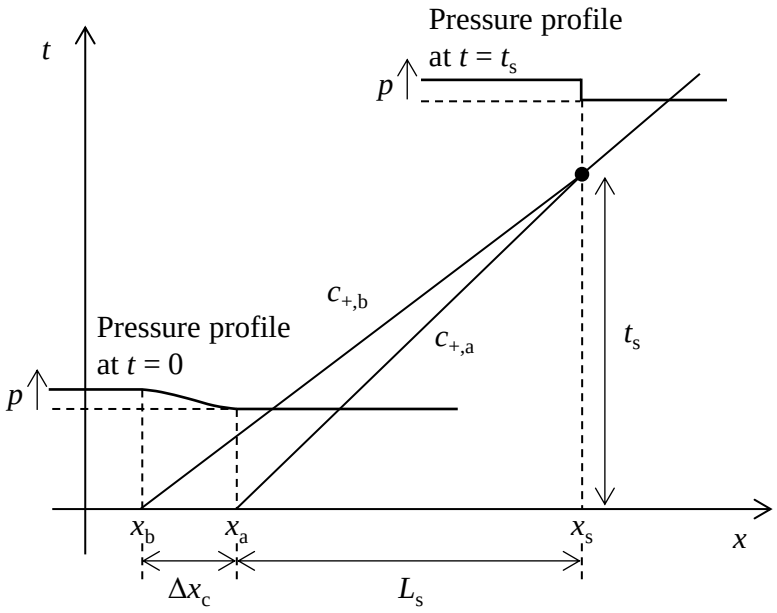


Figure 4.7 Schematic of shock formation by the integration of compression waves, as presented by Sasoh (2020).

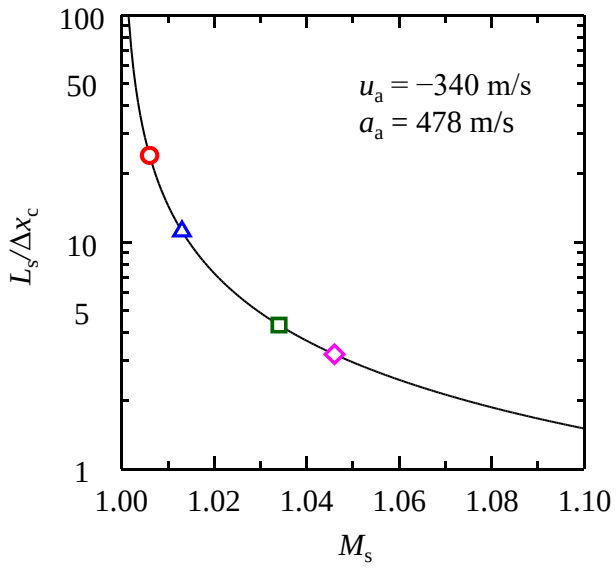


Figure 4.8 Ratio of shock formation distance to thickness of compression wave $L_s/\Delta x_c$ as a function of $M_s$. Plots correspond to the shock Mach numbers examined during the experiment.

## 4.4 Summary of this chapter

This chapter experimentally and theoretically investigates losing the shock wave front profile during interactions with turbulence. We experimentally demonstrated the vanishing of a weak shock wave profile during interactions with grid turbulence using the CD-ST. On the side-projected schlieren images, the weak shock wave contrast gradually decreased with an increase in the interaction length. Under the weak shock wave conditions ($M_{s,\,\text{L-SW}}$ = 1.006 and 1.013), the vanishing regime was confirmed when the interaction length exceeded 200 mm. This phenomenon was modeled based on a 1D unsteady shock interaction theory (the Riemann problem). During the 1D interaction of the shock wave with a forward induced flow, the shock wave transformed into a sound wave and even an expansion wave. We extended the theory to a shock wave interaction with a planar distributed velocity fluctuation and derived a criterion $M_t \geq (M_s^2 - 1)/M_s$ for the vanished regime, where $M_s$ is the shock Mach number and $M_t$ the turbulent Mach number. The effect of the interaction length during the experiment was considered in the proposed shock wave vanishment model by a repetitive interaction with the velocity fluctuation. Regarding the quantitative analysis of the characteristic propagation in the measured interaction range, we discovered that the weak shock wave did not recover once it experienced discontinuous profile loss. Although a precise correspondence was not confirmed for conditions wherein the shock and turbulent Mach numbers began to satisfy the shock wave vanishment criterion, we confirmed the validity of the proposed model for the vanishment of weak shock waves at interaction lengths that were ten times more than the integral scale of the grid turbulence.

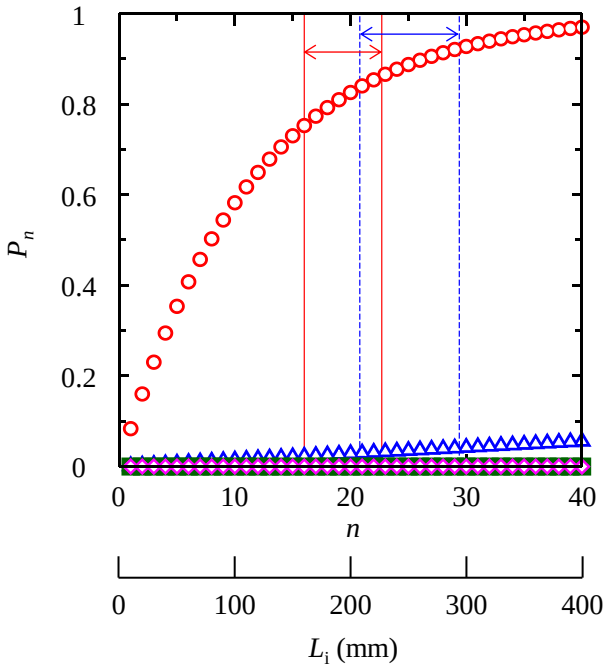


Figure 4.9 Shock vanishment probability in $n$ interactions with the velocity fluctuation. The interaction length for the integral scale of 10 mm is also shown in the horizontal axis. $M_t$ = 0.025 under all conditions and $M_{s,\,L\text{-}tSW}$ = 1.006 (circle), $M_{s,\,L\text{-}tSW}$ = 1.013 (triangle), $M_{s,\,L\text{-}tSW}$ = 1.034 (square), and $M_{s,\,L\text{-}tSW}$ = 1.046 (diamond). Regions indicated by a double arrow correspond to $L_i$, that is, where in the present experiment the shock wave front profile vanishes based on the schlieren images at $M_{s,\,L\text{-}tSW}$ = 1.006 (solid line) and $M_{s,\,L\text{-}tSW}$ = 1.013 (dashed line).

# Chapter 5 Conclusions

In this thesis, unsteady changes in a planar shock wave front propagating through grid turbulence were investigated. A preliminary experiment to generate weak shock waves was reported in Chapter 2. Accordingly, the modulation and moderation of the shock wave front profile affected by grid turbulence were discussed in Chapters 3 and 4. The outcomes of each chapter are summarized below.

Chapter 2 discusses the relationship between a cellophane diaphragm rupture and formation of the weak shock waves to conduct an interaction experiment between a planar shock wave and grid turbulence. We experimentally obtained a law characterizing the cellophane diaphragm rupture process and minimum stress condition for appropriate shock tube operations. The shock wave formation was completed in the early stage of the cellophane diaphragm opening process owing to the effective acceleration of the fragmented diaphragm petal. This result ensured the generation of a weak shock wave in a counter-driver shock tube, which was used in Chapters 3 and 4.

Chapter 3 discusses the interaction of a planar shock wave with grid turbulence, investigated using a counter-driver shock tube. Three parameters (i.e., shock Mach number $M_s$, turbulent Mach number $M_t$, and interaction length $L_i$) were independently controlled. Hence, their effects on shock wave modulations were evaluated by analyzing the edge profile and thickness of the projected image of the planar shock wave while interacting with grid turbulence. Planar shock waves with a Mach number of 1.05 and higher showed the apparent density change on the shadowgraph and schlieren images. The projected thickness of the shock wave increased with an increase in $\widetilde{M}_t$ (tilde

denotes the representative value at the visualization location). Furthermore, saturation of the projected shock wave thickness was observed. The interaction length before the projected thickness saturation corresponded with the result obtained by a recently conducted numerical simulation using a numerical setup similar to the one considered in this research (Tanaka et al., 2020). This compatibility showed that the shock wave, while propagating through turbulence, had a limited deformation extent depending on the strength of the shock wave and turbulence. Regarding the appearance of extreme shock wave deformation, which was similar to the broken regime, the criteria proposed in previous studies (Donzis, 2012; Larsson et al., 2013; Chen and Dondis, 2019) corresponded with our experimental observations. However, during the experiment, we confirmed that an interaction length of approximately 20–50 times the integral scale of the turbulence was required to observe the broken regime. This is a new finding on the regime of shock–turbulence interactions in a shock wave propagating system.

Chapter 4 discusses the investigation of losing the shock wave front profile during interactions with turbulence experimentally and theoretically. Under weak shock wave conditions ($M_{s,\,\text{L-tSW}}$ = 1.006 and 1.013), when the interaction length exceeded 200 mm, the vanishing regime was confirmed. This phenomenon was modeled based on the 1D unsteady shock interaction theory (Riemann problem). Furthermore, a criterion $M_t \geq (M_s^2 - 1)/M_s$ for the vanished regime was derived. We confirmed the validity of the proposed model regarding the vanished weak shock waves at interaction lengths that were ten times higher than the grid turbulence integral scale.

In conclusion, the outcomes obtained in this thesis based on the objective mentioned in Chapter 1 are summarized as follows. The experiment on shock–turbulence interactions was enabled by clarifying shock formation characteristics in the shock tube.

Then, we experimentally demonstrated “broken” and “vanished” interaction regimes, confirmed in earlier DNS studies, in a shock propagation system. The experimental results of shock–turbulence interactions emphasized the importance of unsteady effects during the modulation and moderation of the shock wave front profile. It was found that a sufficient interaction length is required to obtain the broken and vanished regimes in a shock wave propagation system. Regarding the appearance conditions of these regimes, the “broken” and “vanished” regimes were obtained during the interaction between the weak shock wave and weak turbulence when compared to conditions adopted in the DNS studies. Thus, the experimental results demonstrated that such interaction regimes occurred in reality. Additionally, the criterion $M_t \geq (M_s^2 - 1)/M_s$ for the vanished regime in a shock propagation system was proposed and experimentally validated. These outcomes are advantageous to predicting the sonic boom level on the ground and development of new shock mitigation methods based on interactions between the shock waves and a flow field.

# Appendix A

# Polyester diaphragm opening process

Here, examples of the opening process of polyester-made diaphragm are shown. A shock tube of $D$ = 62 mm was used. The thickness of the polyester diaphragm (DuPont Teijin Film, Melinex® 339) was 36 μm. The polyester diaphragm can handle pressure difference higher than the cellophane diaphragm. Natural bursting occurred around $\Delta p_{41}$ = 100 kPa.

Figure A.1 shows the opening of the polyester diaphragm when $p_4$ = 201.5 kPa and $p_1$ = 101.5 kPa. At $t$ = 160 μs, a single crack was generated from the point pierced by a needle. At $t$ = 320 μs, the crack arrived at the shock tube wall. Subsequently, the diaphragm was teared by the high-pressure gas in the driver. This polyester diaphragm opening process was different from that of the cellophane diaphragm, which has the high-speed multiple crack propagation. This result support that the cellophane diaphragm is quite suitable for the weak shock wave formation.

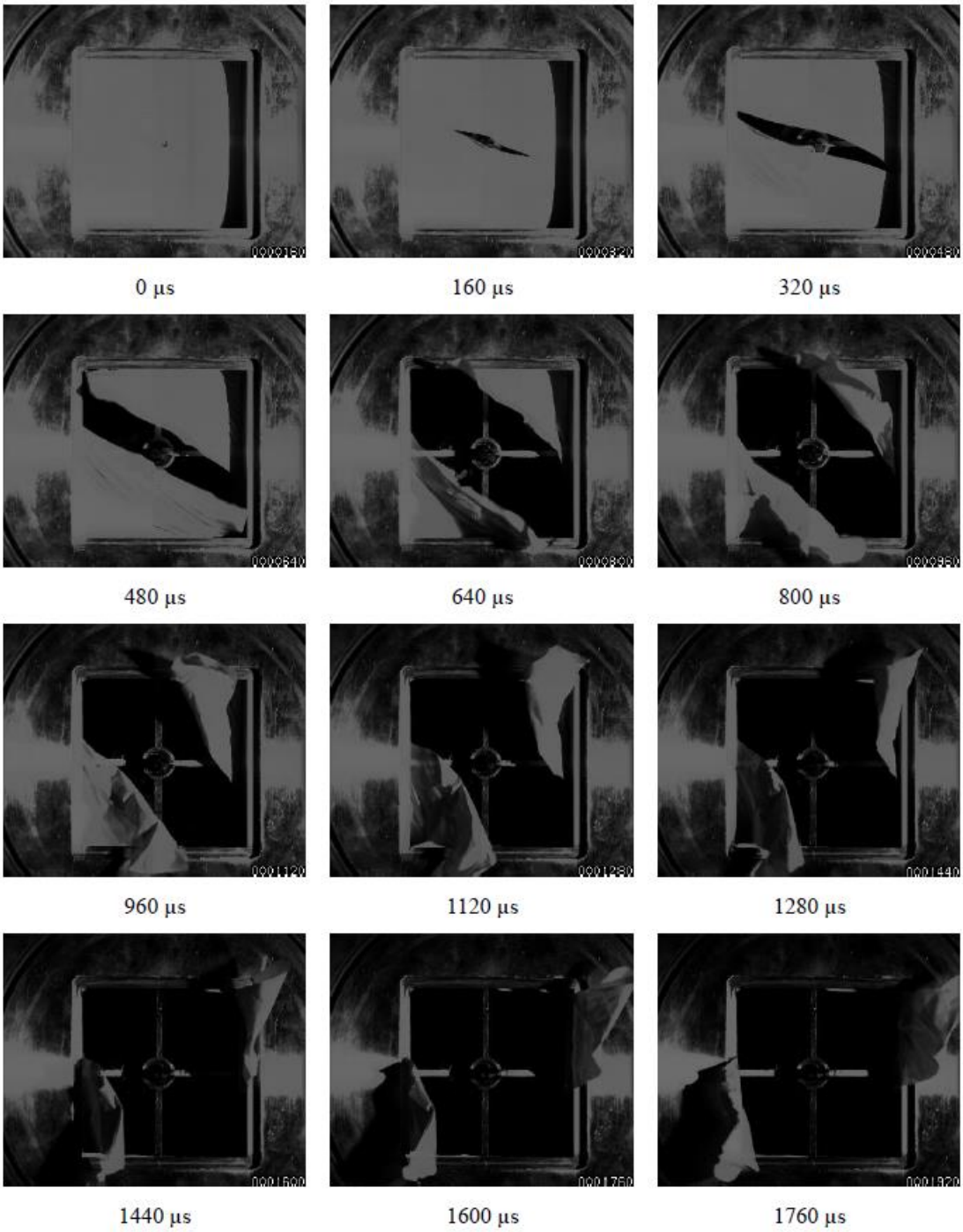


Figure A.1 Opening process of polyester diaphragm at $\Delta p_{41}$ = 100 kPa ($p_4$ = 201.5 kPa and $p_1$ = 101.5 kPa).

# Appendix B

# Response limit of the hot-wire anemometer and distribution of velocity fluctuation of grid turbulence

Here, the response limit of hot-wire anemometer and the velocity distribution of grid turbulence are shown as supplementary data. Figure B.1 is an example of originally measured velocity fluctuation in the grid turbulence. The data was obtained under the condition of $U$ =160 m/s and measured at $\Delta x$ = 0.45 m. The energy distribution of this measured signal is shown in Fig. B.2. The signal has a peak of approximately 7-10 kHz. The signal becomes small after the peak and takes the minimum value at approximately 20-30 kHz, and is noisy at higher frequency regions. Therefore, the response limit of the hot wire used in this research is considered approximately 20 kHz. The turbulent Mach number $M_t$ and other quantities of the grid turbulence are obtained at the low-pass filtered signal of velocity fluctuation (≤ 20 kHz).

Figure B.3 shows the probability density function of the measured data after processing by the low-passed filter. The measured distribution is shown as the black plot in the figure. The gray dotted line shows the Gaussian profile for $\sigma$ = 4.40 m/s. The measured velocity distribution was close to the Gaussian profile.

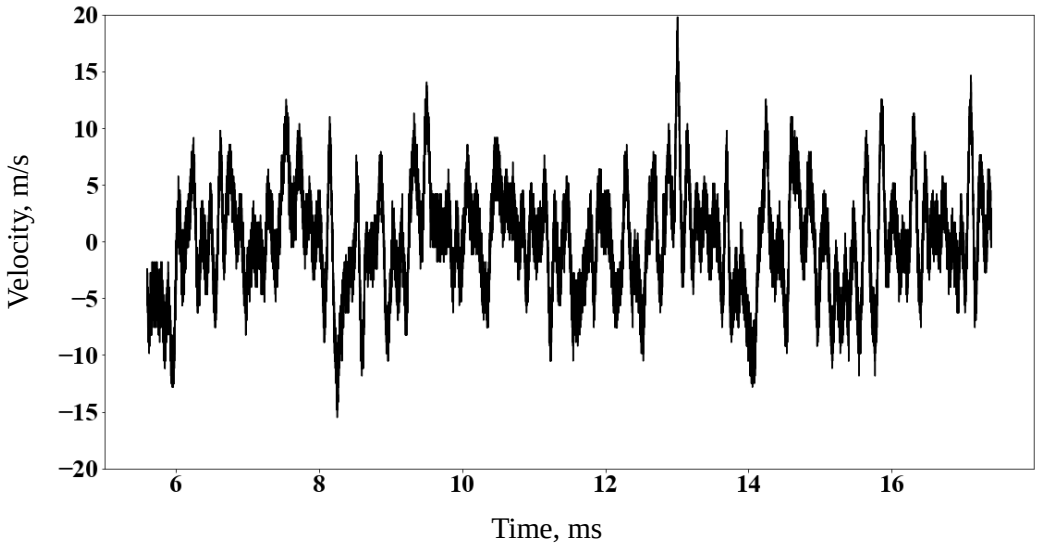


Figure B.1 Example of original velocity fluctuation signal measured by hot-wire anemometer.

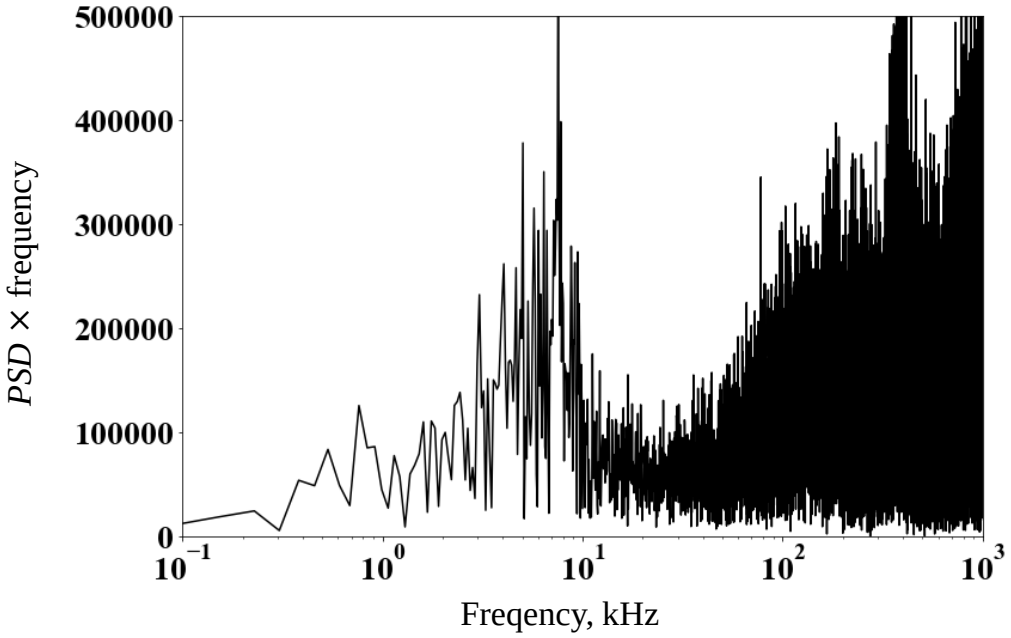


Figure B.2 Energy distribution of measured velocity signal.

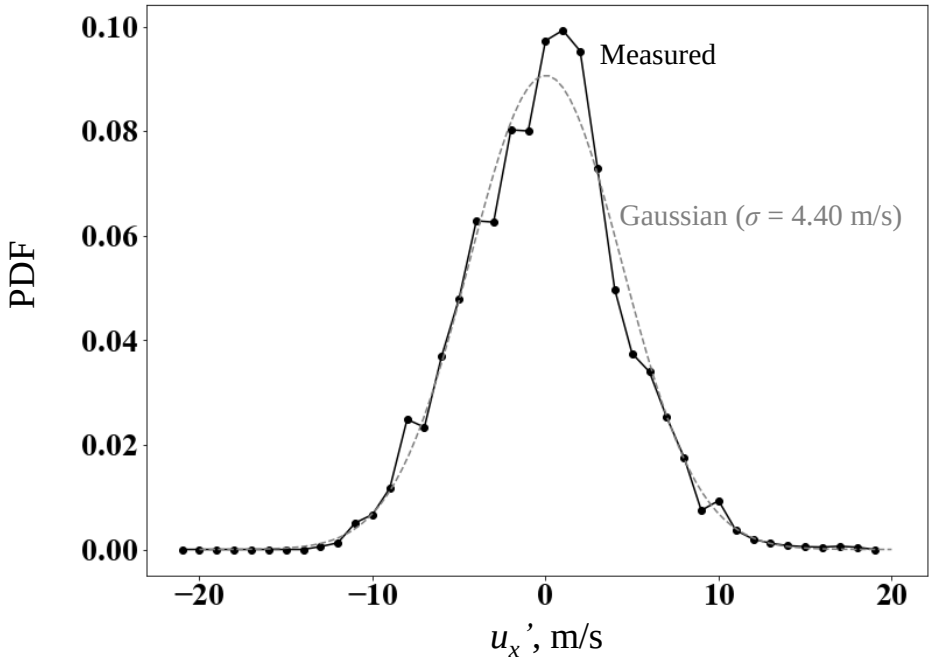


Figure B.3 Example of pdf of measured $u_x$'. Gray dotted line shows Gaussian profile.

# References

Agui, J. H., Buriassulis, G., and Andreopoulos, Y., "Studies of interactions of a propagating shock wave with decaying grid turbulence: velocity and vorticity fields," Journal of Fluid Mechanics, vol. 524, pp. 143–195, 2005.

Andreopoulos, Y., Agui, J. H., and Briassulis, G., "Shock wave-turbulence interaction," Annual Review of Fluid Mechanics, vol. 32, pp. 309–345, 2000.

Barre, S., Alem, D., and Bonnet, P., "Experimental study of a normal shock/Homogeneous turbulence interaction," AIAA Journal, vol 34, No. 5, pp. 968–974, 1996.

Briassulis, G., Agui, J. H., Andreopoulos, J., and Watkins, C. B., "A shock tube research facility for high-resolution measurements of compressible turbulence," Experimental Thermal and Fluid Science, vol, 13, No. 4, pp. 430–446, 1996.

Briassulis, G., Agui, J. H., Watkins, C. B., and Andreopoulos, J., "Studies of shock wave interactions with homogeneous and isotropic turbulence," NASA/CR-1998-206948, 1998

Briassulis, G., Agui, J. H., and Andreopoulos, Y., "The structure of weakly compressible grid-generated turbulence," Journal of Fluid Mechanics, vol. 432, pp. 219–283, 2001.

Britan, A., Igra, O., Ben-Dor, G., and Shapiro, H., "Shock wave attenuation by grids and orifice plates," Shock Waves, vol. 16, pp. 1–15, 2006.

Budzinski, J. M., Zukoski, E. E., and Marble, F. E., "Rayleigh scattering measurements of shock enhanced mixing," AIAA/SAE/ASME/ASEE 28th Joint Propulsion

Conference and Exhibit, AIAA 92-3546, 1992.

Campbell, G. A., Kimber, G. M., and Napier, D. H., “Bursting of diaphragm as related to the operation of shock tubes,” Journal of Scientific Instruments, Vol. 42, pp. 381–384, 1965.

Canny, J., “A Computational Approach to Edge Detection, “IEEE Transactions on Pattern Analysis and Machine Intelligence,” vol. PAMI 8, No. 6, pp. 679–698, 1986.

Chen, C. H. and Donzis, D. A., “Shock–turbulence interactions at high turbulence intensities,” Journal of Fluid Mechanics, vol. 870, pp. 813–847, 2019.

Clemens, N. T. and Narayanaswamy, V., “Low frequency unsteadiness of shock wave/turbulent boundary layer interactions,” Annual Review of Fluid Mechanics, vol. 46, pp. 469–492, 2014.

Curran, E. T., Heiser, W. H., and Pratt, D. T., “Fluid phenomena in scramjet combustion systems,” Annual Review of Fluid Mechanics, vol. 28, pp. 323–360, 1996.

Donzis, D. A., “Shock structure in shock–turbulence interactions,” Physics of Fluids, vol. 24, 126101, 2012.

Dosanjh, D. S., “Interaction of grids with traveling shock waves,” NACA TN3680, 1956.

Ferri, A., “Mixing-controlled supersonic combustion,” Annual Review of Fluid Mechanics, vol. 5, pp. 301–338, 1973.

Futamura Chemical Co. Ltd., Private communication, 2021.

Gaetani, P., Guardone, A., and Persico, G., “Shock tube flows past partially opened diaphragms,” Journal of Fluid Mechanics, vol. 602, pp. 267–286, 2008.

Glass, I. I. and Sislian, J. P., “Nonstationary Flows and Shock Waves,” Clarendon Press, Oxford, 1994.

Henshall, B. D., “On some aspects of the use of shock tubes in aerodynamic research,”

Aeronautical Research Council, Technical Report, Reports and Memoranda, No. 3044, 1955.

Honkan, A. and Andreopoulos, J., “Rapid compression of grid-generated turbulence by a moving shock wave,” Physics of Fluids A: Fluid Dynamics, vol. 4, 2562, 1992.

Houas, L., Biamino, L., Mariani, C., Igra, O., Jourdan, G., and Massol, A., “The effects that changes in the diaphragm aperture have on the resulting shock tube flow,” Shock Waves, vol. 22, pp. 287–293, 2012.

Ikui, T. and Matsuo, K., “Investigation of the aerodynamic characteristics of the shock tubes (part 1, the effects of tube diameter on the tube performance).” Bulletin of the JSME, vol. 12, No. 52, pp. 774–782, 1969.

Ikui, T., Matsuo, K., and Nagai, M., “Investigation of the aerodynamic characteristics of the shock tubes (part 2, on the formation of shock waves),” Bulletin of the JSME, vol. 12, No. 52, pp. 783–792, 1969.

Inokuma, K., Watanabe, T., Nagata, K., Sasoh, A., and Sakai, Y., “Finite response time of shock wave modulation by turbulence,” Physics of Fluids, vol. 29, 051701, 2017.

Inokuma, K., Watanabe, T., Nagata, and Sakai, Y., “Statistics of overpressure fluctuations behind a weak shock wave interacting with turbulence,” Physics of Fluids, vol. 31, 085119, 2019.

Kanamori, T., Takahashi, T., Ishikawa, H., Makino, Y., Naka, Y., and Takahashi, H., “Numerical evaluation of sonic boom deformation due to atmospheric turbulence,” AIAA Journal, vol. 59, No. 3, 2021.

Kane, E. J., “Some effects of the atmosphere on sonic boom,” NASA SP 147, pp. 49–63, 1967.

Keller, J. and Merzkirch, W., “Interaction of a normal shock wave with a compressible

turbulent flow," Experiments in Fluids, vol. 8, pp. 241–248, 1990.

Kim, J.-H., Sasoh, A., and Matsuda, A., "Modulations of a weak shock wave through a turbulent slit jet," Shock Waves, vol. 20, pp. 339–345, 2010.

Kitamura, T., Nagata, K., Sakai, Y., Sasoh, A., Terashima, O., Saito, H., and Harasaki, T., "On invariants in grid turbulence at moderate Reynolds numbers," Journal of Fluid Mechanics, vol. 738, 10, pp. 378–406, 2014.

Landau, L. D. and Lifshitz, E. M., "Theory of Elasticity, Third edition: Course of theoretical physics, Volume 7," Butterworth-Heinemann, Oxford, 1986.

Landau, L. D. and Lifshitz, E. M., "Fluid Mechanics, Second edition: Course of theoretical physics, Volume 6," Butterworth-Heinemann, Oxford, 1987.

Larsson, J. and Lele, S. K., "Direct numerical simulation of canonical shock/turbulence interaction," Physics of Fluids, vol. 21, 126101, 2009.

Larsson, J., Bermejo Moreno, I., and Lele, S. K., "Reynolds- and Mach-number effects in canonical shock–turbulence interaction," Journal of Fluid Mechanics, vol. 717, pp. 293–321, 2013.

Lee, S., Lele, S. K., and Moin, P., "Eddy shocklets in decaying compressible turbulence," Physics of Fluids A: Fluid Dynamics, vol. 3, pp. 657–664, 1991.

Lee, S., Lele, S. K., and Moin, P., "Direct numerical simulation of isotropic turbulence interacting with a weak shock wave," Journal of Fluid Mechanics, vol. 251, pp. 533–562, 1993.

Lele, S. K., "Shock-jump relations in a turbulent flow," Physics of Fluids A: Fluid Dynamics, vol 4, 2900, 1992.

Liepmann, H. W. and Roshko, A., "Elements of Gas Dynamics," Wiley, New York, 1957.

Lipkens, B. and Blackstock, D. T., "Model experiment to study sonic boom propagation

through turbulence. Part I: General results," The Journal of the Acoustical Society of America, vol. 103, pp. 148–158, 1998.

Maglieri, D. J., Bobbitt, P. J., Plotlin, K. J., Shepherd, K. P., Coen, P. G., and Richwine, D. M., "SONIC BOOM, Six decades of research," NASA/SP 2014 622, 2014.

Martín, T., Español, P., Rubio, M. A., and Zúñiga, I., "Dynamic fracture in a discrete model of a brittle elastic solid," Physical Review E, Vol. 61, pp. 6120–6131, 2000.

McManamen, B., Donzis, D. A., North, S. W., and Bowersox, R. D. W., "Velocity and temperature fluctuations in a high-speed shock–turbulence interaction," Journal of Fluid Mechanics, vol. 913, A10, 2021.

Moulinet, S. and Adda-Bedia, M., "Popping balloons: a case study of dynamical fragmentation," Physical Review Letter, vol. 115, 184301, 2015.

Petrie-Repar, P. J. and Jacobs, P. A., "A computational study of shock speeds in high-performance shock tubes," Shock Waves, vol. 8, pp. 79–91, 1998.

Ribner, H. S., "Shock–turbulence interaction and the generation of noise," NACA Report No. 1233, 1954.

Roach, P. E., "The generation of nearly isotropic turbulence by means of grids," International Journal of Heat and Fluid Flow, vol. 8, Issue 2, pp. 82–92, 1987.

Roark, R. J., "Formulas for Stress and Strain," McGraw-Hill Book Company Inc., New York and London, 1938.

Rothkopf, E. M. and Low, W., "Diaphragm opening process in shock tubes," The Physics of Fluids, vol. 17, pp. 1169–1173, 1974.

Ryu, J. and Livescu, D "Turbulence structure behind the shock in canonical shock–vortical turbulence interaction," Journal of Fluid Mechanics, vol. 756, R1, 2014.

Sasoh, A., Harasaki, T., Kitamura, K., Takagi, D., Ito, S., Matsuda, A., Nagata K., and Sakai, Y., “Statistical behavior of post-shock overpressure past grid turbulence,” Shock Waves, vol. 24, pp. 489–500, 2014.

Sasoh, A., “Compressible Fluid Dynamics and Shock Waves,” Springer Singapore, Singapore, 2020.

Shapiro, A. H. “The Dynamics and Thermodynamics of Compressible Fluid Flow, vol. I,” The Ronald Press Company, New York, 1953.

Shapiro, A. H. “The Dynamics and Thermodynamics of Compressible Fluid Flow, vol. II,” The Ronald Press Company, New York, 1953.

Strack, W. C. and Morris, Jr. S. J., “The challenges and opportunities of supersonic transport propulsion technology,” NASA-TM-100921, 1988.

Takahashi, H., Kanamori, M., Naka, Y., and Makino, Y., “Statistical characterization of atmospheric turbulence behavior responsible for sonic boom waveform deformation,” AIAA Journal, vol. 56, No. 2, pp. 673–686, 2018.

Tamba, T., Nguyen, T. M., Takeya, K., Harasaki, T., Iwakawa, A., and Sasoh, A. “Counter-driver shock tube,” Shock Waves, vol. 25, pp. 667–674, 2015.

Tamba, T., Furukawa, D., Aoki, Y., Kayumi, M., Iwakawa, A., Sasoh, A., Matsunaga, T., Izumo, M., Sugiyama, Y., Matsumura, T., and Nakayama, Y., “Field experiment of blast wave pressure modulation past a turbulent flow,” Science and Technology of Energetic Mate rials, vol. 77, No. 4, pp. 91–97, 2016.

Tanaka, K., Watanabe, T., Nagata, K., Sasoh, A., Sakai, Y., and Hayase, T., “Amplification and attenuation of shock wave strength caused by homogeneous isotropic turbulence,” Physics of Fluids, vol. 30, 035105, 2018.

Tanaka, K., Watanabe, T, and Nagata, K., “Statistical analysis of deformation of a shock

wave propagating in a local turbulent region," Physics of Fluids, vol. 32, 096107, 2020.

Trapier, S., Duveau, P., and Deck, S., "Experimental study of supersonic inlet buzz," AIAA Journal, vol. 44, No. 10, pp. 2354–2365, 2006.

White, D. R., "Influence of diaphragm opening time on shock-tube flows," Journal of Fluid Mechanics, vol. 4, pp. 585–599, 1958.

Xanthos, S., Briassulis, G., and Andreopoulos, Y., "Interaction of decaying freestream turbulence with a moving shock wave: pressure field," Journal of Propulsion and Power, vol. 18, No. 6, pp. 1289–1297, 2002.

Yang, J., PhD thesis, Tohoku University, 1995 (in Japanese).

Zhang, B., Azuma, J., and Uyama, H., "Preparation and characterization of a transparent amorphous cellulose film," RSC Advances, vol. 5, 2900, 2015.